

ABSTRACT

SEARCH FOR CHARGED HIGGS BOSONS IN THE $\tau + \ell$ FINAL STATE WITH 36.1 fb^{-1} OF pp COLLISION DATA AT $\sqrt{s} = 13 \text{ TeV}$ WITH THE ATLAS EXPERIMENT

Elliot Wesley Parrish, Ph.D.

Department of Physics

Northern Illinois University, 2022

Dhiman Chakraborty and Jahred Adelman, Director

This dissertation uses 139 fb^{-1} of pp collision data collected at a center of mass energy of $\sqrt{s} = 13 \text{ TeV}$ by the ATLAS detector to search for charged Higgs bosons decaying to a tau lepton and a neutrino ($H^\pm \rightarrow \tau^\pm \nu_\tau$) in association with a leptonically decaying top quark. No significant excess was found, therefore limits are set at the 95% confidence level on the charged Higgs production cross section times the branching fraction into the $\tau^\pm \nu_\tau$ ranging from XX pb to XX fb. These limits are interpreted in the hMSSM benchmark scenario as an exclusion at 95% confidence on $\tan \beta$ as a function of m_{H^\pm} . In this scenario, for $\tan \beta = 60$, the H^\pm mass range up to XXX GeV is excluded, with all values of $\tan \beta$ excluded for $m_{H^\pm} \leq XXX \text{ GeV}$.

NORTHERN ILLINOIS UNIVERSITY
DE KALB, ILLINOIS

DECEMBER 2022

**SEARCH FOR CHARGED HIGGS BOSONS IN THE $\tau + \ell$ FINAL STATE
WITH 36.1 fb^{-1} OF pp COLLISION DATA AT $\sqrt{s} = 13 \text{ TeV}$ WITH THE
ATLAS EXPERIMENT**

BY

ELLIOT WESLEY PARRISH
© 2022 Elliot Wesley Parrish

A DISSERTATION SUBMITTED TO THE GRADUATE SCHOOL
IN PARTIAL FULFILLMENT OF THE REQUIREMENTS
FOR THE DEGREE
DOCTOR OF PHILOSOPHY

DEPARTMENT OF PHYSICS

Dissertation Director:
Dhiman Chakraborty and Jahred Adelman

ACKNOWLEDGEMENTS

DEDICATION

To Dr. Dhiman Chakraborty. Thank you for everything.

TABLE OF CONTENTS

	Page
List of Tables	viii
List of Figures.	x
List of Appendices.	xvi
Chapter	
1 Introduction.	1
2 Theory	2
2.1 The Standard Model	2
2.1.1 Particles	2
2.1.1.1 Fermions	3
2.1.1.2 Bosons	3
2.1.2 Interactions	5
2.1.2.1 Quantum Electrodynamics	5
2.1.2.2 ElectroWeak Interaction.	6
2.1.2.3 Quantum Chromodynamics	7
2.1.3 The Higgs Mechanism	7
2.2 Supersymmetry.	10
2.2.1 MSMM Particles.	11
2.2.2 2 Higgs Doublet Model	12
2.3 Charged Higgs Bosons	13
2.3.1 Previous Result	13

Chapter	Page
3 Experimental Apparatus	19
3.1 Particle Accelerators	19
3.1.1 Hadron Colliders.	19
3.1.2 The Large Hadron Collider	20
3.1.3 CERN Accelerator Complex	22
3.1.4 Luminosity.	24
3.2 The ATLAS Detector	26
3.2.1 Detector Coordinates	27
3.2.2 Magnet Systems	29
3.2.2.1 Solenoid System	29
3.2.2.2 Toroid System.	30
3.2.3 Inner Detector	31
3.2.3.1 Pixel	32
3.2.3.2 Semiconductor Tracker.	32
3.2.3.3 Transition Radiation Tracker	33
3.2.4 Calorimeters.	34
3.2.4.1 Liquid Argon Calorimeters.	36
3.2.4.2 Tile Calorimeter	37
3.2.5 Muon Spectrometer	39
3.2.6 Trigger System	40
4 Simulation	43
4.1 Event Generation and Hadronization	44
4.2 Detector Simulation	44

Chapter	Page
5 Event Reconstruction	47
5.1 Tracks	48
5.2 Topological Clusters	48
5.3 Muon Identification	49
5.4 $e\gamma$ Identification	51
5.5 Jets	52
5.5.1 b -jet Tagging	55
5.6 τ Identification	56
5.7 E_T^{miss}	57
6 Search for Charged Higgs Bosons	59
6.1 Signature and Event Selection	60
6.1.1 Object Definitions	61
6.1.2 Event Selections	62
6.2 Datasets	63
6.2.1 Signal Modeling	63
6.3 Background Modeling	65
6.4 Multivariate Analysis Techniques	73
6.4.1 Training	74
6.4.2 Input Variables Selection	75
6.4.3 Hyperparameter Optimization	77
6.5 Systematic Uncertainties	77
6.6 Results	78
7 Conclusion	79
Appendices	80

Appendices	81
----------------------	----

LIST OF TABLES

Table	Page
2.1 Standard Model fermions and their properties [1]	4
2.2 Standard Model bosons and their properties [1]	4
2.3 Standard Model fermions and their ElectroWeak properties [1].	6
2.4 SM particles and their MSSM partners [1]	11
2.5 2HDM extended Higgs sector [6]	12
3.1 LHC parameters [9]	21
3.2 Accelerator final energies	23
3.3 Design resolution of EM and hadronic calorimeters in the ATLAS Detector..	34
6.1 H^\pm production mechanisms based on m_{H^\pm} , dominant H^\pm decay mode, and the main background associated with the diagram.	60
6.2 Definitions of physics objects used in this analysis.	61
6.3 $\tau + \text{jets}$ and $\tau + \ell$ signal region definitions.	62
6.4 For each H^\pm mass the generator cross-section ($\sigma \times BR(H^\pm \rightarrow \tau^\pm \nu_\tau)$) is given, as well as the number of generated events for both $\tau + \ell$ and $\tau + \text{jets}$ subchannels.	64
6.5 Dominant backgrounds from prompt $\tau_{\text{had-vis}}$ and fake $\tau_{\text{had-vis}}$ candidates.	65
6.6 Cross sections for the main SM background samples at $\sqrt{s} = 13$ TeV . Here, ℓ refers to the three lepton families e , μ and τ . All background cross sections are normalized to NNLO predictions, except for diboson events, where the NLO prediction is used. A '*' indicates that the quoted cross section for the sample is neglecting leptonic/hadronic branching ratios.	66
6.7 Control region definitions for the $\tau + \text{jets}$ subchannel.	67

Table	Page
6.8 Control region definitions for the $\tau + \ell$ subchannel.	68
6.9 List of low level (a) and high level (b) kinematic variables used as input to the PNN in the $\tau + \ell$ subchannel. $\Delta\phi_{X,\text{miss}}$ denotes the difference in azimuthal angle between a reconstructed object X ($X = \tau, b - \text{jet}, \ell$) and the direction of the missing transverse momentum.	76

LIST OF FIGURES

Figure		Page
2.1	The Higgs potential defined in 2.2 with $\mu^2 < 0$ [4]	8
2.2	The distributions of the invariant mass of diphoton candidates after all selections for the combined 7 TeV and 8 TeV data sample. The inclusive sample is shown in (a) and a weighted version of the same sample in (c); the weights are explained in the text. The result of a fit to the data of the sum of a signal component fixed to $m_H = 126.5$ GeV and a background component described by a fourth-order Bernstein polynomial is superimposed. The residuals of the data and weighted data with respect to the respective fitted background component are displayed in (b) and (d).	14
2.3	Examples of leading-order Feynman diagrams contributing to the production of charged Higgs bosons in pp collisions: (a) non-resonant top-quark production, (b) single-resonant top-quark production that dominates at large H^\pm masses, (c) double-resonant top-quark production that dominates at low H^\pm masses. The interference between these three main diagrams becomes most relevant in the intermediate-mass region.	15
2.4	Cross section of H^\pm at various $\tan \beta$ values.	15
2.5	Branching ratios of H^\pm for (a) $\tan \beta = 10$ and (b) $\tan \beta = 50$ [7]	16
2.6	Limits on $\sigma(pp \rightarrow tbH^\pm xB(H^\pm \rightarrow \tau^\pm \nu))[pb]$. (a) is for the $\tau + \text{jets}$ subchannel (b) corresponds to the $\tau + \ell$ subchannel and (c) is the combination of the two subchannels. [8]	17
2.7	Limits on $\tan \beta$ as a function of m_{H^\pm} . [8]	18
3.1	Cross-section of cryodipole (lengths in mm). [10]	21
3.2	Field of the LHC dipole magnets. [11].	22
3.3	The CERN accelerator complex. [12]	23

Figure	Page
3.4 Cumulative luminosity versus time delivered to ATLAS (green), recorded by ATLAS (yellow), and certified to be good quality data (blue) during stable beams for pp collisions at 13 TeV center of mass energy in 2015-2018. The difference between the colored histograms reflects inefficiencies, especially those seen when restarting data taking.	25
3.5 The luminosity-weighted distribution of the mean number of interactions per bunch crossing for the 2015-2018 pp collision dataset at 13 TeV center of mass energy.	25
3.6 A display of a candidate Z boson event from proton-proton collisions recorded by ATLAS with LHC stable beams at a collision energy of 13 TeV. The Z boson candidate is reconstructed in a beam crossing with 28 additionally reconstructed primary vertices from the minimum bias interactions. The candidate event is reconstructed in the 2μ final state. In the left display, the red lines show the path of the two muons including the hits in the muon spectrometer and the yellow tracks are the remaining charged particles from the 29 vertices, with transverse momentum above 0.5 GeV. The colored squares in the lower display correspond to the position of the reconstructed vertices. The invariant mass of the two muons is 92.3 GeV.	26
3.7 Cut-away view of the ATLAS detector with major subdetectors highlighted.	27
3.8 A diagram showing the pseudorapidity η and corresponding θ values. [13] . .	28
3.9 The ATLAS magnet systems.	29
3.10 (a) Cut-away view of the ATLAS Inner Detector. (b) Cross-sectional view of the ATLAS Inner Detector.	31
3.11 Interaction lengths as a function of η in the ATLAS calorimeters. The unlabeled brown color is the material in front of the EM calorimeters and the unlabeled cyan is the amount of material in front of the first active layer of the muon spectrometer. [20]	35
3.12 Cut-out view of the ATLAS detector's calorimeters.	35
3.13 A EMB module showing the accordion geometry and granularity. [20] . . .	37
3.14 (a) Diagram of an individual TileCal module. (b) Azimuthal view of two TileCal modules with the IP being to the right.	38
3.15 Cut-out view of the ATLAS detector Muon Spectrometer.	40

Figure	Page
3.16 The ATLAS TDAQ system in Run-2 showing the components relevant for triggering as well as the detector read-out and data flow.	41
4.1 A pictorial representation of the simulation chain used in the ATLAS experiment. [23].	43
4.2 A pictorial representation of a parton shower of a $t\bar{t}H$ event. [23]	45
5.1 Cross section view of the ATLAS detector with subdetectors labeled. Various types of particles radial trajectories are shown.	47
5.2 Algorithm flow diagram for the electron and photon reconstruction [28].	52
5.3 A flow chart of how the particle flow algorithm proceeds, starting with track selection and continuing until the energy associated with the selected tracks has been removed from the calorimeter. At the end, charged particles, topoclusters which have not been modified by the algorithm, and remnants of topoclusters which have had part of their energy removed remain [29].	53
5.4 Idealized examples of how the algorithm is designed to deal with several different cases. The red cells are those which have energy from the π^+ , the green have cells energy from the photons in the π^0 decay, the dotted lines represent the original topocluster boundaries with those outlined in blue having been matched by the algorithm to the π^+ , while those in black are yet to be selected. The different layers in the EM calorimeter (Presampler, EMB1, EMB2, EMB3) are indicated. In this sketch only the first two layers of the Tile calorimeter are shown (TileBar0 and TileBar1) [29].	54
5.5 Comparison between several jet finding algorithms [30].	55
5.6 Schematic view of the tracks in a b -jet [32].	56
6.1 Signal acceptance as a function of the charged Higgs boson mass for both the $\tau + \text{jets}$ (a) and $\tau + \ell$ subchannels (b).	63
6.2 Mass of $\tau - e$ system in the Zee control region.	66
6.3 Combined fake factors for the $\tau + \text{jets}$ b-veto $m_T > 100$ control region, $\tau + \text{jets}$ signal region, $\tau + \text{electron(muon)}$ with same-sign control region and the $\tau + \ell$ signal region. Error bars represent systematic uncertainties of the method.	70

Figure	Page
6.4 Comparison between the predicted and the measured E_T^{miss} distributions in various control regions defined for the $\tau + \text{jets}$ channel. The uncertainty band includes both statistical and systematic uncertainties on the background prediction	71
6.5 Comparison between the predicted and the measured E_T^{miss} distributions in various control regions defined for the $\tau + \ell$ channel. The uncertainty band includes both statistical and systematic uncertainties on the background prediction	72
6.6 <i>Left</i> , individual networks with input variables (x_1, x_2) , each trained with examples with a single value of some parameter $\theta = \theta_a, \theta_b$. The individual networks are purely functions of the input variables. Performance for intermediate values of θ is not optimal nor does it necessarily vary smoothly between the networks. <i>Right</i> , a single network trained with input variables (x_1, x_2) as well as input parameter θ ; such a network is trained with examples at several values of the parameter θ [38].	74
6.7 The k-fold method for $k = 5$ [41].	75
6.8 Expected limits comparing a set of high level variables and low level variables with various depths in the PNN architecture. X layers refers to the number of layers in the PNN.	77
B.1 Fake factors parameterized as a function of p_T^τ and the number of charged τ decay products (1-prong and 3-prong) obtained in the multi-jet and W+jets CRs. The errors shown represent the statistical uncertainty.	83
B.2 Corrected α_{MJ} values for the $\tau_{\text{had-vis}} + \text{jets}$ b-veto $m_T > 100$ control region, $\tau_{\text{had-vis}} + \text{jets}$ signal region, $\tau_{\text{had-vis}} + \text{electron(muon)}$ with same-sign control region and the $\tau_{\text{had-vis}} + \text{lepton}$ signal region. Error bars represent uncertainties due to α_{MJ} fitting using template-fit method.	83
B.3 Estimation of α_{MJ} in the $\tau_{\text{had-vis}} + \text{jets}$ signal region for $p_T \leq 60$ GeV 1-prong $\tau_{\text{had-vis}}$ candidates. Left: templates of discriminating variables for different $\tau_{\text{had-vis}}$ p_T and n-prong slices. Middle: shape of the discriminating variable obtained in the signal region and fitted shape using the templates measured in the control regions. Right: χ^2/ndf of the fit as a function of α_{MJ} , the error on α_{MJ} is defined by the band at $\chi^2_{\text{min}}/\text{ndf} + \sqrt{\frac{2}{\text{ndf}}}$	84

Figure	Page
B.4 Estimation of α_{MJ} in the $\tau_{had-vis} + \text{jets}$ signal region for $p_T \geq 60 \text{ GeV}$ 1-prong $\tau_{had-vis}$ candidates. Left: templates of discriminating variables for different $\tau_{had-vis} p_T$ and n-prong slices. Middle: shape of the discriminating variable obtained in the signal region and fitted shape using the templates measured in the control regions. Right: χ^2/ndf of the fit as a function of α_{MJ} , the error on α_{MJ} is defined by the band at $\chi^2_{\min}/\text{ndf} + \sqrt{\frac{2}{\text{ndf}}}$	85
B.5 Estimation of α_{MJ} in the $\tau_{had-vis} + \text{jets}$ signal region for 3-prong $\tau_{had-vis}$ candidates. Left: templates of discriminating variables for different $\tau_{had-vis} p_T$ and n-prong slices. Middle: shape of the discriminating variable obtained in the signal region and fitted shape using the templates measured in the control regions. Right: χ^2/ndf of the fit as a function of α_{MJ} , the error on α_{MJ} is defined by the band at $\chi^2_{\min}/\text{ndf} + \sqrt{\frac{2}{\text{ndf}}}$	86
B.6 Estimation of α_{MJ} in the $\tau_{had-vis} + \text{lepton}$ signal region for $p_T \leq 50 \text{ GeV}$ 1-prong $\tau_{had-vis}$ candidates. Left: templates of discriminating variables for different $\tau_{had-vis} p_T$ and n-prong slices. Middle: shape of the discriminating variable obtained in the signal region and fitted shape using the templates measured in the control regions. Right: χ^2/ndf of the fit as a function of α_{MJ} , the error on α_{MJ} is defined by the band at $\chi^2_{\min}/\text{ndf} + \sqrt{\frac{2}{\text{ndf}}}$	87
B.7 Estimation of α_{MJ} in the $\tau_{had-vis} + \text{lepton}$ signal region for $p_T \geq 50 \text{ GeV}$ 1-prong $\tau_{had-vis}$ candidates. Left: templates of discriminating variables for different $\tau_{had-vis} p_T$ and n-prong slices. Middle: shape of the discriminating variable obtained in the signal region and fitted shape using the templates measured in the control regions. Right: χ^2/ndf of the fit as a function of α_{MJ} , the error on α_{MJ} is defined by the band at $\chi^2_{\min}/\text{ndf} + \sqrt{\frac{2}{\text{ndf}}}$	88
B.8 Estimation of α_{MJ} in the $\tau_{had-vis} + \text{lepton}$ signal region for $p_T \leq 60 \text{ GeV}$ 3-prong $\tau_{had-vis}$ candidates. Left: templates of discriminating variables for different $\tau_{had-vis} p_T$ and n-prong slices. Middle: shape of the discriminating variable obtained in the signal region and fitted shape using the templates measured in the control regions. Right: χ^2/ndf of the fit as a function of α_{MJ} , the error on α_{MJ} is defined by the band at $\chi^2_{\min}/\text{ndf} + \sqrt{\frac{2}{\text{ndf}}}$	89

Figure	Page
B.9 Estimation of α_{MJ} in the $\tau_{\text{had-vis}} + \text{lepton}$ signal region for $p_T \geq 60\text{GeV}$ 3-prong $\tau_{\text{had-vis}}$ candidates. Left: templates of discriminating variables for different $\tau_{\text{had-vis}}$ p_T and n-prong slices. Middle: shape of the discriminating variable obtained in the signal region and fitted shape using the templates measured in the control regions. Right: χ^2/ndf of the fit as a function of α_{MJ} , the error on α_{MJ} is defined by the band at $\chi^2_{\min}/\text{ndf} + \sqrt{\frac{2}{\text{ndf}}}$	90
C.1 Comparison between the predicted and the measured p_T^τ distributions in various control regions defined for the $\tau + \text{jets}$ channel. The uncertainty band includes both statistical and systematic uncertainties on the background prediction.	92
C.2 Comparison between the predicted and the measured p_T^{b-jet} distributions in various control regions defined for the $\tau + \text{jets}$ channel. The uncertainty band includes both statistical and systematic uncertainties on the background prediction.	93
C.3 Comparison between the predicted and the measured p_T^τ distributions in various control regions defined for the $\tau + \ell$ channel. The uncertainty band includes both statistical and systematic uncertainties on the background prediction.	95
C.4 Comparison between the predicted and the measured p_T^ℓ distributions in various control regions defined for the $\tau + \ell$ channel. The uncertainty band includes both statistical and systematic uncertainties on the background prediction.	96
C.5 Comparison between the predicted and the measured p_T^e distributions in various control regions defined for the $\tau + \ell$ channel. The uncertainty band includes both statistical and systematic uncertainties on the background prediction.	97
C.6 Comparison between the predicted and the measured p_T^μ distributions in various control regions defined for the $\tau + \ell$ channel. The uncertainty band includes both statistical and systematic uncertainties on the background prediction.	98
C.7 Comparison between the predicted and the measured p_T^{b-jet} distributions in various control regions defined for the $\tau + \ell$ channel. The uncertainty band includes both statistical and systematic uncertainties on the background prediction.	99

LIST OF APPENDICES

Appendix	Page
A TileCal Data Quality	81
B Fake Factors.	82
C Additional Validation Plots	91
C.1 τ +jets Validation Plots.	92
C.2 $\tau + \ell$ Validation Plots	94

CHAPTER 1

INTRODUCTION

CHAPTER 2

THEORY

In this chapter, the theoretical motivation of a search for $H^\pm \rightarrow \tau^\pm \nu_\tau$ is described. Firstly, a review of the Standard Model of particle physics (SM) is laid out, then a brief overview of Supersymmetry focusing on the Minimal Supersymmetric Standard Model (MSSM). Finally, the Type II 2-Higgs Doublet Model's (2HDM) relation to the H^\pm production cross section and subsequent branching ratio into SM particles is described as motivation for the choice of studying $H^\pm \rightarrow \tau^\pm \nu_\tau$.

2.1 The Standard Model

The SM of particle physics is a quantum field theory that describes all known matter and forces. The SM is built upon a gauge group of type $SU(3)_C \times SU(2)_L \times U(1)_Y$. The $SU(3)_C$ term dictates the strong interaction while the $SU(2)_L \times U(1)_Y$ term describes the electroweak interaction. These interactions occur between fundamental particles called fermions that comprise the known matter of the universe. The interactions, or forces, are mediated by fundamental particles called bosons.

2.1.1 Particles

The particles that make up the SM are separated into two groups according to their intrinsic angular momentum charge, or spin. Fermions are those that carry half-integer spin,

and thus obey Fermi-Dirac statistics, while Bosons carry full integer spin values and obey Bose-Einstein statistics.

2.1.1.1 Fermions

The matter we encounter in everyday life is comprised of fermions. Fermions are subdivided into two groups, quarks and leptons. The quarks participate in the strong interaction via their color charge. Quarks cannot exist as a singular particle and thus combine into hadrons in a process called hadronization; the bound states they form are colorless. The proton and neutron are examples of hadrons. Leptons carry no color charge and therefore do not participate in strong force interactions. The fermions in the SM all participate in the electroweak interaction. However, the electromagnetic interaction is limited to those fermions that carry an electromagnetic charge. Section 2.1.2.2 describes the electroweak interaction in detail.

Fermions can then be further divided into three generations, each lepton has an electrically neutral weak force partner in the form of a neutrino. Table 2.1 lists all the SM fermions and their properties.

2.1.1.2 Bosons

Bosons are colloquially referred to as force-carriers in that the fundamental forces act via exchanging gauge bosons. This means that each force has an associated boson which is described by a field theory. The ElectroWeak quantum field theory (QFT) is more complicated, and is described in detail in section 2.1.2.2. Table 2.2 lists the SM bosons¹, their associated field theory and properties.

¹excluding the Higgs

Table 2.1: Standard Model fermions and their properties [1]

	1^{st} Generation	2^{nd} Generation	3^{rd} Generation	Spin	EM Charge	Color	Mass
Quarks	Up (u)	Charm (c)	Top (t)	$\frac{1}{2}$	$+\frac{2}{3}$	✓	$m_u = 2.16_{-0.26}^{+0.49}$ MeV $m_c = 1.27 \pm 0.02$ GeV $m_t = 172.76 \pm 0.30$ GeV
	Down (d)	Strange (s)	Bottom (b)	$\frac{1}{2}$	$-\frac{1}{3}$	✓	$m_d = 4.67_{-0.17}^{+0.48}$ MeV $m_s = 93_{-5}^{11}$ MeV $m_b = 4.18_{-0.02}^{0.03}$ GeV
Leptons	Electron (e^-)	Muon (μ^-)	Tau (τ^-)	$\frac{1}{2}$	-1	X	$m_{e^-} = 0.51$ MeV $m_{\mu^-} = 105.65$ MeV $m_{\tau^-} = 1776.86 \pm 0.12$ MeV
	Electron Neutrino (ν_e)	Muon Neutrino (ν_μ)	Tau Neutrino (ν_τ)	$\frac{1}{2}$	0	X	$m_{\nu_e} < 1.1$ eV $m_{\nu_\mu} < 0.19$ MeV $m_{\nu_\tau} < 18.2$ MeV

Table 2.2: Standard Model bosons and their properties [1]

Field Theory	Boson	Spin	EM Charge	Color	Mass
Quantum Chromodynamics (QCD)	Gluon (g)	1	0	✓	0
Quantum Electrodynamics (QED)	Photon (γ)	1	0	X	$< 1 \times 10^{-18}$ eV
ElectroWeak Theory	W^\pm	1	± 1	X	80.379 ± 0.012 GeV
	Z^0	1	0	X	91.1876 ± 0.0021 GeV

2.1.2 Interactions

At its core, the SM relies upon symmetries. From these symmetries, conservation laws follow. It is these laws of conservation, and the breaking of the associated symmetry, that dictate the allowed interactions of matter. The first, being a symmetry under charge conjugation, mirror reflection, and time reversal is known as CPT symmetry. The symmetry between charge conjugation and mirror reflection (CP) can be broken in certain circumstances, but holds in strong and electromagnetic interactions. This breaking of CP symmetry occurs in the weak interaction and implies a non-symmetry between matter and antimatter. Since this symmetry holds for strong and electromagnetic interactions, baryon number ($B = \frac{1}{3}(n_q - n_{\bar{q}})$) and lepton number are conserved in SM interactions. Lepton generation number ², electric charge, color charge, 4-momentum ($p = (E, \vec{p})$), and angular momentum are all conserved in the SM.

2.1.2.1 Quantum Electrodynamics

The electromagnetic force is governed by the QFT known as Quantum Electrodynamics (QED). This force is mediated by the photon, γ , a massless boson with EM charge 0. The EM force only affects, in other words, the photon only interacts with, charged particles; including all quarks and the e , μ , and τ leptons. Antiparticles are those that carry the opposite EM charge from their normal counterparts and differ in no other way. Antiparticles are denoted by a bar above the particle symbol (e, \bar{e}).

²Ignoring neutrino oscillations

2.1.2.2 ElectroWeak Interaction

The weak force is most often seen in nuclear decays and is mediated by the W^\pm and Z^0 bosons. Due to the relatively large mass of these bosons, the weak force has a very limited range. The W^\pm affects the third component of isospin (T_3), thus only coupling to so called left-handed fermions. This “handedness”, or chirality, is a property similar to color charge, in that an individual particle can have a number of different values. Table 2.3 contains the allowed values for isospin (T) and hypercharge (Y_W).

Table 2.3: Standard Model fermions and their ElectroWeak properties [1]

	1^{st} Generation	2^{nd} Generation	3^{rd} Generation	EM Charge	Y_W		T		T_3	
	Up (u)	Charm (c)	Top (t)	$+\frac{2}{3}$	LH $+\frac{1}{3}$	RH $+\frac{4}{3}$	LH $\frac{1}{2}$	RH 0	LH $\pm\frac{1}{2}$	RH 0
Quarks	Down (d)	Strange (s)	Bottom (b)	$-\frac{1}{3}$	$+\frac{1}{3}$	$-\frac{2}{3}$	$\frac{1}{2}$	0	$\pm\frac{1}{2}$	0
	Electron (e^-)	Muon (μ^-)	Tau (τ^-)	-1	-1	0	$\frac{1}{2}$	0	$\pm\frac{1}{2}$	0
Leptons	Electron Neutrino (ν_e)	Muon Neutrino (ν_μ)	Tau Neutrino (ν_τ)	0	-1	-2	$\frac{1}{2}$	0	$\pm\frac{1}{2}$	0

The W^\pm bosons have a T_3 component of isospin and act as raising or lowering operators on the T_3 component of left handed fermions. The Z does not have a T_3 component, and thus does not act on isospin of fermions. However, the Z boson instead transfers momentum, energy, and spin on all fermions irregardless of their chirality. At energies > 100 GeV the electromagnetic and weak forces combine into the electroweak force. In fact, isospin and hypercharge combine to give electromagnetic charge. $Q_{EM} = T_3 + \frac{1}{2}Y_W$

2.1.2.3 Quantum Chromodynamics

Quantum chromodynamics (QCD) is the QFT that describes the strong force that holds together atomic nuclei and other objects called hadrons. The strong force interacts via the color charge³ which can have values of either red, green, or blue. Particles that have a color charge cannot exist on their own, they must form colorless bound states called hadrons. Since the strong force grows with distance, if a quark is ejected out from a hadron, the stored energy is such that new particles with color charge will be spontaneously created from the vacuum, binding with the free quark in a process called hadronization. In a particle detector, the hadronization process cascades and creates showers of hadrons that are reconstructed as so called jets.

2.1.3 The Higgs Mechanism

The Higgs field is the mass generator of the SM and was first theorized by Peter Higgs [2], François Englert, and Robert Brout [3] in 1964. The SM itself has four massless Goldstone bosons that do not correspond to the observed bosons. Instead, the Higgs mechanism couples to them via a complex scalar doublet.

$$\phi = \begin{pmatrix} \phi^+ \\ \phi^0 \end{pmatrix} \quad (2.1)$$

The scalar potential that gives rise to this phenomena can be written as

$$V(\phi) = \mu^2 |\phi^\dagger \phi| + \lambda (|\phi^\dagger \phi|)^2 \quad (2.2)$$

³This color does is not the visual color we are used to. Merely a convenient analogous naming scheme.

When $\mu^2 > 0$ and $\lambda > 0$ the minimum of the potential $V(\phi)$ is 0. However, when $\mu^2 < 0$,

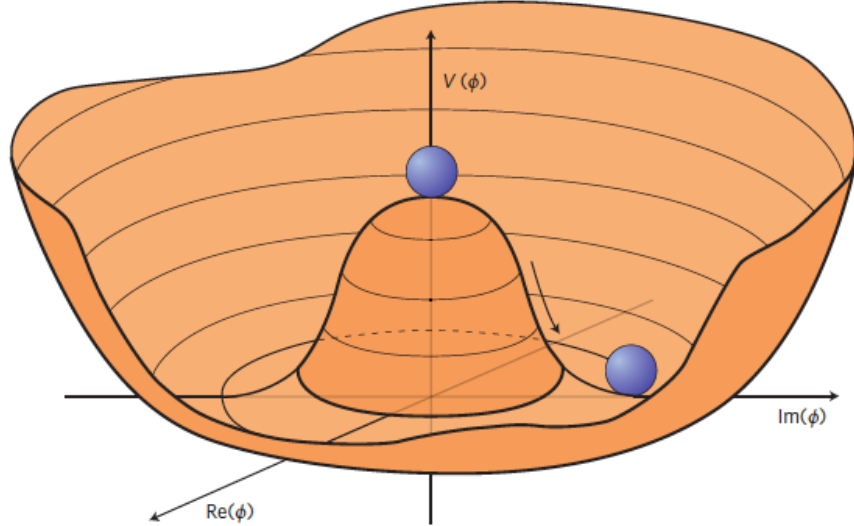


Figure 2.1: The Higgs potential defined in 2.2 with $\mu^2 < 0$ [4]

the scalar potential $V(\phi)$ takes the shape shown in figure 2.1. It follows that the vacuum expectation value (VEV) of ϕ is then

$$\langle \phi \rangle = \sqrt{\frac{-\mu^2}{2\lambda}} = \frac{\nu}{\sqrt{2}} \quad (2.3)$$

From here, convention states that we choose an arbitrary direction of the fluctuation as

$$\phi^0 = \frac{1}{\sqrt{2}} \begin{pmatrix} 0 \\ \nu \end{pmatrix} \quad (2.4)$$

By choosing these values, $SU(2)$ and $U(1)_Y$ symmetries are broken, the Goldstone bosons are “eaten” and we are left with the remaining degree of freedom being the real scalar field $h(x)$

$$\phi(x) = \phi^0 + h(x) \quad (2.5)$$

Substituting in our definition of ϕ^0 , we get

$$\phi = \frac{1}{\sqrt{2}} \begin{pmatrix} 0 \\ \nu + h(x) \end{pmatrix} \quad (2.6)$$

and couples to the gauge bosons via

$$(\frac{1}{2}g\vec{\sigma} \cdot \vec{W} + \frac{1}{2}g'B)\phi^0 \quad (2.7)$$

, where $\vec{\sigma}$ are the Pauli matrices, \vec{W} are $W_{1,2,3}$, g is the weak coupling constant, and g' is the hypercharge coupling constant. From this coupling, we get the four eigenstates that correspond to the observed bosons

$$\begin{aligned} W^\pm &= \frac{1}{\sqrt{2}}(W_\mu^1 \mp iW_\mu^2) \\ Z^\mu &= \frac{-g'B_\mu + gW_\mu^3}{\sqrt{g^2 + g'^2}} \\ A^\mu &= \frac{gB_\mu + g'W_\mu^3}{\sqrt{g^2 + g'^2}} \end{aligned} \quad (2.8)$$

These eigenstates have corresponding mass values of

$$\begin{aligned} M_W^2 &= \frac{1}{4}g^2\nu^2 \\ M_Z^2 &= \frac{1}{4}(g^2 + g'^2)\nu \\ M_A^2 &= 0 \end{aligned} \quad (2.9)$$

The eigenstate labeled here as A is the photon. The Higgs boson was discovered in 2012 by the ATLAS and CMS collaborations at CERN with a mass of 125 GeV [5]. The scalar boson that was found appears to be the SM Higgs Boson.

2.2 Supersymmetry

While the SM is describes a wide range of physics to a high degree of accuracy, it is not without issues. To name a few, gravity, dark matter, and the observed matter-antimatter asymmetry of the universe are not defined by the SM. In addition, the SM defines the mass of neutrinos to be 0. However, because neutrino mixing is observed, where $\nu_e \rightarrow \nu_\mu$ is seen, neutrinos must have mass.

One promising model that offers solutions to many of these issues is Supersymmetry (SUSY). As discussed previously, the SM is built upon symmetries, and the breaking of these symmetries gives us electroweak unification. SUSY proposes another symmetry, this time between fermions and bosons.

$$\begin{aligned} Q|Fermion\rangle &= |Boson\rangle, \\ Q|Boson\rangle &= |Fermion\rangle \end{aligned} \tag{2.10}$$

Equation 2.10 shows how the SUSY operator Q acts on particles. SUSY naturally offers solutions to the “hierarchy problem” with the SM.

The hierarchy problem arises from the difference in electroweak ($M_W \sim 100$ GeV) and Planck ($M_P \sim 2.4 \times 10^{18}$ GeV) mass scales. For the Higgs mass to be on the scale of $M_H \sim 125$ GeV incredibly large and small mass terms must cancel perfectly, leading to a feeling of “unnaturalness”. SUSY brings many new particles into the picture, theorized to occupy the intermediate mass range leading to a more natural theory.

2.2.1 MSMM Particles

SUSY is a large group of theories, including many additional superpartner particles. The Minimal Supersymmetric Standard Model (MSSM) is the smallest extension of the SM that introduces SUSY. In the MSSM, each SM particle is part of a supermultiplet with its superpartner where both particles have the same quantum numbers, except spin. If this supersymmetry is unbroken, then the superpartner and the SM particle would have the same mass as well. However, SUSY has not been observed, so the supersymmetry must be broken putting the mass scale on the TeV scale.

Table 2.4: SM particles and their MSSM partners [1]

Name	SM	MSSM
Spin- $\frac{1}{2}$ quarks and spin-0 squarks		
(s)up	u	\tilde{u}
(s)down	d	\tilde{d}
(s)charm	c	\tilde{c}
(s)strange	s	\tilde{s}
(s)top	t	\tilde{t}
(s)bottom	b	\tilde{b}
Spin- $\frac{1}{2}$ leptons and spin-0 sleptons		
(s)electron	e	\tilde{e}
(s)electron (s)neutrino	ν_e	$\tilde{\nu}_e$
(s)muon	μ	$\tilde{\mu}$
(s)muon (s)neutrino	ν_μ	$\tilde{\nu}_\mu$
(s)tau	τ	$\tilde{\tau}$
(s)tau (s)neutrino	ν_τ	$\tilde{\nu}_\tau$
Spin-0 Higgs and spin- $\frac{1}{2}$ Higgsinos		
Higgs(ino)	H	\tilde{H}
gluon (gluino)	g	\tilde{g}
W (Wino)	W^\pm, W^0	$\widetilde{W}^\pm, \widetilde{W}^0$
B (Bino)	B^0	\widetilde{B}^0

Table 2.4 lists the MSSM supermultiplets and the associated naming conventions.

2.2.2 2 Higgs Doublet Model

Having only one Higgs chiral supermultiplet with hypercharge $Y_W = \pm \frac{1}{2}$ leads to a gauge anomaly. This can be resolved by introducing two Higgs doublets with hypercharge $Y_W = \frac{1}{2}$ and $Y_W = -\frac{1}{2}$. Such is the case with the MSSM which requires two complex doublet scalar fields where one couples to the up-type quarks and the other couples to down-type quarks and charged leptons. At this point, the MSSM has 8 degrees of freedom. Following the same type of symmetry breaking described in subsection 2.1.3 Three of these degrees of freedom give the observed W^\pm and Z^0 bosons. This leaves us with the extended Higgs sector shown

Table 2.5: 2HDM extended Higgs sector [6]

light neutral scalar	h^0
heavy neutral scalar	H^0
neutral pseudoscalar	A^0
two charged scalars	H^\pm

in table 2.5, where the h^0 is the SM-like Higgs that was discovered by ATLAS and CMS in 2012. When referring to the charged Higgs bosons, we often refer to them using one symbol H^\pm . In the 2HDM we have two free parameters⁴, the masses of the H^\pm and the ratio of their vacuum expectation values which is defined as $\tan \beta$. These types of models are referred to as Type II 2HDM.

⁴Only regarding the charged Higgs bosons

2.3 Charged Higgs Bosons

Since the H^\pm couplings are proportional to the fermion masses, the main production modes at the LHC are through $t\bar{t}$ and Wt diagrams where the W is replaced by a H^\pm . The production diagrams considered in this dissertation can be seen in figure 2.3. The cross section at various $\tan\beta$ values can be seen as a function of m_{H^\pm} in figure 2.4. As $\tan\beta$ goes to smaller values the H^\pm cross section become smaller and at very small values the top Yukawa couplings become non-perturbative, meaning they are highly unlikely to occur. In this dissertation the decay channel considered is $H^\pm \rightarrow \tau^\pm \nu_\tau$. As can be seen in figure 2.5, the $H^\pm \rightarrow \tau^\pm \nu_\tau$ decay channel is especially relevant at low m_{H^\pm} and high $\tan\beta$. The search described in this dissertation consists of two sub-channels, $\tau + \text{jets}$ and $\tau + \ell$, where the associated top decays either hadronically or leptonically respectively.

2.3.1 Previous Result

To add context to this dissertation, it is important to reference the results of the previous iteration of the search discussed in this dissertation. The ATLAS collaboration published a paper in 2018 covering the data taking years of 2015 and 2016 [8], whereas this dissertation covers the full Run-2 (2015-2018) dataset. Figure 2.6 shows the limits on the cross section and figure 2.7 shows the limits on $\tan\beta$ as a function of m_{H^\pm} .

The previous iteration of this analysis used boosted decision trees (BDT) binned in m_{H^\pm} , giving them five separate classifiers to cover the mass range of 90 – 2000 GeV. The mass bins can be seen as the blue dotted lines in Figure 2.6c. It is important to note the inclusion of the mass range 90 – 200 GeV, as [8] was the first search to include this mass region below the top quark mass of 175 GeV.

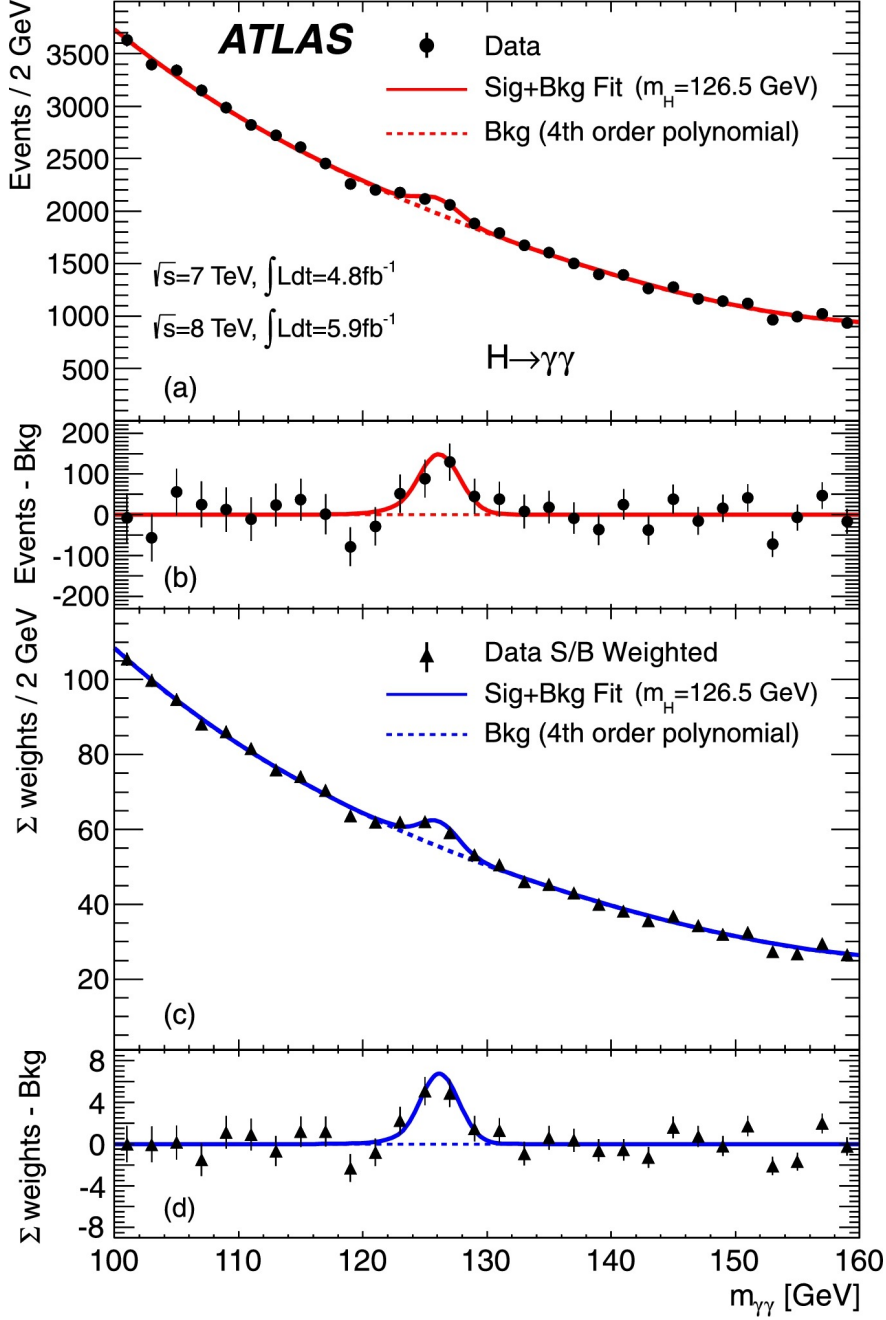


Figure 2.2: The distributions of the invariant mass of diphoton candidates after all selections for the combined 7 TeV and 8 TeV data sample. The inclusive sample is shown in (a) and a weighted version of the same sample in (c); the weights are explained in the text. The result of a fit to the data of the sum of a signal component fixed to $m_H = 126.5$ GeV and a background component described by a fourth-order Bernstein polynomial is superimposed. The residuals of the data and weighted data with respect to the respective fitted background component are displayed in (b) and (d).

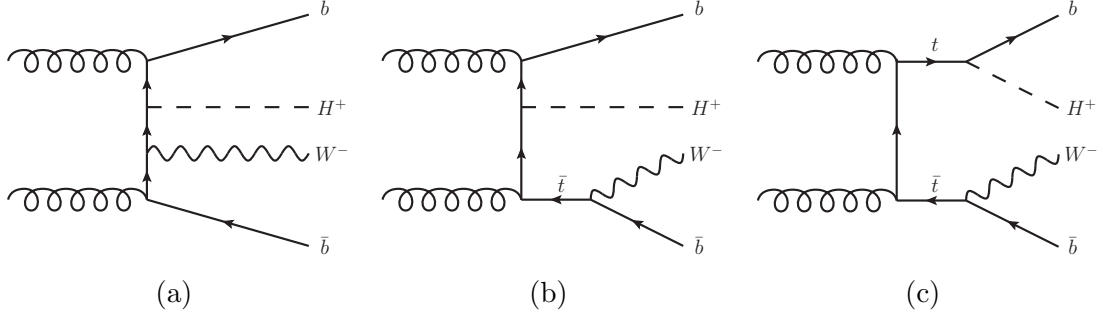


Figure 2.3: Examples of leading-order Feynman diagrams contributing to the production of charged Higgs bosons in pp collisions: (a) non-resonant top-quark production, (b) single-resonant top-quark production that dominates at large H^\pm masses, (c) double-resonant top-quark production that dominates at low H^\pm masses. The interference between these three main diagrams becomes most relevant in the intermediate-mass region.

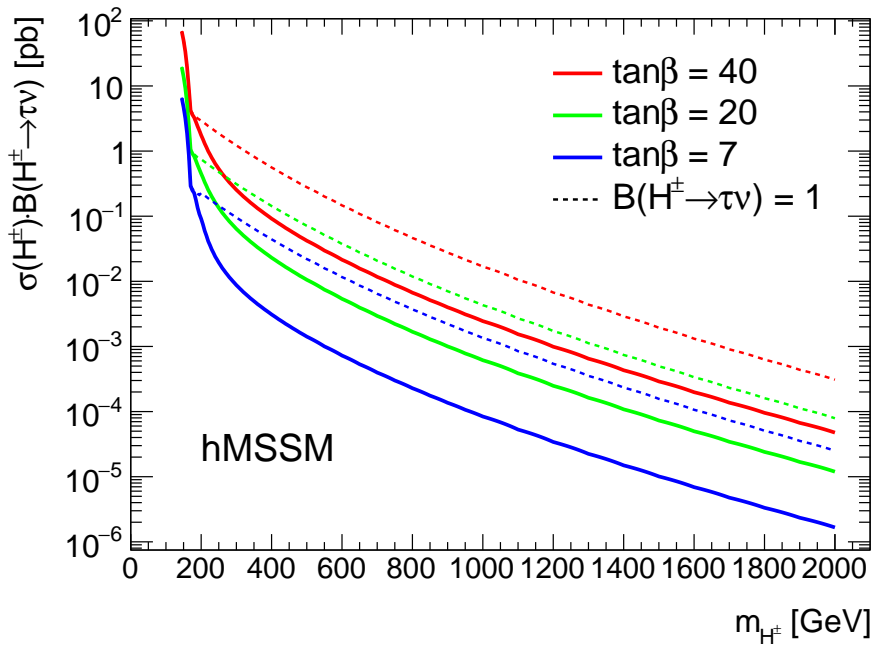


Figure 2.4: Cross section of H^\pm at various $\tan\beta$ values.

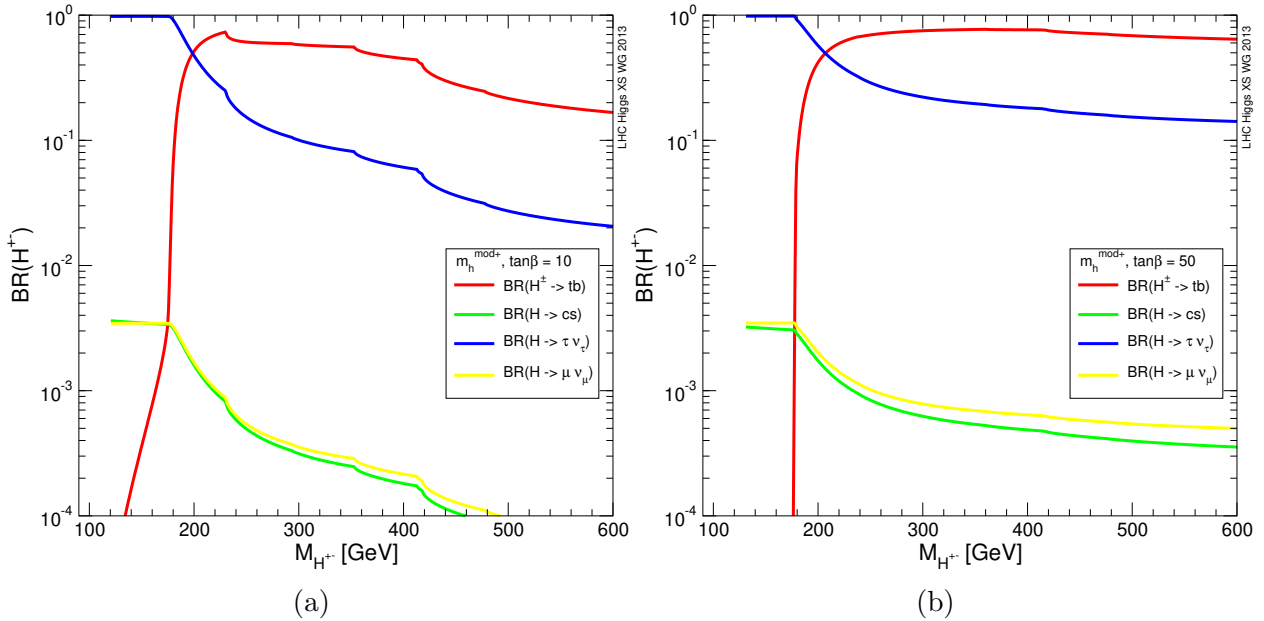


Figure 2.5: Branching ratios of H^\pm for (a) $\tan \beta = 10$ and (b) $\tan \beta = 50$ [7]

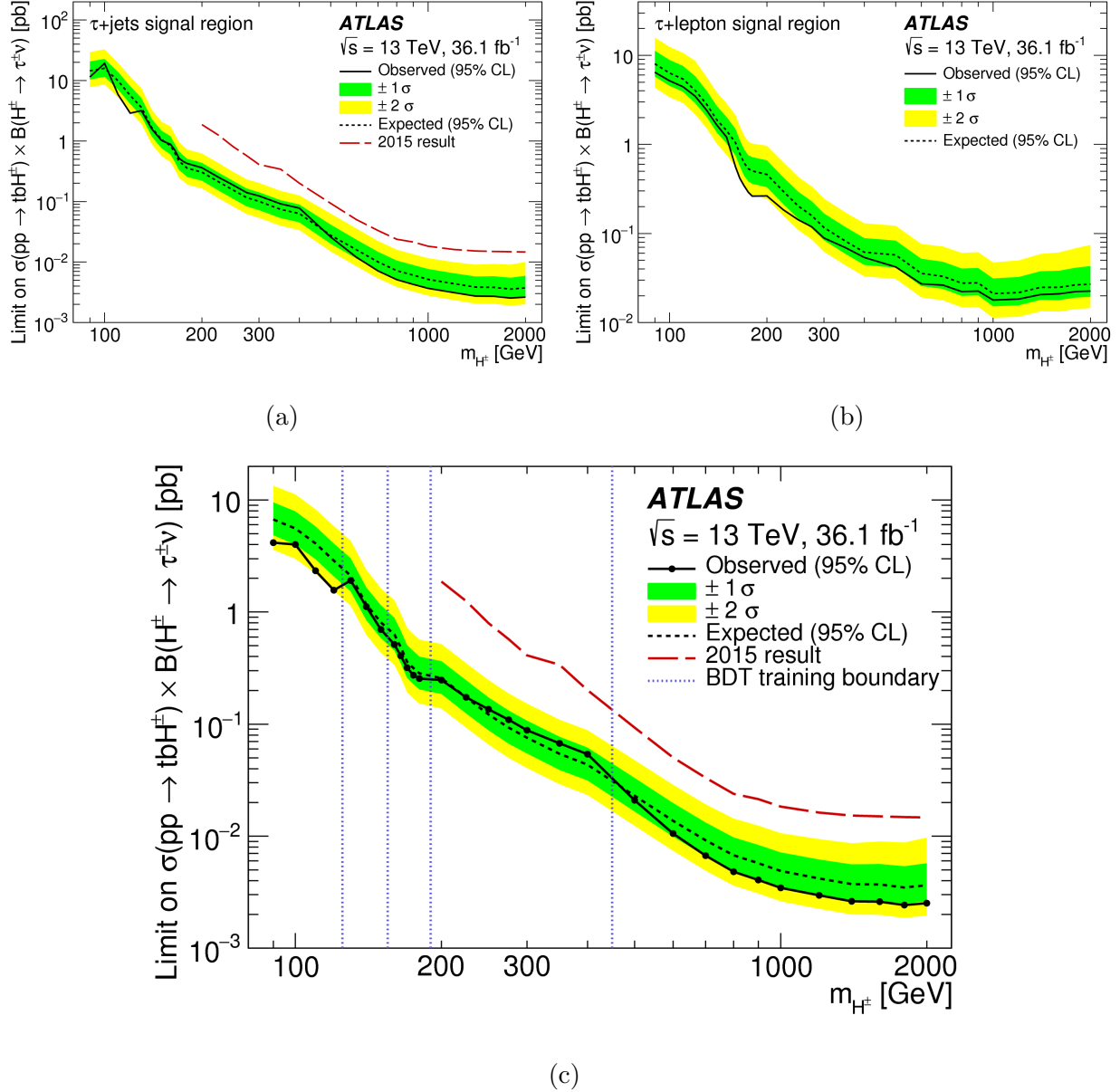


Figure 2.6: Limits on $\sigma(pp \rightarrow tbH^\pm x B(H^\pm \rightarrow \tau^\pm \nu)) [pb]$. (a) is for the $\tau + \text{jets}$ subchannel (b) corresponds to the $\tau + \ell$ subchannel and (c) is the combination of the two subchannels. [8]

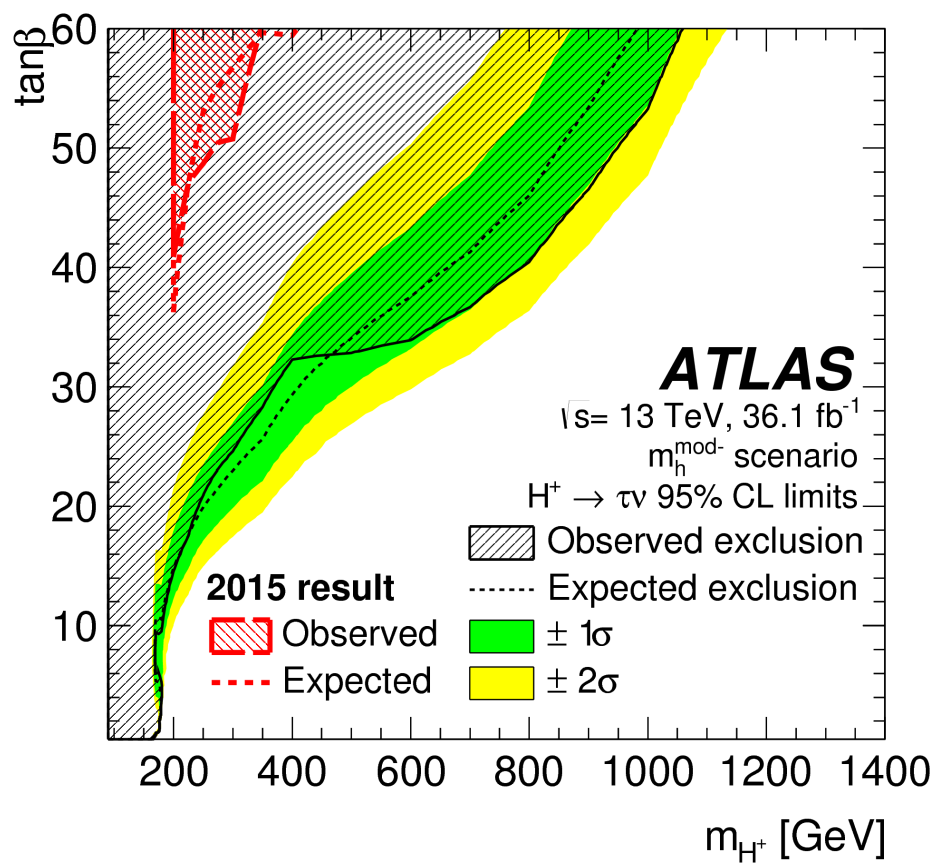


Figure 2.7: Limits on $\tan \beta$ as a function of m_{H^\pm} . [8]

CHAPTER 3

EXPERIMENTAL APPARATUS

3.1 Particle Accelerators

To study the Standard Model, the Higgs boson, and hints of new physics, particle accelerators are used. Particle accelerators can be categorized as either fixed target or colliders. As the naming suggest, in a fixed target accelerator the beam hits a target that then produces the desired particle collisions. Whereas a collider uses two opposite circulating beams that are then brought to collide inside a detector. A fixed target accelerator energy scales as $E_{CM} = \sqrt{E_{beam}}$ whereas a collider scales as $E_{CM} = 2 E_{beam}$.

3.1.1 Hadron Colliders

There are two main types of particle colliders, those that use hadrons and those that use leptons. Lepton colliders are often referred to as precision machines, as the longitude momentum is known and backgrounds are well understood. The center of mass energy is well controlled in a lepton collider, meaning particles can be produced on resonance. On the other hand, due to the nature of hadrons not being fundamental particles a hadron collider produces a wide range of collisions. The constituents of a hadron participate in the collisions, meaning it is impossible to know the exact longitude momentum of the initial state. It is because of this exact reason that hadron colliders are referred to as discovery machines. The synchrotron radiation produced from a hadron collider is much lower than that of a

lepton collider; meaning the beams are easier to control and can be pushed to higher energies without extra loses. The center of mass energy scales with $\frac{1}{m^4}$ in a hadron collider; again leading to an increased energy gain by simply using heavier particles.

3.1.2 The Large Hadron Collider

The Large Hadron Collider (LHC) is a 27 km circumference circular collider built outside of Geneva, Switzerland at CERN (Conseil Européen pour la Recherche Nucléaire). At center of mass energy 13.6 TeV, the LHC is the largest and highest energy particle accelerator ever built. There are four main collision points along the LHC: the ATLAS, CMS, ALICE, and LHCb experiments. ATLAS and CMS are general purpose particle detectors while ALICE and LHCb focus on heavy ion collisions. The numbers stated in the following sections are in reference to proton-proton collisions.

The LHC consists of 1104 NbTi superconducting dipole magnets, each being 15 m long, weighing 35 tonnes, cooled to 2 K, operating at 11,000 Amps, and produce a magnetic field of 8.3 T. A cross-section of a dipole magnet and the surrounding cryogenic system can be seen in figure 3.1. The dipole magnets are used to bend the beam around the ring with another 128 used in the beam dump system to remove the beam safely from the LHC. A 2-in-1 configuration is used within the dipole magnets to create the required magnetic fields to bend two equally charged beams in opposite directions. A diagram of the magnetic fields in this configuration produced can be seen in 3.2. To focus the beam in the horizontal and vertical planes two quadrupole magnets are used; one magnet focuses in one plane while defocusing in the other. The end result is a horizontally and vertically focused beam. While in the LHC, the hadrons are accelerated using radiofrequency cavities. Table 3.1 lists some information on the LHC.

Table 3.1: LHC parameters [9]

Circumference	26,659 m
Dipole operating temperature	1.9 K
Dipole magnets	1232
Quadrupole magnets	392
Radiofrequency cavities	16 (8 per beam)
Beam energy	6.5 TeV (13 CoM TeV)
Protons per bunch	1.2×10^{11}
Bunches per beam	2808
Revolutions per second	11245
Collisions per second	1,000,000,000

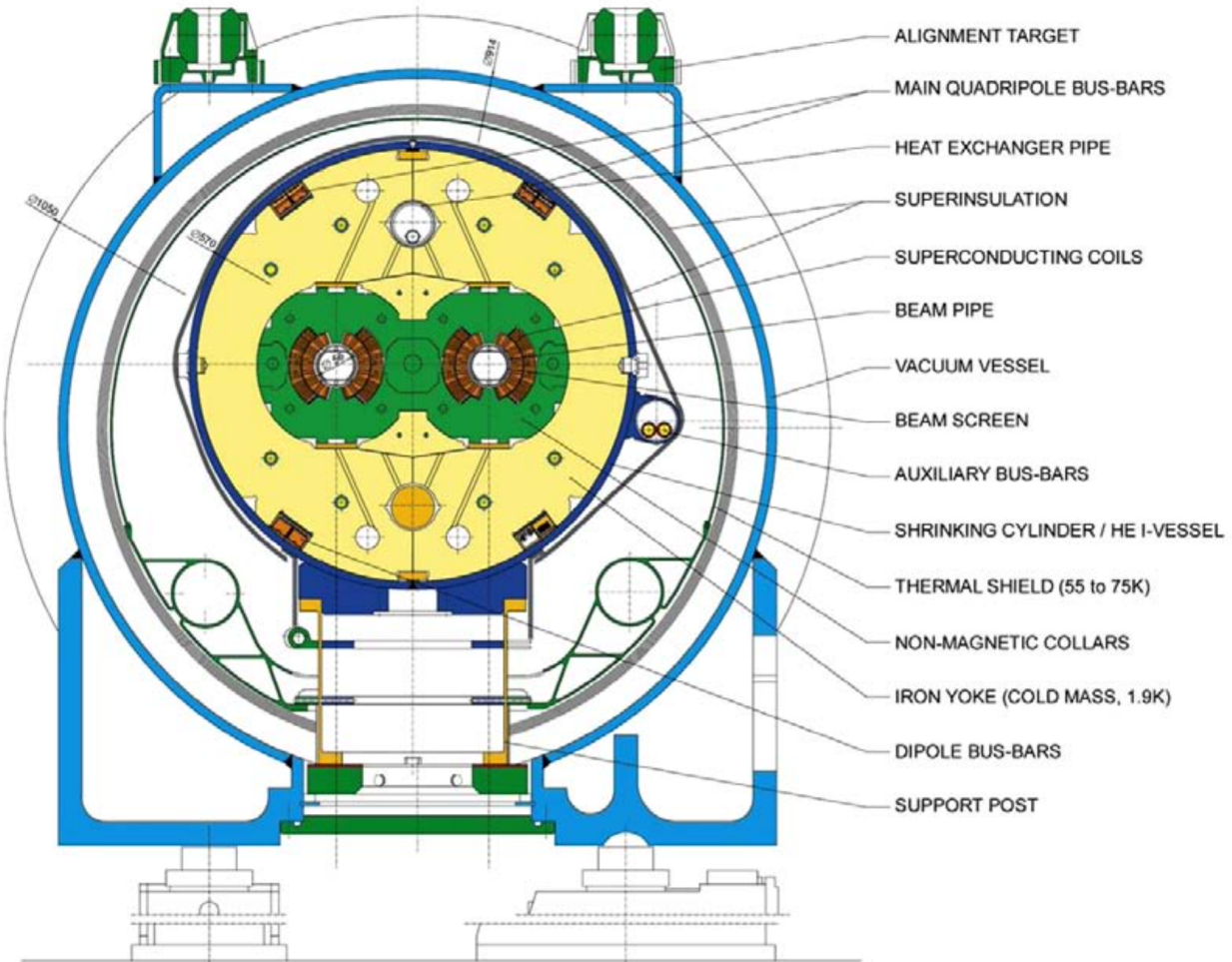


Figure 3.1: Cross-section of cryodipole (lengths in mm). [10]

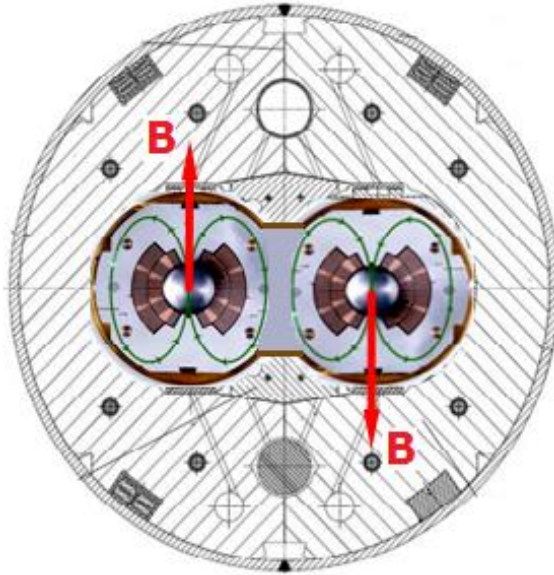


Figure 3.2: Field of the LHC dipole magnets. [11]

3.1.3 CERN Accelerator Complex

There are a series of accelerators used to get each beam up to its final energy of 6.5 TeV. The protons used in collisions are sourced from hydrogen atoms. The hydrogen is ionized, leaving the nucleus consisting of one proton, these protons are then accelerated in radiofrequency (RF) cavities. Figure 3.3 shows in detail the full accelerator complex at CERN.¹ The protons used in the LHC start the accelerating process in the linear accelerator LINAC 2. They then are accelerated in the booster, PS, SPS, and are finally injected at the LHC where they are accelerated to the final 6.5 TeV beam energy. The final energies of protons from each accelerator can be seen in Table 3.2.

¹Figure 3.3 shows the newer LINAC 4 at the start of Run-3. This work is concerning data taken with LINAC 2.

The CERN accelerator complex Complexe des accélérateurs du CERN

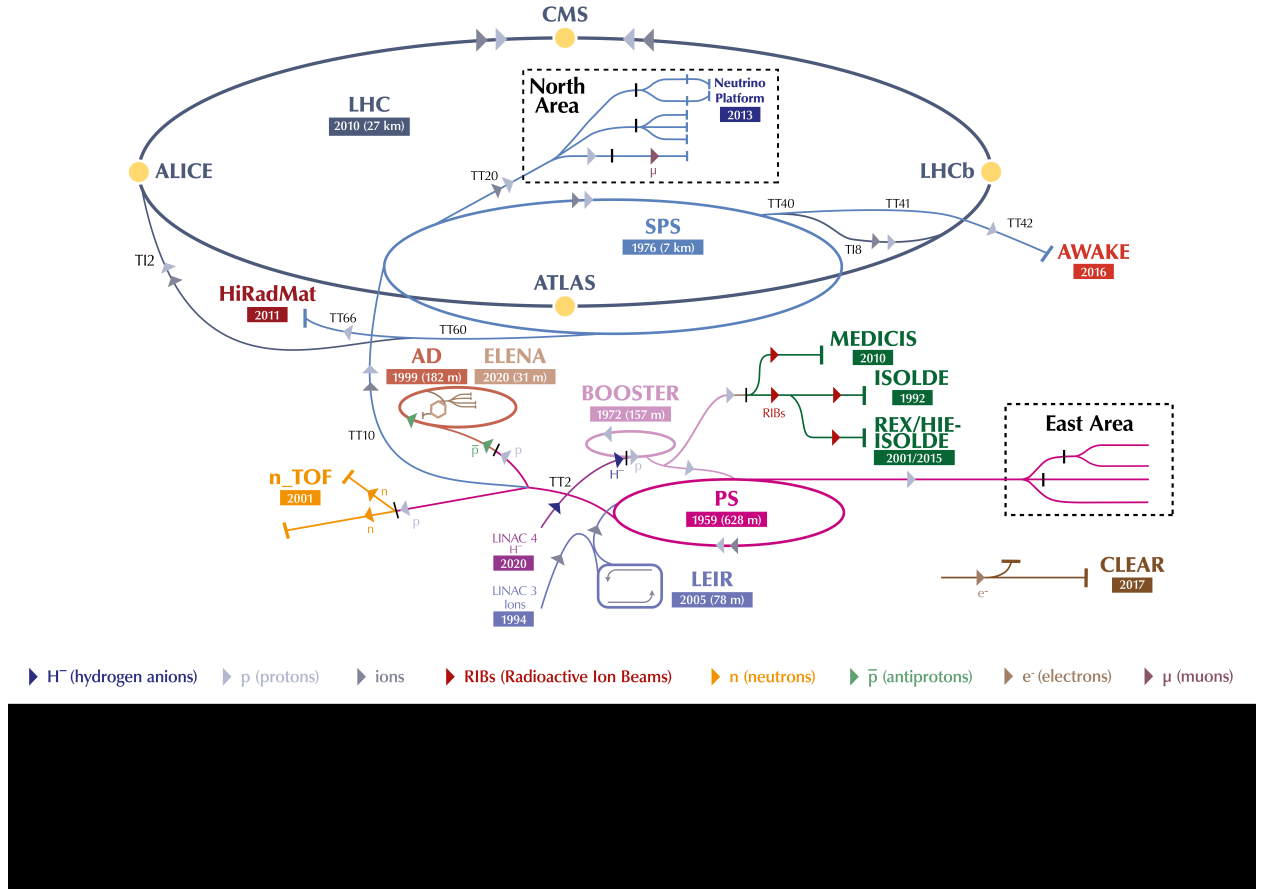


Figure 3.3: The CERN accelerator complex. [12]

Table 3.2: Accelerator final energies

Accelerator	Final Energy
LINAC 2	50 MeV
Booster	1.4 GeV
Proton Synchrotron (PS)	26 GeV
Super Proton Synchrotron (SPS)	450 GeV
Large Hadron Collider (LHC)	6.5 TeV

3.1.4 Luminosity

The amount of data collected from colliders is often referred to in terms of luminosity. Luminosity is measured in terms of inverse barns, where $1 b = 10^{-28} m^2$. Instantaneous luminosity of one bunch crossing can be written as

$$\mathcal{L}_{bunch} = \frac{\mu f}{\sigma} \quad (3.1)$$

where σ is the cross section and can be thought of as the probability of a collision occurring, μ is the number of inelastic interactions per bunch crossing, and f is the revolution frequency of the LHC $f = 11246$ Hz. Therefore, the total instantaneous luminosity is

$$\mathcal{L} = N_b \frac{\langle \mu \rangle f}{\sigma} \quad (3.2)$$

where $\langle \mu \rangle$ is the average number of inelastic interactions per bunch crossing.

The integrated luminosity then corresponds to the total amount of data that was taken during a time period and can be seen for the LHC Run-2 in 3.4 The value of $\langle \mu \rangle$ changed throughout data taking and can be seen in Figure 3.5 and is referred to as pileup because the higher the $\langle \mu \rangle$ value, the more messy a collision becomes. The effect of high pileup can be seen in Figure 3.6, a collision event taken in 2018 with 29 reconstructed vertices shown on the bottom right as colored circles.

A common calculation using the total integrated luminosity is shown in Equation 3.3; where the number of times a particular process was produced is calculated.

$$N_x = \mathcal{L} \sigma_x \quad (3.3)$$

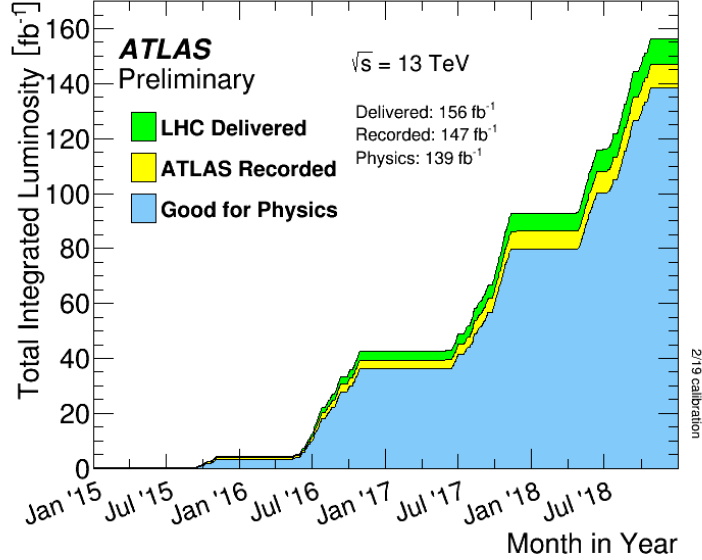


Figure 3.4: Cumulative luminosity versus time delivered to ATLAS (green), recorded by ATLAS (yellow), and certified to be good quality data (blue) during stable beams for pp collisions at 13 TeV center of mass energy in 2015-2018. The difference between the colored histograms reflects inefficiencies, especially those seen when restarting data taking.

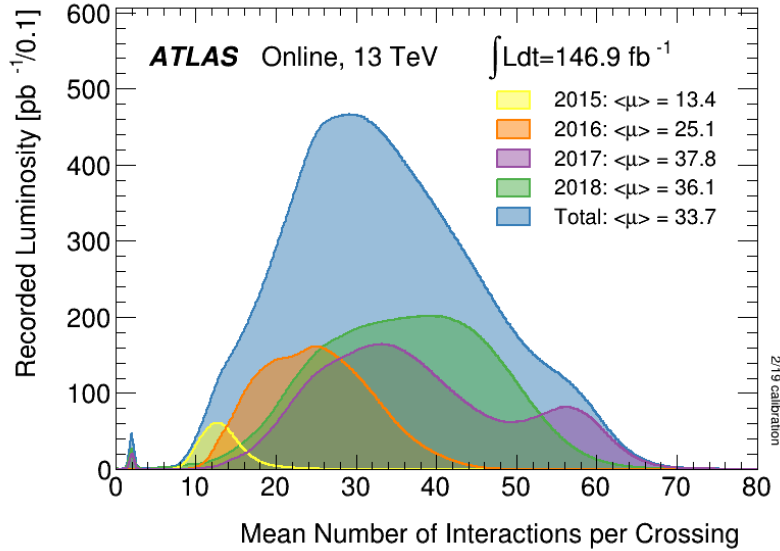


Figure 3.5: The luminosity-weighted distribution of the mean number of interactions per bunch crossing for the 2015-2018 pp collision dataset at 13 TeV center of mass energy.

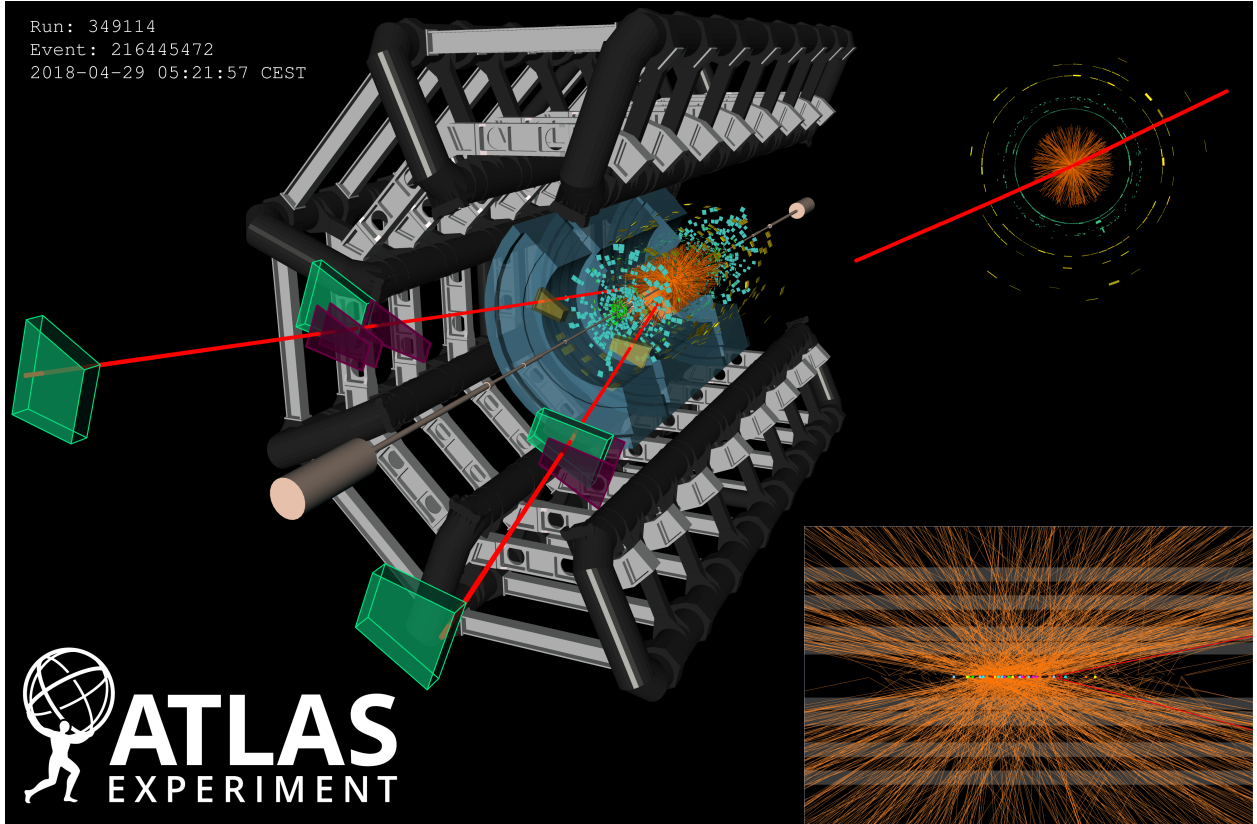


Figure 3.6: A display of a candidate Z boson event from proton-proton collisions recorded by ATLAS with LHC stable beams at a collision energy of 13 TeV. The Z boson candidate is reconstructed in a beam crossing with 28 additionally reconstructed primary vertices from the minimum bias interactions. The candidate event is reconstructed in the 2μ final state. In the left display, the red lines show the path of the two muons including the hits in the muon spectrometer and the yellow tracks are the remaining charged particles from the 29 vertices, with transverse momentum above 0.5 GeV. The colored squares in the lower display correspond to the position of the reconstructed vertices. The invariant mass of the two muons is 92.3 GeV.

where again, σ is the cross section. In this case, the cross section corresponding to process x .

3.2 The ATLAS Detector

The ATLAS (**A** Toroidal LHC Apparatu**S**) detector is one of two general purpose particle detectors on the LHC. The other being the **C**ompact **M**uon **S**olenoid (CMS). ATLAS,

like other particle detectors, is comprised of four main components; the inner detector, calorimeters, muon system, and the magnet system. Each component has several types of technology in order to measure the energy of all possible particle decays.² The full ATLAS detector measures 44 m in length, 25 m in diameter, and weighs over 7000 tonnes. Figure 3.7 shows a 3D model of the ATLAS detector.³ All of the subdetectors output data to the Trigger and Data Acquisition (TDAQ) system that selects collisions with interesting physics using a complex mix of hardware and software algorithms detailed in 3.2.6.

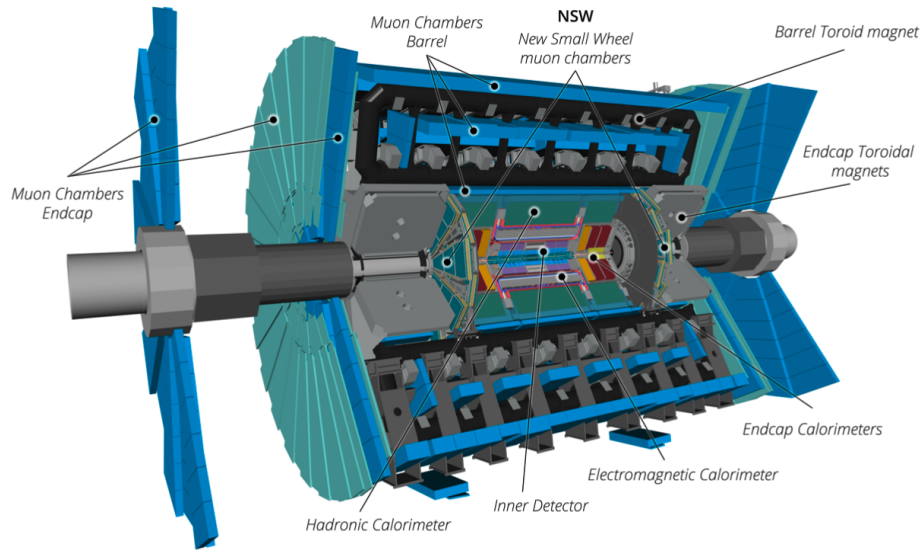


Figure 3.7: Cut-away view of the ATLAS detector with major subdetectors highlighted.

3.2.1 Detector Coordinates

Since ATLAS is a cylinder, it is convenient to start with polar cylindrical coordinates. For ATLAS, the z-axis is inline with the beam line, the x-axis points towards the center of the

²Neutrinos are not directly detected, but inferred via a missing transverse energy calculation described in Section 5.7.

³Figure 3.7 shows the New Small Wheel muon-chambers. This dissertation concerns data collected with the old Small Wheel muon-chambers.

LHC ring, and the y-axis points vertically. However, since particle collisions are relativistic by nature, a set of Lorentz invariant coordinates is much more useful. The radial coordinate r defines the radial distance from the interaction point (IP) at the center of ATLAS, ϕ is the azimuthal angle describing the angle from the x-axis in, and η , the pseudorapidity, is defined as

$$\eta \equiv -\ln(\tan(\frac{\theta}{2})) \quad (3.4)$$

where θ is the angle from the y-axis. It is in the differences in η between particles that provides the Lorentz invariance in this coordinate system of (r, ϕ, η) . Due to the large collision energies of the LHC, the pseudorapidity is a close estimate to the true rapidity of the particles.

$$y \equiv \frac{1}{2} \ln\left(\frac{E + p_Z}{E - p_Z}\right) \approx \eta \quad (3.5)$$

When speaking of differences in particle locations within ATLAS, ΔR is often used.

$$\Delta R \equiv \sqrt{(\Delta\eta)^2 + (\Delta\phi)^2} \quad (3.6)$$

Figure 3.8 shows visually how η relates to θ . In the ATLAS detector, the central barrel section corresponds to a range of $|\eta| < 1$.

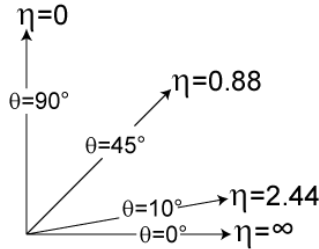


Figure 3.8: A diagram showing the pseudorapidity η and corresponding θ values. [13]

3.2.2 Magnet Systems

The ATLAS detector makes use of two superconducting magnet systems; a central solenoid and a toroid system. Both systems provide large magnetic fields to curve charged particles. The curvature can be used to measure the electromagnetic charge and charge to mass ratio, effectively measuring the momentum of charged particles. Figure 3.9 shows the magnets in ATLAS.

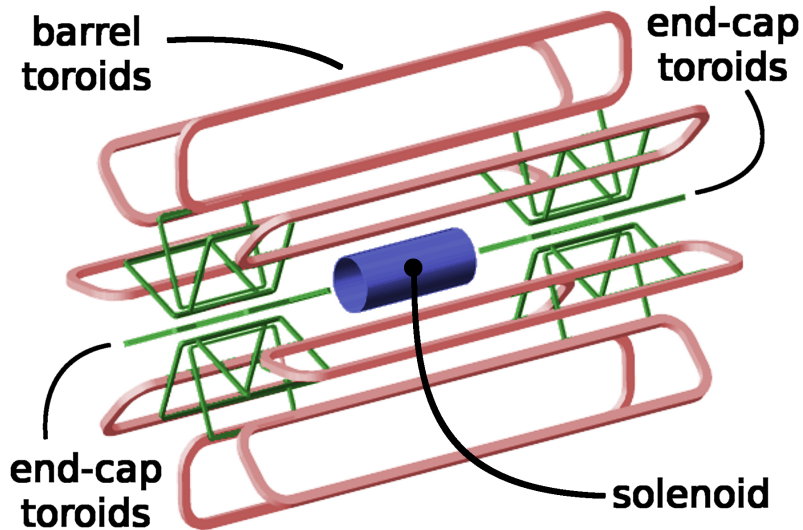


Figure 3.9: The ATLAS magnet systems.

3.2.2.1 Solenoid System

The central solenoid encases the Inner Detector (ID), creating an axially symmetric 2 T magnetic field. This magnetic field bends charged particles in the transverse plane throughout the ID. The solenoid magnet itself measures 5.3 m in length and 2.63 m in diameter. In an effort to decrease the amount of material in front of the calorimeters the solenoid magnet was made to be thin. It is a single-layer coil with approximately 1200 turns

of NbTi superconducting wires encased in Al-Cu to structurally stabilize the magnet material [14]. The steel structure within the Tile calorimeter acts as the magnetic flux return for the solenoid magnet system. 70% of this flux passes through the supporting girder structure, 25% through the active calorimeter material, and roughly 2% through the front-plates of the Tile calorimeter [15].

3.2.2.2 Toroid System

The ATLAS detector gets its name from the toroid magnetic system that is critical in the identification of high energy muons. The toroid system bends any charged particles that make it past the calorimeters along the beam axis. This is achieved through a radially symmetric magnetic field of 3.9 T in the barrel and 4.1 in the end-caps. The barrel toroid system is comprised of 8 air core superconducting toroid magnets that each measure 25 m in length, 10 m in diameter, and weigh 750 tonnes. The superconducting wires are the same used in the solenoid, NbTi encased in Al-Cu [16]. Each magnet is encased in a stainless steel cryogenic chamber, or cryostat. The toroid magnet system has two end-cap toroids that are very similar in construction to the barrel toroids. The end-cap toroids also have 8 coils measuring 5 m in length and 10 m in diameter. Instead of individual cryostats for each coil, the end-caps are encased in large cryostats that hold all 8 coils. This allows the end-caps to be pulled out and offers easy access to the rest of the detector. Just like with the central solenoid system, the design of the toroid system was chosen to limit the amount of material between detector components. A solenoid magnet of similar size to the toroid system would not only add more material, but would be cost prohibitive as well.

3.2.3 Inner Detector

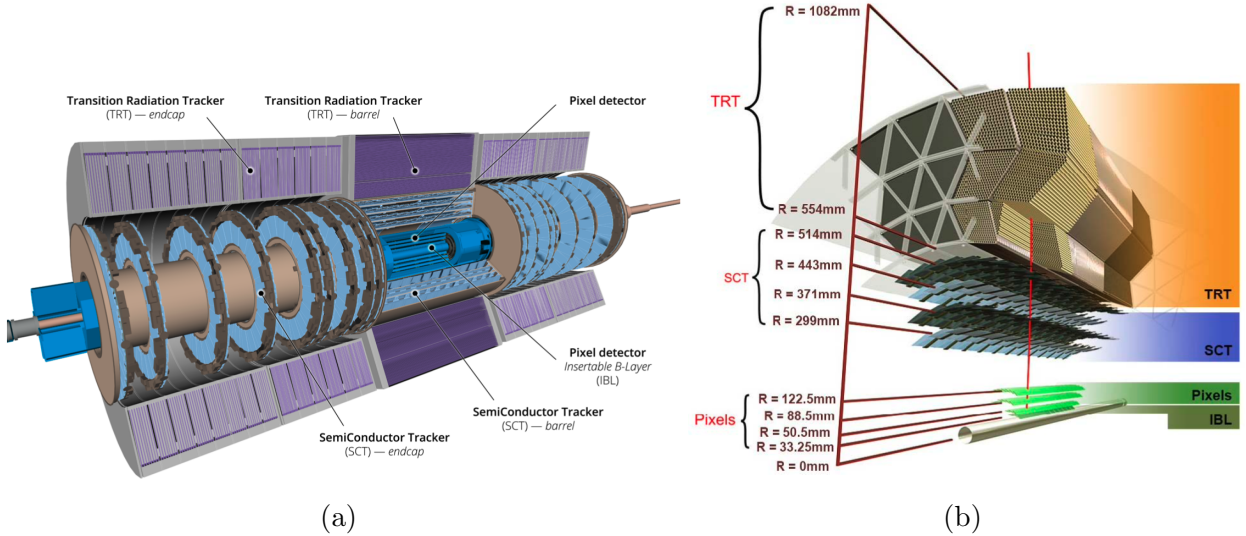


Figure 3.10: (a) Cut-away view of the ATLAS Inner Detector. (b) Cross-sectional view of the ATLAS Inner Detector.

The ID is the inner-most detector, closest to the IP and is used to track the trajectory of charged particles leading to the measurement of electromagnetic charge and momentum. The ID is immersed in the 2 T magnetic field provided by the central solenoid described in section 3.2.2.1 and covers a pseudorapidity range of $|\eta| < 2.5$. The three subdetectors within the ID can be seen in Figure 3.10, the Pixel, Semiconductor Tracker (SCT), and the Transition Radiation Tracker (TRT). Like the toroid system, and many of the other subdetectors, the ID is comprised of barrel and end-cap segments. The ID barrel section is 1.6 m in length and covers $|\eta| < 1$ while the end-caps measure over 7 m in length and cover $1 < |\eta| < 2.5$.

A track is considered good if there are hits in at least 3 pixel layers and 8 strips. The ID tracking system was designed with a resolution of

$$\frac{\sigma_{p_T}}{p_T} = 0.05\% p_T \oplus 1\% \quad (3.7)$$

3.2.3.1 Pixel

The detector closest to the beam and IP is the Pixel Detector. The Pixel Detector is designed to measure with high-precision and high-granularity. The barrel Pixel detector consists of three layers of n-type silicon substrate with n-type implants. The closest layer to the IP sits at 50.5 mm and the outermost layer extends out to 12 cm. This combination gives the Pixel Detector the ability to determine the impact parameters of collisions with incredible precision. Due to the high radiation dose this close to the IP, the Pixel Detector was designed to be operated only in partial depletion. Each pixel cell measures $200\mu m \times 400\mu m \times 250\mu m$. There are five Pixel disks on each end-cap of the ID. In total there are 1,744 modules, 46,080 readout channels per module, giving over 80 million channels with a spatial resolution of $10\mu m(R - \phi) \times 115\mu m(z)$ [17].

In order to keep up with the increased demand of Run-2 data taking conditions, an additional layer of pixels was installed in the Long Shutdown 1 (LS1) between 2013 and 2015. This Insertable **B** Layer (IBL) provides even finer granularity tracking with pixel cells measuring $50\mu m \times 250\mu m$ installed at a radial distance of $R = 33.25$ mm from the IP and a spatial resolution of $8\mu m(R - \phi) \times 40\mu m(z)$ [18]. The IBL has proved incredibly useful in the reconstruction of displaced vertices from processes like b -jet hadronization and $\gamma \rightarrow e^+e^-$.

3.2.3.2 Semiconductor Tracker

Moving radially outward, the next subdetector is the SCT that provides tracking in the intermediate radial range from the IP and covers a range of $|\eta| < 2.5$. Similar to the Pixel Detector, the SCT has 4 barrel layers and 9 end-cap wheels on each side. The SCT provides four measurements per track via silicon microstrip detectors. Each microstrip is made of two

$6.36 \times 6.40 \text{ cm}^2$ detectors glued end to end so each microstrip is 12.8 cm long. Two microstrips are then glued back to back with a $40 \mu\text{rad}$ angle. In total there are 768 strips, giving 6.2 million readout channels. The SCT has a spatial resolution of $17 \mu\text{m}(R - \phi) \times 580 \mu\text{m}(z)$ and can distinguish tracks with as small as a $200 \mu\text{m}$ separation [19].

3.2.3.3 Transition Radiation Tracker

The final subdetector of the ID is the TRT ($R = 554 \text{ mm} - 1082 \text{ mm}$) . Instead of silicon detectors the TRT uses 4 mm diameter straw tubes; a hollow tube with a sense wire held at high voltage in the middle. The max length of a straw is 150 cm. The straws are filled with a gaseous mixture of 70% Xe, 27% CO₂, 3% O₂.⁴ Charged particles ionize the gas mixture, thereby releasing an electron and an ion. The ion drifts to the straw surface and the electron drifts to the wire; this charge drift is then measured as a signal. The TRT checks the signals against two thresholds, a lower threshold for measuring the drift time to derive a position and a higher threshold that is used to identify transition radiation X-rays. The higher threshold provides discriminating power between charged pions and electrons.

The TRT consists of a barrel section and 18 wheels in each end-cap. In the barrel, there are 50,000 straws divided in two at the center to allow for two separate readouts. The end-caps have 320,000 straws. In total, there are 420,000 readout channels. Each straw provides a spatial resolution of $170 \mu\text{m}$. [19]

⁴During Run-2 the Xe was replaced with Ar as a cost saving measure. Ar provides similar performance as Xe in tracking, but is less efficient in absorbing X-rays from transition radiation.

3.2.4 Calorimeters

The ATLAS detector makes use of two types of sampling calorimeters, one that uses liquid argon as the active medium and another that uses scintillating plastic tiles. Both types of calorimeters are designed to fully absorb particles via showering. Incoming particles interact with an absorber material and generate secondary particles. Those secondary particles interact with the absorber and create another set of particles. This cascading effect creates showers of particles inside the calorimeters. The shape and depth of these particles is important in the design choices for the calorimeters as well as particle identification. Two helpful variables when talking about shower depth are radiation length χ_0 and nuclear interaction length λ . χ_0 is defined as the distance where a particle has lost energy via bremsstrahlung equal to $\frac{1}{e}$.⁵ Whereas λ is the mean free path of a hadron before undergoing an inelastic nuclear interaction. In order to fully absorb a wide energy range of incident particles the calorimeters are such that any path through them is at least $25 \chi_0$ or 10λ . Figure 3.11 shows the calorimeters and their nuclear interaction lengths as a function of η .

The design resolution of the calorimeters can be seen in Table 3.3.

Table 3.3: Design resolution of EM and hadronic calorimeters in the ATLAS Detector.

Calorimeter	Pseudorapidity range	Resolution
Electromagnetic	$ \eta < 3.2$	$\frac{\sigma}{E} = \frac{10\%}{\sqrt{E}} \oplus 0.7\%$
Hadronic	$ \eta < 3.2$ $3.1 < \eta < 4.9$	$\frac{\sigma}{E} = \frac{50\%}{\sqrt{E}} \oplus 3\%$ $\frac{\sigma}{E} = \frac{100\%}{\sqrt{E}} \oplus 10\%$

The layout of calorimeters in the ATLAS detector can be seen in Figure 3.12.

⁵ χ_0 can also be defined as $\frac{7}{9}$ of the mean free path of a high energy photon.

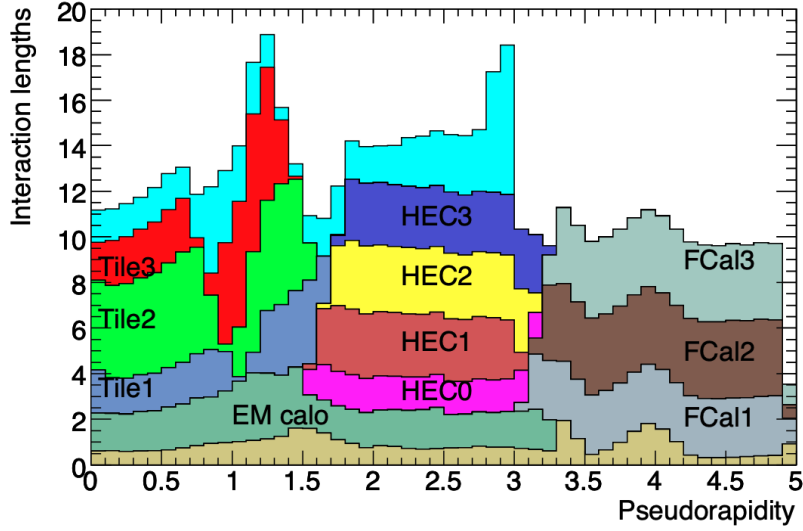


Figure 3.11: Interaction lengths as a function of η in the ATLAS calorimeters. The unlabeled brown color is the material in front of the EM calorimeters and the unlabeled cyan is the amount of material in front of the first active layer of the muon spectrometer. [20]

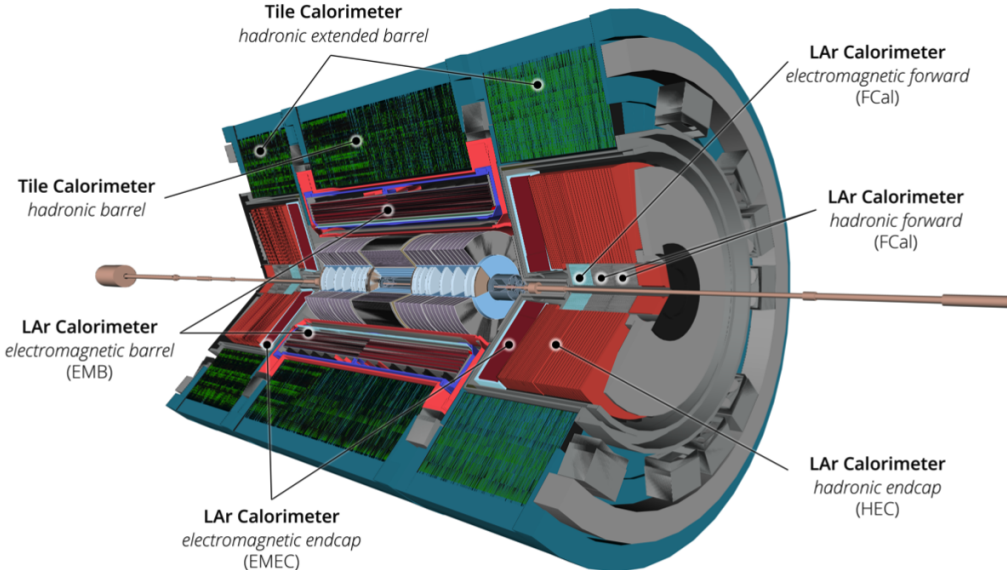


Figure 3.12: Cut-out view of the ATLAS detector's calorimeters.

3.2.4.1 Liquid Argon Calorimeters

A liquid argon (LAr) is based on a similar principle to the straw tubes of the TRT described in section 3.2.3.3. In this case, the LAr is the active medium that is ionized by the incoming particle. The free electron then drifts to an electrode, copper-tungsten in the case of the barrel LAr calorimeter. The drifting electrons are then readout as an electrical signal; there are approximately 180,000 LAr readout channels in the ATLAS detector. LAr was chosen as the active medium due to it's intrinsic radiation hardness, stability over time, and linear response. The LAr must be kept at very cold temperatures, around 85 K. To achieve this, the LAr calorimeters are kept in cryostats, the barrel calorimeter shares the cryostat and vacuum with the central solenoid.

There are four LAr calorimeters within the ATLAS detector. The main barrel section (EMB) is designed for electromagnetic calorimetry with a lead-stainless steel absorber and covers a pseudorapidity range of $|\eta| < 2.5$. Next in η is the LAr Electromagnetic End-Cap (EMEC) that also uses lead-stainless steel absorber and the LAr Hadronic End-Cap (HEC) which has a copper plate absorber; both EMEC and HEC cover $1.5 < |\eta| < 3.2$. The final LAr calorimeter is the aptly named Forward Calorimeter (FCAL) that covers $|\eta| < 4.9$ and has three modules. The first is optimized for EM calorimetry and uses a copper absorber. The other two FCAL modules are used to measure hadronic showers and use tungsten absorbers.

The EMB and EMEC both utilize an accordion geometry pictured in Figure 3.13 to ensure a full ϕ coverage. The EMB consists of four layers, the first being a LAr presampler of 1.1 cm thickness. The presampler is used to correct for energy losses due to material in front of the calorimeter. The first layer after the presampler is finely segmented to ensure good position measurements. The second layer is $16\chi_0$ thick and collects most of the electromagnetic

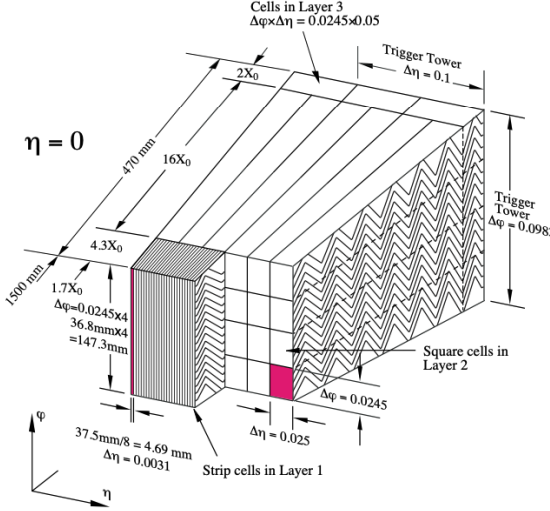


Figure 3.13: A EMB module showing the accordion geometry and granularity. [20]

showers. Typically, only the tails of EM showers make it to the third and final layer, so a coarser granularity is used.

3.2.4.2 Tile Calorimeter

The hadronic Tile Calorimeter (TileCal) is a sampling calorimeter that is designed to fully absorb hadronic showers covering a range of $|\eta| < 1.7$ at a radial distance of $2.28\text{ m} \leq R \leq 4.25\text{ m}$ from the IP. This radial distance translates to approximately 7.4λ . A similar design of absorber and electrode is used in TileCal to capture the full energy of hadronic showers. TileCal uses a steel absorber. However, instead of a liquid or gas being ionized and the free electrons being collected as a signal, TileCal takes advantage of a special material called scintillating plastic. When an ionizing particle interacts with the scintillating plastic, light is created; this light is absorbed in wavelength shifting (WLS) fibers. It is then re-emitted and transmitted to photomultiplier tubes (PMTs). The PMT signal is then shaped, amplified at two gains with a ratio of 64:1, then digitized at 40 MHz with 10-bit

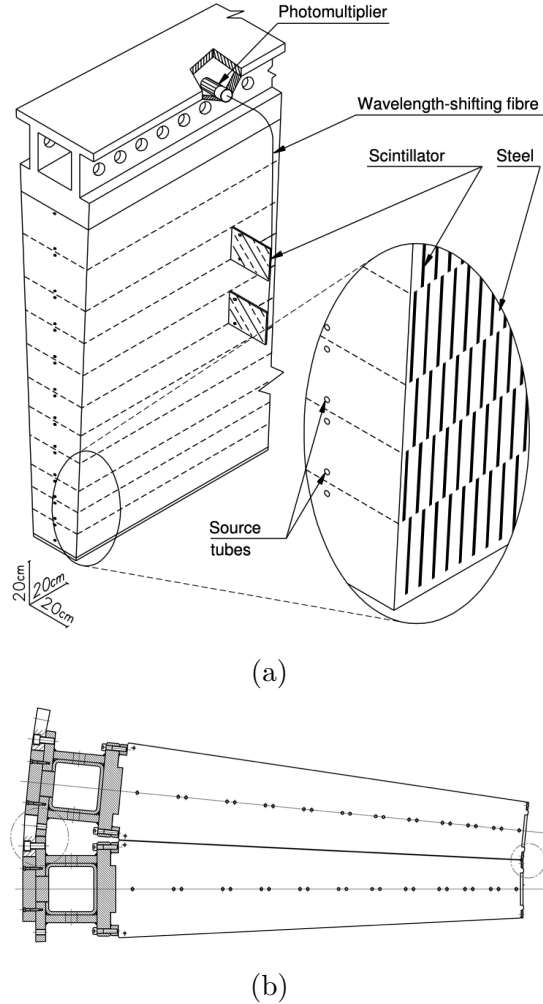


Figure 3.14: (a) Diagram of an individual TileCal module. (b) Azimuthal view of two TileCal modules with the IP being to the right.

analogue-to-digital converters (ADCs). Each cell within TileCal has 2 PMTs, giving over 10,000 readout channels. There are 256 modules within TileCal. A diagram of an individual module and the layout of two modules side-by-side can be seen in Figure 3.14.

A significant fraction of the author's time and effort during their PhD went to data quality monitoring and maintenance of TileCal. These works are detailed in Appendix A.

3.2.5 Muon Spectrometer

High momentum muons provide a vital signature at the LHC. Muons are minimally ionizing particles, meaning they leave a small amount of energy inside detectors and travel to the edge and beyond the volume of the ATLAS detector. Instead of attempting to fully absorb muons, high precision position measurements are taken to track their trajectories. The toroid magnet system described in section 3.2.2.2 is an integral part of the Muon Spectrometer (MS); it provides the bending force, changing the trajectories to the direction of the beamline. The barrel section of the MS compo consists of three concentric cylindrical shells at $R = 5\text{ m}, 7.5\text{ m}, 10\text{ m}$ made of Monitored Drift Tubes (MDTs) ($|\eta| < 1$). [21] These cylindrical shells sit in-between and on the air core toroid magnets. On the 2nd and 3rd shells are Resistive Plate Chambers (RPCs) that provide quick triggering. Complimenting the barrel section are the end-caps, referred to as wheels for the MS compo. The wheels are placed at $|z| \approx 7.4\text{ m}, 10.8\text{ m}, 14\text{ m}$, and 21.5 m ($2.0 < |\eta| < 2.7$). The innermost layer of these wheels experience the highest rates of incident particles. To cope with this, Cathode Strip Chambers (CSCs) with a finer granularity than the MDTs that are used in the barrel. Similarly, Thin Gap Chambers (TGCs) are used for triggering instead of RPCs. These wheels provide spatial coordinates orthogonal to those of the precision-tracking MDTs in the barrel. Figure 3.15 shows the positioning of the various MS components.⁶

⁶Figure 3.15 Shows the New Small Wheel (NSW). The NSW is an upgrade to the old Small Wheels that were used in the data taking period that concerns this dissertation.

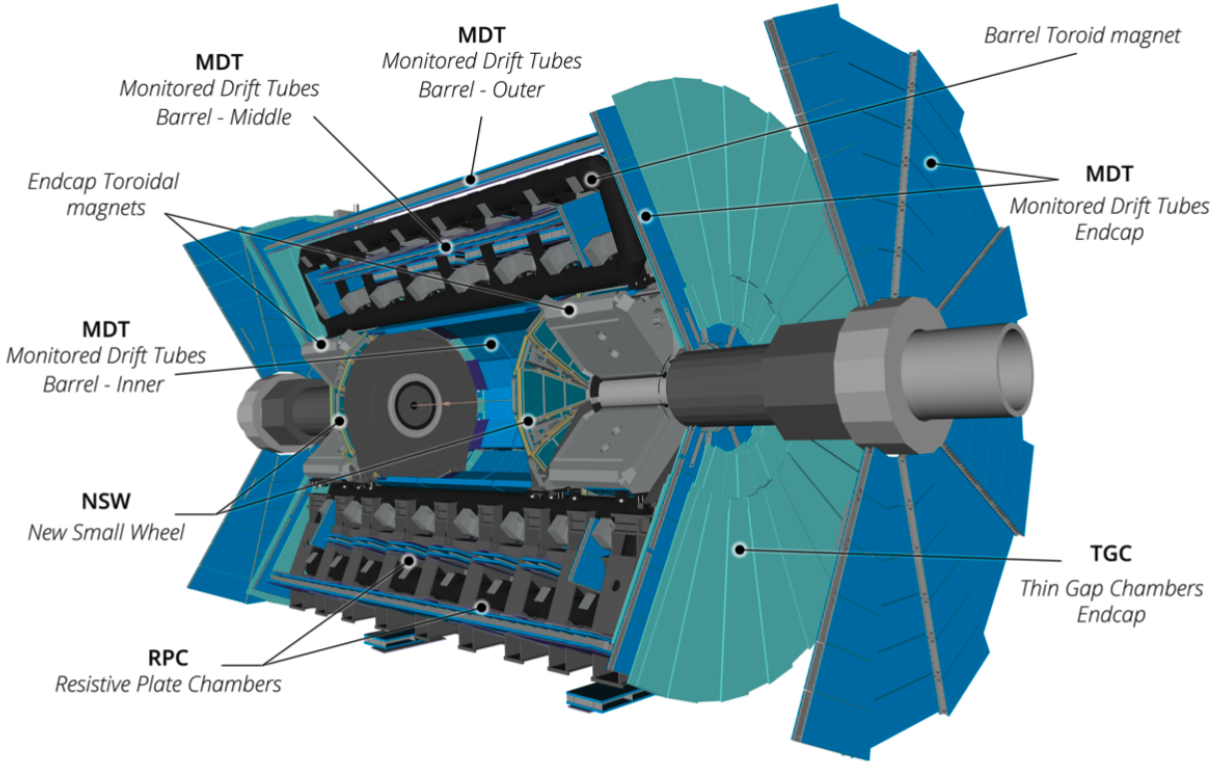


Figure 3.15: Cut-out view of the ATLAS detector Muon Spectrometer.

3.2.6 Trigger System

The high luminosity provided by the LHC is critical in collecting enough data to make detailed physics analyses. However, it also means that there is an incredibly large amount of data to sort through. So much that it is not possible to write out the data from every bunch crossing. As shown in Figure 3.6, even one single event can contain an inordinate amount of data. Another issue arises due to the nature of hadron collisions; in that not all bunch crossing provide hard scatter inelastic collisions that are “interesting” enough to save data on.

To solve this issue, the data coming out of ATLAS is combed through in real time at a variable rate of 1 kHz to 40 MHz. This is done with a Trigger and Data Acquisition (TDAQ)

system. The TDAQ system used in Run-2 is described in detail here: [22]. The TDAQ system reads in data from the ATLAS detector, calculates relevant quantities, and makes a decision on if there was an event worth storing. A diagram showing the data flow into the TDAQ system is shown in 3.16.⁷ The ATLAS TDAQ system consists of two main components, Level-1

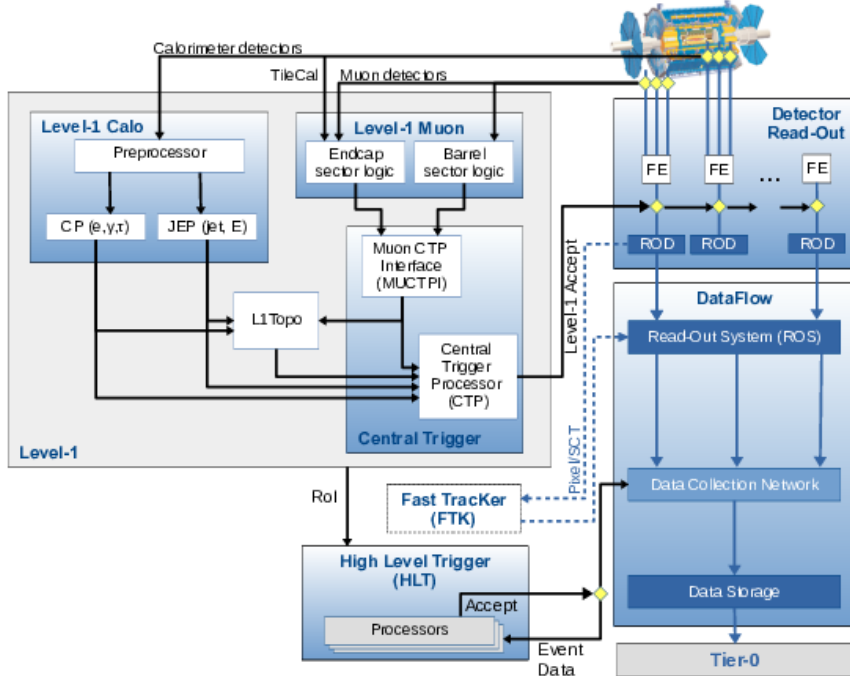


Figure 3.16: The ATLAS TDAQ system in Run-2 showing the components relevant for triggering as well as the detector read-out and data flow.

(L1) and High Level Trigger (HLT). The L1 trigger is a hardware based trigger system that reads in data from the calorimeters and muon spectrometer. The L1 trigger has a latency of $2.5\ \mu\text{s}$ and can read-out accepted events up to 100 kHz, the detector maximum readout

⁷Figure 3.16 shows the Fast TracKer (FTK). During Run 2 FTK was undergoing commissioning and was not used in the active TDAQ system.

rate. The HLT is a software based trigger system based on the offline reconstruction software. During Run-2 the HLT operated with an average output rate of 1.2 kHz, which translates to about 1.2 GB/s of data sent to permanent storage.

After the TDAQ system accepts an event, the data is set to be stored on magnetic tape for long term storage. It is also processed at the local computing farm named Tier-0 with the full reconstruction software suite described in Chapter 5.

CHAPTER 4

SIMULATION

The data collected by the ATLAS experiment must be compared to a control. This control is most often a dataset of simulation particle collisions that approximate to great precision physics processes and particle interaction with detector material, as well as the detector's response. Figure 4.1 shows the chain of simulations these datasets are produced by.

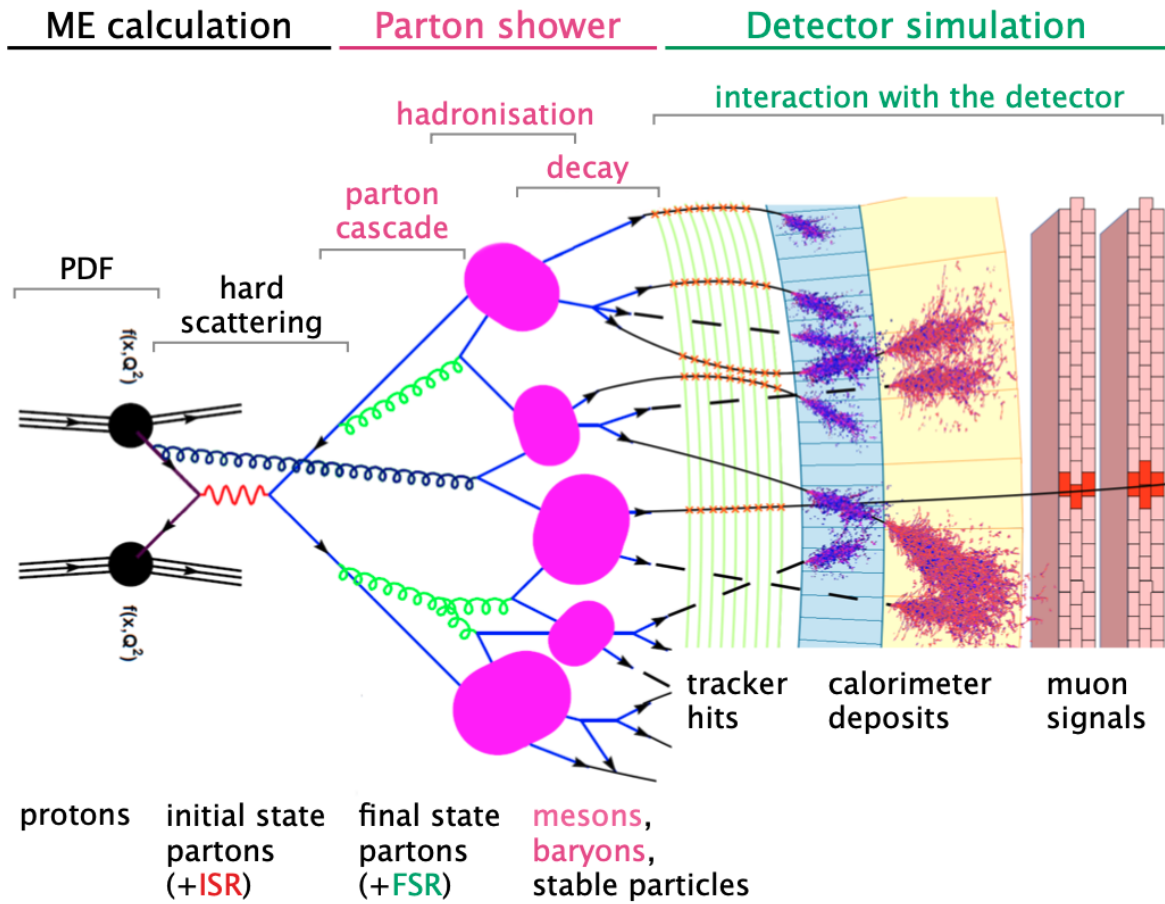


Figure 4.1: A pictorial representation of the simulation chain used in the ATLAS experiment. [23]

Many particle physics experiments, ATLAS included, use Monte Carlo (MC) simulation techniques to produce these datasets. Monte Carlo simulation techniques use repeated random sampling of underlying probability density functions to closely model various processes.

4.1 Event Generation and Hadronization

Since protons and other hadrons are not fundamental particles, it is impossible to know the exact constituents (partons) that interacted during a collision. To mimic this intrinsic probabilistic nature, Parton Distribution Functions (PDFs) are used. Where a PDF models the probability of any parton within a proton (or hadron) to carry a fraction of the beam energy as momentum. The PDF and subsequent inelastic hard scattering of the interacting partons are modeled via a Matrix Element (ME) calculation, often depicted through Feynman diagrams. This ME calculation is done to fixed order in perturbation theory, leading order (LO), next-to-leading order (NLO), leading-logarithmic order (LL), etc. This first level event generation can be done by a myriad of MC event generators. Often specific choices are made based on individual generator performance for a given physics process.

The next step in the simulation chain is the parton showering or hadronization. This is often done with a completely different set of MC generators. Hadronization is a complex, computationally expensive step to simulate and is done through iteratively. An example of a parton shower generator output can be seen in figure 4.2.

4.2 Detector Simulation

The final step in the simulation chain is simulating the particle's interaction with the detector material and the detector's response. Up until this point, the MC generators used are

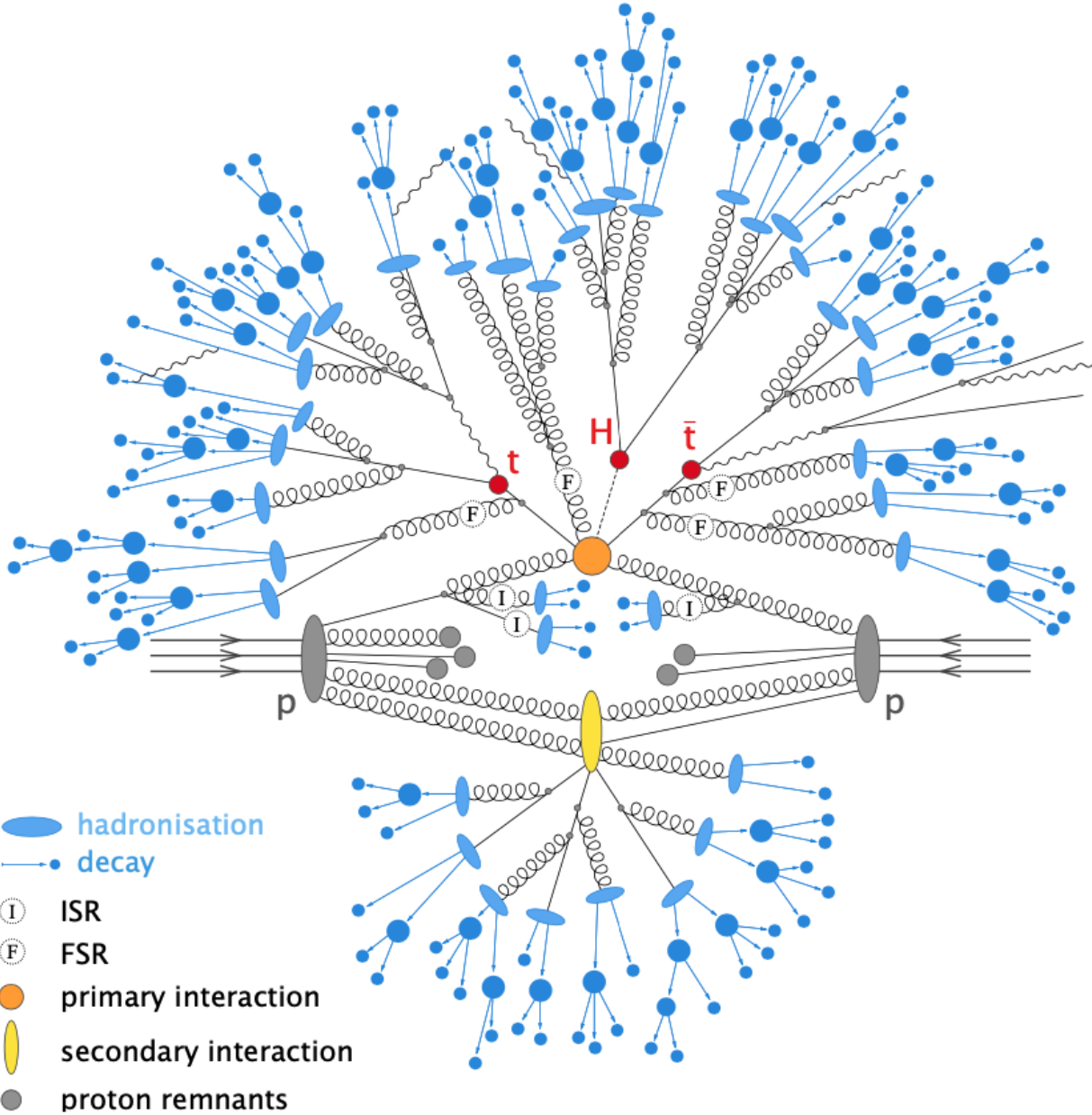


Figure 4.2: A pictorial representation of a parton shower of a $t\bar{t}H$ event. [23]

generic non-experiment dependent simulations. The ATLAS collaboration uses a GEANT4 based generator suite to simulate these interactions. [24] These simulations are incredibly detailed, including all support structure, material densities, readout electronics, digitization,

etc. The final simulated dataset is output into a raw data format identical to real data coming off of the ATLAS detector.

CHAPTER 5

EVENT RECONSTRUCTION

Before any physics analysis can be performed on the raw data from the ATLAS detector and MC simulations both raw datasets go through a reconstruction software suite called Athena. Various algorithms are employed to identify energy deposits as particles based on shower shapes, tracker hits, calculated charge to mass ratios, etc. Figure 5.1 shows the signatures of various particles within the ATLAS detector.

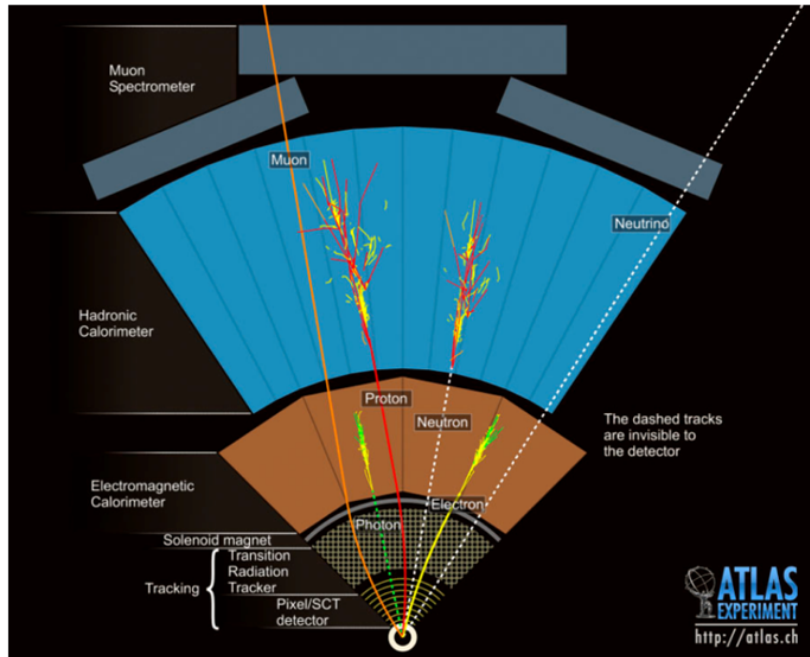


Figure 5.1: Cross section view of the ATLAS detector with subdetectors labeled. Various types of particles radial trajectories are shown.

The following sections detail the identification processes of muons, electrons, photons, jets, τ leptons, and a calculated quantity called missing transverse energy (E_T^{miss}). These reconstructed physics objects are the inputs to the majority of physics analyses.

5.1 Tracks

Tracks are fits connected three dimensional space-points in the ID. These space-points are created from clusters of hits in the ID. A set of three space-points are combined into one track seed, then fed into three methods in the ATLAS detector: inside-out, outside-in, and TRT-standalone. The inside-out method creates tracks by starting with a seed hit in the pixel detector, then SCT hits are added, finally the track is extrapolated out into the TRT. This method creates tracks of particles that are mostly produced in the hard pp interaction and has a requirement of $p_T > 400$ MeV. On the other-hand the outside-in method starts with track segments in the TRT and extrapolates towards the beamline using silicon that were not used in the inside-out method. Outside-in tracking typically reconstructs secondary vertices from particles that have long enough lifetimes to decay while inside the ID, including b quarks and τ leptons. Lastly, TRT-standalone tracks are made only from seeds within the TRT and are not extrapolated to the silicon subdetectors [25]. The reconstructed tracks are used in the identification of various types of particles.

5.2 Topological Clusters

A topocluster is defined as a cluster of topologically connected calorimeter cell signals. Topological clusters in the ATLAS detector’s calorimeters are vital to the identification of hadronic final states, meaning jets (Section 5.5), isolated hadrons, and hadronically decaying τ leptons (Section 5.6). Topoclusters are also included in the calculation of missing transverse energy discussed in Section 5.7, as they represent the direction and energy of softer particles in a collision event.

A topocluster is created via a growing volume algorithm that operates based on a set of three thresholds. These thresholds are defined using the calorimeter cell significance ξ_{cell} [26].

$$\xi_{cell} = \frac{E_{cell}}{\sigma_{noise,cell}} \quad (5.1)$$

Where E_{cell} is the energy in the calorimeter cell and $\sigma_{noise,cell}$ is the average expected noise of a given calorimeter cell. An in-depth review of how the $\sigma_{noise,cell}$ value is calculated for TileCal is given in A. A topocluster starts with a seed cell that has a significance greater than the seed threshold S . From the seed cell, all three-dimensionally neighboring cells with a significance greater than the growth threshold N are added to the topocluster. This is done repeatedly until there are no more neighboring cells that pass the requirement $|\xi_{cell}| > N$. If a neighboring cell also passes the $|\xi_{cell}| > S$ threshold, then the topocluster corresponding to the neighbor cell is merged into the original topocluster. Finally, a last layer of the topocluster is added from all neighboring cells passing a threshold of $|\xi_{cell}| > P$. In the ATLAS experiment, the threshold values are set at $(S, N, P) = (4, 2, 0)$.

5.3 Muon Identification

Muons are identified using a combination of information from the ID and the MS. Within the ID, muons leave tracks identical to any other charged particle; however, in the MS tracks are identified within the MDTs through a straight-line fit in a single layer and by doing a combinatorial search of CSC hits in the $\eta - \phi$ plane. [27] Muons are identified through five strategies, each using the information from the ID, MS, and calorimeter (in one case).

- Combined (CB): Match ID and MS tracks. Perform a combined track fit on ID and MS hits. Takes into account energy loss in calorimeters

- Inside-Out (IO): Extrapolate ID tracks, look for at least three loosely aligned MS hits.
Calorimeter energy loss is accounted for.
- Muon Spectrometer Extrapolated (ME): Extrapolate MS tracks back to the beamline.
No ID hits are taken into account.
- Segmented-Tagged (ST): Extrapolate ID tracks and match to MS segments with tight angular requirement. Muon parameters are taken directly from the ID.
- Calorimeter-Tagged (CT): Extrapolate ID tracks into the calorimeters. Look for energy deposits consistent with minimum ionizing particles. Tag as muon, take parameters from ID.

All muon identification strategies have a transverse momentum cut on ID tracks of $p_T^{track} > 2$ GeV, except for CT, which has a cut of $p_T^{track} > 5$ GeV.

Reconstructed muons are divided into three WPs to allow analyzers a choice of purity, efficiency, and background rejection.

- Loose: Optimized for reconstruction of $H \rightarrow 4\mu$. Lowest purity and highest efficiency.
- Medium: Efficiency and purity are suitable for a wide range of analyses with small systematic uncertainties.
- Tight: High purity, slightly lower efficiency than medium WP. Significantly higher background rejection.

The analysis discussed in this dissertation uses the Loose WP for muons.

5.4 $e\gamma$ Identification

Electrons and photons deposit the majority of their energy in the EM calorimeters in similar fashion. Electrons produce Bremsstrahlung photons as they interact with the EM calorimeter, the produced photons then convert into an electron-positron pair. This process repeats and produces a shower. A photon that is produced in the ID and travels to the EM calorimeters creates a very similar shower by converting into an electron-positron pair, thus creating a very similar shower. The discerning difference between an electron's signature and that of a photon is matching tracks. An electron carries an EM charge, thus leaving a track in the ID; whereas a photon does not carry an EM charge, therefore does not leave a track. The process of identifying an EM shower as either electron initiated or photon initiated is detailed in [28]. A brief algorithm flow chart of this process can be seen in Figure 5.2. If tracks in the ID are found to match a topocluster in the EM calorimeter, then it is identified as an electron, re-clustered into so called superclusters to ensure the full shower is captured, calibrated, then lastly made into an analysis object for use in physics analyses. The same algorithm is used to identify photons with the exception of matching tracks to the ID. Instead, photons are matched to conversion vertices where the initial photon first converted into an electron-positron pair. Both electrons and photons are reconstructed at three WPs. As with muons, there are three WPs, Loose, Medium, and Tight; the stricter WPs being subsets of the looser WPs.

To ensure that an electron or photon is indeed an initial particle and not part of another shower, whether it be from a converted photon in a hadron decay, electrons from heavy flavor hadrons or a light hadron mis-identified as an electron, an isolation variable is calculated. The isolation variable is based on track isolation and defined as the sum of transverse momenta

of all tracks within a cone around the electron candidate of $\Delta R = 0.2$ or in the case of high energy photons, $10 \text{ GeV}/E_T$. Where E_T is the transverse energy of the electron.

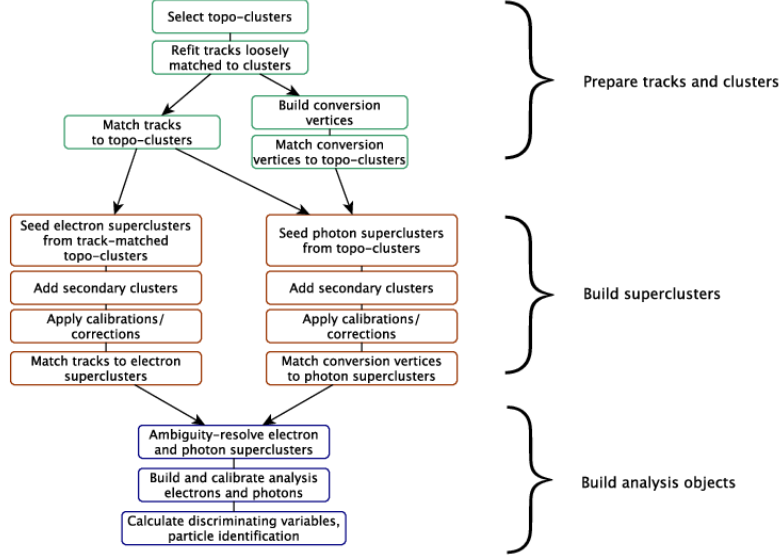


Figure 5.2: Algorithm flow diagram for the electron and photon reconstruction [28].

5.5 Jets

A jet is a reconstructed object of calorimeter energy that is meant to capture the energy of a hadronic shower, typically initiated from hard scatter quarks or hadrons. There are several algorithms available to perform a clustering of calorimeter topoclusters to form jets. This dissertation uses jets created from particle flow objects. The particle flow algorithm is described in detail in [29], a flow chart of the algorithm is shown in Figure 5.3 and an idealized example of the particle flow algorithm performing the reconstruction of hadrons is shown in Figure 5.4.

The particle flow algorithm starts by matching selected tracks to a single topocluster. The expected energy of the initial particle in the calorimeter is calculated from the track

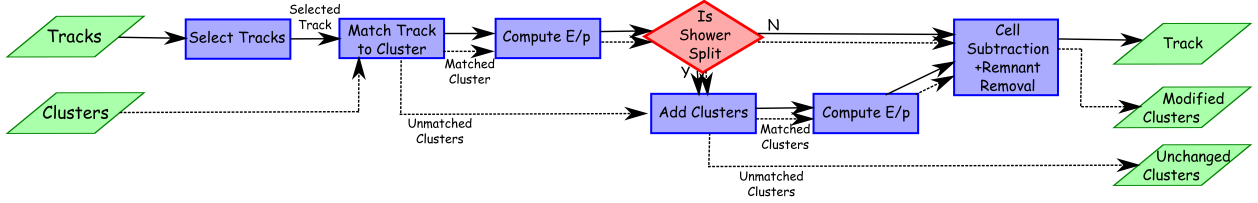


Figure 5.3: A flow chart of how the particle flow algorithm proceeds, starting with track selection and continuing until the energy associated with the selected tracks has been removed from the calorimeter. At the end, charged particles, topoclusters which have not been modified by the algorithm, and remnants of topoclusters which have had part of their energy removed remain [29].

momentum and the topocluster position. The probability of the track-topocluster system being deposited in multiple topoclusters is then calculated. The algorithm then adds in more topoclusters to the output object based on this probability. The expected energy of the initial particle is subtracted from the energy of the matched topoclusters cell by cell. If the energy of the output object is consistent with a single particle signal, then the remaining topocluster remnants are removed. The outputs of the particle flow algorithm are then fed into the anti- k_t algorithm [30] with a radius value of $R = 0.4$.

The anti- k_t algorithm is a jet finding algorithm that is collinear and infrared safe. Meaning the number of identified jets does not change due to splitting or merging of high transverse momentum particles, nor the presence of soft gluon emission between jets [31]. A jet is constructed in the anti- k_t algorithm through an iterative process using a the distance parameter defined as

$$d_{ij} = \min(k_{t,i}^{-2}, k_{t,j}^{-2}) \frac{\Delta_{ij}^2}{R^2} \quad (5.2)$$

where k_t is the transverse momentum, R is an input parameter defining the radius of the jet cone, and Δ_{ij} is the distance between objects i and j defined as

$$\Delta_{ij} = (y_i - y_j)^2 + (\phi_i - \phi_j)^2 \quad (5.3)$$

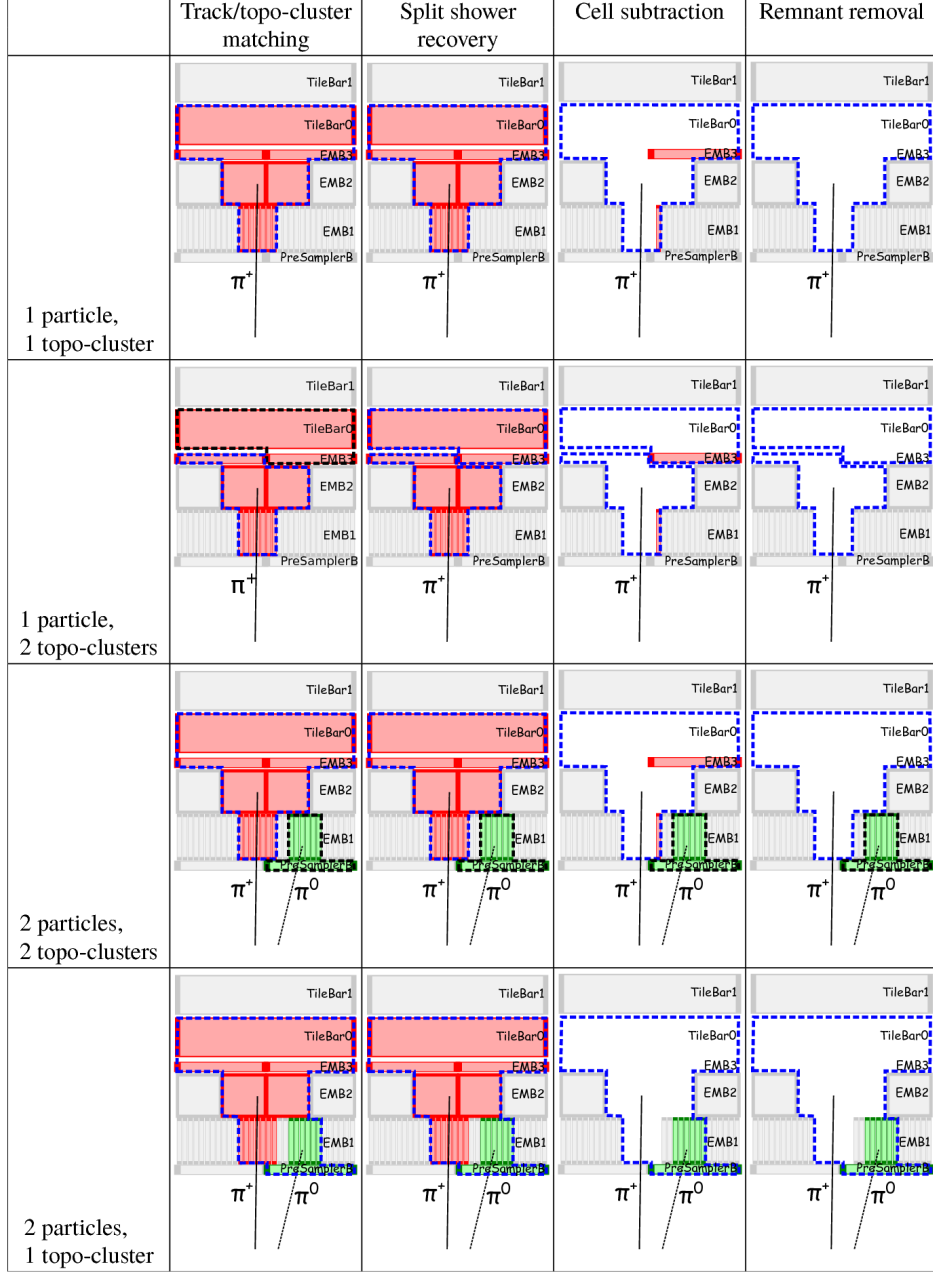


Figure 5.4: Idealized examples of how the algorithm is designed to deal with several different cases. The red cells are those which have energy from the π^+ , the green have cells energy from the photons in the π^0 decay, the dotted lines represent the original topocluster boundaries with those outlined in blue having been matched by the algorithm to the π^+ , while those in black are yet to be selected. The different layers in the EM calorimeter (Presampler, EMB1, EMB2, EMB3) are indicated. In this sketch only the first two layers of the Tile calorimeter are shown (TileBar0 and TileBar1) [29].

The anti-kt algorithm first identifies the smallest d_{ij} and clusters the particle flow objects if $d_{ij} > k_{t,i}^{-2}$. If $d_{ij} > k_{t,i}^{-2}$ then the particle flow object is discarded. This process continues iteratively until there are no more objects to consider. Objects with $\Delta > R$ are still considered, making the R input parameter an energy cut-off for clustering and not a direct radius value. Figure 5.5 shows the anti- k_t algorithm's performance compared to other jet finding algorithms. The anti- k_t algorithm results in a more conical shape than other jet finding algorithms; better encapsulating the shower profile of jets.

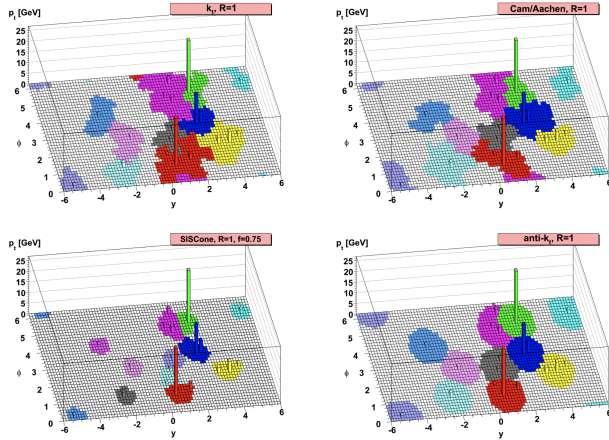


Figure 5.5: Comparison between several jet finding algorithms [30].

5.5.1 b-jet Tagging

Jets originating from hard scatter b quarks are an important signature in high energy physics colliders, especially so in the analysis discussed in this dissertation. An initial state b quark hadronizes into B-hadrons which have a relatively long lifetime. Due to the relativistic speeds and long lifetime of the B-hadrons they travel a distance away from the IP before decaying and creating a hadronic shower. This leads to a secondary vertex that can be

measured. A pictorial representation is shown in Figure 5.6. The impact parameter d_0 shown is the minimum distance between the tracks from the secondary vertex and IP.

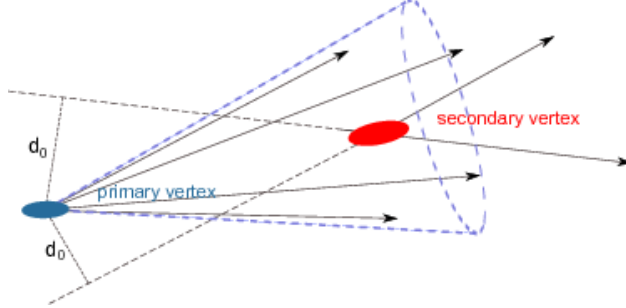


Figure 5.6: Schematic view of the tracks in a b -jet [32].

There are several methods used to tag a jet as coming from a b quark; this analysis uses the DL1 high level tagger [33] that is based on an Artificial Deep Neural Network. Neural networks are discussed in detail in Section ???. DL1 not only tags b -jets, but also output the probability for a jet to be initiated from a charm or light flavor quark. The DL1 tagger has over 20 input variables, including the p_T and η of jets [34]. The analysis discussed in this dissertation uses a fixed cut working point that corresponds to an average efficiency of 70% for b -jets in $t\bar{t}$ events.

5.6 τ Identification

One of the most important particles in the final state of the search discussed in this dissertation is the τ lepton. The decay channels of τ leptons make them difficult to reconstruct. A τ lepton can decay to hadrons, an electron, or a muon; in each decay mode, at least one neutrino is also present. The analysis discussed in this dissertation only considers τ leptons that have decayed hadronically. The hadronic decay mode consists of 1 or 3 charged hadrons (π^\pm), a neutrino, and possible neutral hadrons (π^0). A τ lepton decaying in this manner within the ATLAS detector leaves 1 or 3 tracks in the ID and collimated showers of energy

in the calorimeters; the neutrino does not interact with the ATLAS detector, therefore no direct signature is left behind. Reconstruction is done on the visible part of the hadronically decaying τ lepton, further referred to as $\tau_{had-vis}$ in the rest of this dissertation.

The $\tau_{had-vis}$ candidates start with an anti- k_t jet seed with $E_T > 10$ GeV in the calorimeter, tracks and topoclusters within $\Delta R = 0.2$ are added to the $\tau_{had-vis}$ candidate. The axis of the original jet seed is redefined in the direction of the $\tau_{had-vis}$ candidate and calibration is done at the $\tau_{had-vis}$ scale. An overlap removal is done to ensure the $\tau_{had-vis}$ is isolated from electrons and muons. Tracks are required to have $E_T > 30$ GeV, $|\eta| < 2.3$ and strictly either 1 or 3 tracks. A $\tau_{had-vis}$ candidate is referred to as 1-prong or 3-prong based on the associated number of tracks. To discern $\tau_{had-vis}$ objects from quark and gluon initiated jets a recurrent neural network (RNN) is used. The search described in this analysis uses a medium WP that corresponds to 75% identification efficiency for 1-prong and 60% for 3-prong in $\gamma \rightarrow \tau\tau$ collision events. Only the highest p_T $\tau_{had-vis}$ candidate in an event is considered in this analysis.

5.7 E_T^{miss}

The final SM particle in the reconstruction scheme is the neutrino¹. The presence of a neutrino, or another minimally interacting particle, can be inferred through the calculation of $E_T^{\text{miss}}\text{²};$ which takes advantage of the initial collision having a small momentum in the transverse plane ($p_T \simeq 0$). The initial momentum in the z direction (along the beamline) cannot be known due to the composite nature of the colliding protons and the associated PDFs of their components.

¹The W, Z and gluon do not have long enough lifetimes to leave signatures within the ATLAS detector volume. Instead, their presence is inferred through their decay products

²The choice of E_T^{miss} to represent missing transverse momentum is a common nomenclature. Other choices include p_T^{miss} , MET, and et miss.

The calculation of E_T^{miss} in the ATLAS detector is defined as

$$E_T^{\text{miss}} = -\sum E_T = \sum p_T^\mu + \sum p_T^e + \sum p_T^\gamma + \sum p_T^\tau + \sum p_T^{\text{jets}} + \sum p_T^{\text{soft}} \quad (5.4)$$

where the p_T^{soft} term comes from soft tracks that are not associated with any physics objects [35]. The analysis discussed in this dissertation uses E_T^{miss} triggers in one of the subchannels to select events and is described in chapter 6.

CHAPTER 6

SEARCH FOR CHARGED HIGGS BOSONS

This chapter details a search for a charged Higgs boson decaying to a hadronically decaying tau lepton and a neutrino; the phenomenology is discussed in Section 2.3. This search contains two subchannels, $\tau + \text{jets}$ and $\tau + \ell$ based on the decay of the associated top quark in the collision event. The $\tau + \text{jets}$ subchannel ($t \rightarrow Wb$, $W \rightarrow q\bar{q}$) has a higher branching fraction, leading to higher sensitivity at larger m_{H^\pm} values. The $\tau + \ell$ subchannel ($t \rightarrow Wb$, $W \rightarrow \ell\nu$) has a much lower branching fraction, but takes advantage of single-lepton triggers which enhance background suppression of QCD jet $\rightarrow \tau$ fakes. This leads to an increased sensitivity at lower m_{H^\pm} values. The extra neutrino in the $\tau + \ell$ decay mode creates extra difficulties in separating signal from background in this subchannel by adding a significant contribution to the E_T^{miss} calculation for the event.

The search described by this dissertation uses a profile likelihood ratio as the test statistic in a simultaneous fit in two control regions and three signal regions. The discriminating variable is chosen to be the output score distribution of a multivariate analysis technique (MVA). In the previous publication described in Section 2.3.1 several boosted decision trees (BDT) were used, binned in m_{H^\pm} ; this analysis uses a parameterized neural network (PNN) to classify events as signal-like or background-like.

This chapter discusses in detail the entire analysis, including the signal signatures, event selections, analyzed datasets, modeling of backgrounds, training and evaluation of classifiers, studies of systematic uncertainties, and results.

6.1 Signature and Event Selection

As shown in Figure 2.3, the production of the H^\pm is dependent on the mass m_{H^\pm} . Table 6.1 shows the production mechanisms for m_{H^\pm} values with respect to the top quark mass m_t as well as the main decay mode (and theoretical constraints), as well as the main source of background. Three mass ranges are defined, low mass $80 \leq m_{H^\pm} \leq 130$ GeV, intermediate mass $140 \leq m_{H^\pm} \leq 190$, and high mass $200 \leq m_{H^\pm} \leq 3000$ GeV. The two subchannels have similar signal signatures with a hard scatter source of E_T^{miss} , one $\tau_{\text{had-vis}}$, and at least 1 b -jet from the associated top decay. In the $\tau + \ell$ subchannel there is an extra requirement of a lepton (e or μ). Due to the variable amount of energy available to the final state products based on m_{H^\pm} the event topology changes as a function of m_{H^\pm} . As described in Section ??, classifiers are trained and evaluated in m_{H^\pm} bins to account for the varying event topology.

H^\pm Mass	Production Mechanism	Decay	Main Background
$m_{H^\pm} < m_t$	double-resonant $t \rightarrow H^\pm b$ (LO) 	$H^\pm \rightarrow \tau^\pm \nu_\tau$ (low $\tan \beta \implies H^\pm \rightarrow cs$ or $H^\pm \rightarrow cb$)	$t\bar{t}$, single-top
$m_{H^\pm} \simeq m_t$	non-resonant $t \rightarrow H^\pm b$ (LO) interferences taken into account	$H^\pm \rightarrow \tau\nu$	$t\bar{t}$, single-top
$m_{H^\pm} > m_t$	single-resonant $gg \rightarrow tbH^\pm$ (NLO) 	$H^\pm \rightarrow tb$ ($\cos(\beta - \alpha) \simeq 0$ and large $\tan(\beta) \implies H^\pm \rightarrow \tau\nu$ $BR(H^\pm \rightarrow \tau^\pm \nu_\tau) \simeq 10 - 15\%$)	multi-jet

Table 6.1: H^\pm production mechanisms based on m_{H^\pm} , dominant H^\pm decay mode, and the main background associated with the diagram.

6.1.1 Object Definitions

Table 6.2 shows the identification requirements on all objects used in the analysis. In both subchannels $\tau_{had-vis}$ candidates are required to fit the medium working point described in Section 5.6 that corresponds to a 75% efficiency for 1-prong and 60% efficiency for 3-prong $\tau_{had-vis}$ identification, an $|\eta|$ cut of < 2.3 that also excludes the gap and crack region of the ATLAS calorimeters at $1.37 < |\eta| < 1.52$, an overlap removal with electrons is also performed. For the $\tau+jets$ subchannel, the $\tau_{had-vis} p_T$ is required to be greater than 40 GeV and greater than 30 GeV for the $\tau + \ell$ subchannel. Although muons and electrons are not part of the $\tau+jets$ signal final state, a loose identification and isolation requirement is used to veto events; while the $\tau + \ell$ subchannel requires there to be either an electron or a muon that passes the tight identification and isolation requirements as well as a p_T above 30 GeV. The jets in candidate events are required to have greater than 25 GeV in p_T and are made with the anti- k_t algorithm with R=0.4. Jets tagged as b -jets are done so at a 70% efficient working point using the DL1r tagger described in Section 5.5.1.

Object	$\tau+jets$	$\tau + \ell$
$\tau_{had-vis}$	Leading reconstructed τ (regardless of its ID), mediumID*, $p_T > 40$ GeV, $ \eta ^{***} < 2.3$, e OLR	Leading reconstructed τ (regardless of its ID), mediumID*, $p_T > 30$ GeV, $ \eta ^{***} < 2.3$, e OLR
e	LoseLLH, $p_T > 20$ GeV, $ \eta ^{***} < 2.47$, Loose isolation, IP cuts	TightLLH, $p_T > 30$ GeV, $ \eta ^{***} < 2.47$, Tight isolation, IP cuts
μ	LooseID, $p_T > 20$ GeV, $ \eta < 2.5$, Loose isolation, IP cuts	TightID, $p_T > 30$ GeV, $ \eta < 2.5$, Tight isolation, IP cuts
jet	AntiKt4EMPFlow, $p_T > 25$, GeV $ \eta < 2.5$, JVT** > 0.59, Btag=70%, DL1r	AntiKt4EMPFlow, $p_T > 25$ GeV, $ \eta < 2.5$, JVT** > 0.59 , Btag=70%, DL1r

Table 6.2: Definitions of physics objects used in this analysis.

6.1.2 Event Selections

Each subchannel signal region has stricter requirements than those described in Section 6.2. Table 6.3 details these selections. The channels differ in the triggers used; the $\tau + \text{jets}$ subchannel relies on E_T^{miss} triggers while the $\tau + \ell$ subchannel relies on single lepton triggers. Due to the difficulty of separating signal from background the $\tau + \text{jets}$ subchannel has a higher p_T cut on the $\tau_{\text{had-vis}}$ of 40 GeV as opposed to the $\tau + \ell$ value of 30 GeV. In addition, a higher value of E_T^{miss} of 150 GeV is required for the $\tau + \text{jets}$ subchannel. A value of 50 GeV is also required of the transverse mass m_T defined as

$$m_T = \sqrt{2p_T^\tau E_T^{\text{miss}}(1 - \cos\Delta\phi_{\tau, E_T^{\text{miss}}})} \quad (6.1)$$

The $\tau + \ell$ has no such requirement, but does require the $\tau_{\text{had-vis}}$ and lepton to have opposite electromagnetic charge. A set of orthogonal control regions are defined for each subchannel to verify proper background modelling and are described in Section 6.3. The acceptance of signal in the signal regions defined in 6.3 is shown in Figure 6.1.

$\tau + \text{jets SR}$	$\tau + \ell \text{ SR}$
E_T^{miss} Trigger (mostly HLT_xe110)	Single lepton trigger (e or μ)
1 $\tau_{\text{had-vis}}$; $p_T^\tau > 40$ GeV	1 $\tau_{\text{had-vis}}$; $p_T^\tau > 30$ GeV
0 ℓ (e or μ) ; $p_T^\ell > 20$ GeV	1 ℓ (e or μ) ; $p_T^\ell > 30$ GeV
≥ 3 jets ; $p_T^j > 25$ GeV	≥ 1 jet ; $p_T^j > 25$ GeV
≥ 1 b-jets; $p_T^{b\text{-jet}} > 25$ GeV	≥ 1 b-jets; $p_T^{b\text{-jet}} > 25$ GeV
$E_T^{\text{miss}} > 150$ GeV	$E_T^{\text{miss}} > 50$ GeV
$m_T(\tau, E_T^{\text{miss}}) > 50$ GeV	Opposite sign τ and ℓ

Table 6.3: $\tau + \text{jets}$ and $\tau + \ell$ signal region definitions.

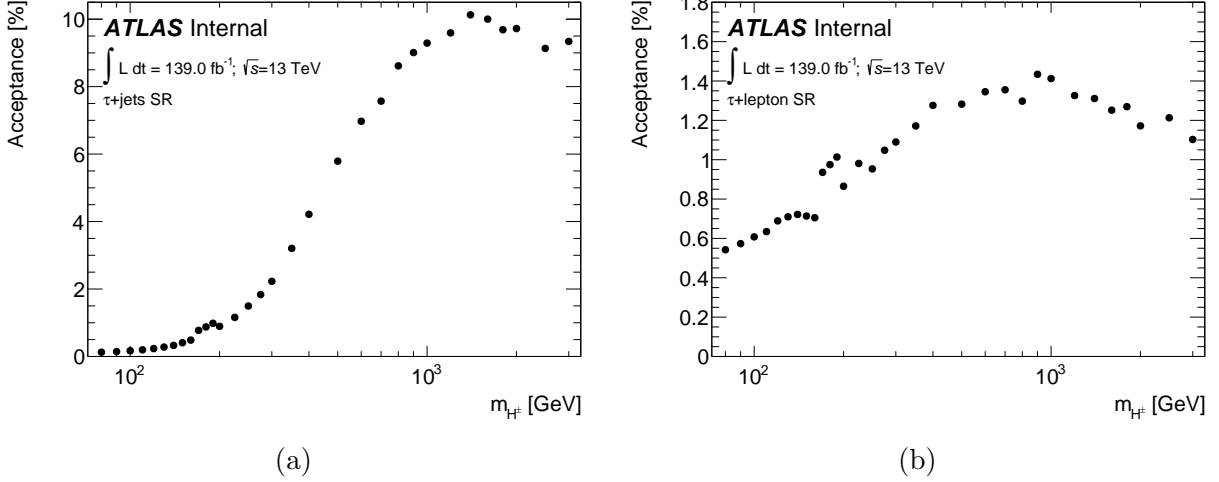


Figure 6.1: Signal acceptance as a function of the charged Higgs boson mass for both the $\tau + \text{jets}$ (a) and $\tau + \ell$ subchannels (b).

6.2 Datasets

This analysis uses the full Run-2 ATLAS dataset collected between 2015 and 2018 corresponding to $139.0 \pm 2.4 \text{ fb}^{-1}$ [36]. The datasets used are required to be included in the ATLAS ‘‘Good Run Lists’’ (GRLs), meaning they have passed nominal data quality checks with all detector subsystems operating within normal conditions. Further event cleaning is applied that removes events in which a reconstructed jet originated from detector noise or non-collision backgrounds. The collection of data throughout Run-2 can be seen in Figure 3.4.

6.2.1 Signal Modeling

Monte Carlo (MC) simulations of H^\pm signal events are generated at varying orders dependent on m_{H^\pm} . In all cases, the 2HDM Type II model described in Section 2.2.2 is

assumed and the generator MadGraph is used. The lower mass range corresponding to $m_{H^\pm} < 140$ GeV where a H^\pm takes the place of a W^\pm in a top decay is generated at LO. The intermediate mass range of $140 \leq m_{H^\pm} < 200$ GeV is generated at LO, taking into account the non-resonant, single-top resonant and double-resonant diagrams and their interferences. In this mass range, the final state contains one H^\pm , one W^\pm , and two b quark. For charged Higgs masses of 200 GeV and above, the H^\pm is produced in association with a top quark and is generated at NLO. In all cases, the parton generator is interfaced with Pythia 8 using the A14 underlying event tuning parameters [37]. Table 6.4 shows the cross section and raw number of events generated for each m_{H^\pm} point for both subchannels.

m_{H^\pm} [GeV]	σ [pb]	$\tau + \ell$ Generated Events	$\tau + \text{jets}$ Generated Events
80	61.639	220k	110k
90	52.823	220k	110k
100	43.777	220k	110k
110	34.770	220k	110k
120	26.092	220k	110k
130	18.069	220k	110k
140	15.023	220k	220k
150	7.681	220k	220k
160	2.665	220k	220k
170	0.63748	220k	220k
180	0.52979	220k	220k
190	0.47201	220k	220k
200	0.55632	110k	220k
225	0.44081	110k	220k
250	0.3573	110k	220k
275	0.28592	110k	220k
300	0.23373	110k	220k
350	0.15774	110k	220k
400	0.10818	110k	220k
500	0.054139	110k	220k
600	0.02847	110k	220k
700	0.015764	110k	220k
800	0.009067	110k	220k
900	0.005324	110k	220k
1000	0.003271	110k	220k
1200	0.001311	110k	220k
1400	0.000558	110k	220k
1600	0.000252	110k	220k
1800	0.000120	110k	220k
2000	0.0000587	110k	220k
2500	0.0000111	110k	220k
3000	0.00000234	110k	220k

Table 6.4: For each H^\pm mass the generator cross-section ($\sigma \times BR(H^\pm \rightarrow \tau^\pm \nu_\tau)$) is given, as well as the number of generated events for both $\tau + \ell$ and $\tau + \text{jets}$ subchannels.

6.3 Background Modeling

The main sources of backgrounds are shown in Table 6.5, separated between backgrounds with a prompt $\tau_{had-vis}$ in the hard scatter process and those that arise from the misidentification of other physics objects as a $\tau_{had-vis}$. The cross section of all simulated background samples and the relevant generators can be seen in Table 6.6. Control regions that are designed to be orthogonal to the signal region are created for both subchannels in order to study the modeling of the backgrounds. These control regions are defined by the cuts in Table 6.7 ($\tau+jets$) and Table 6.8 ($\tau+\ell$). For the $\tau+\ell$ subchannel the Same Sign and b-veto control regions are further split into two control regions, one that requires a μ in the event and another that requires an electron.

Backgrounds w/ prompt $\tau_{had-vis}$	Backgrounds w/ fake τ
$t\bar{t}$ estimated with MC	Fake $j \rightarrow \tau$ estimated with data driven fake factor method
$W(Z) + jets$ estimated with MC	Fake $\ell \rightarrow \tau$ estimated with MC, validated on $Z \rightarrow ee$
Diboson estimated with MC	

Table 6.5: Dominant backgrounds from prompt $\tau_{had-vis}$ and fake $\tau_{had-vis}$ candidates.

As seen in Table 6.5 misidentified objects appearing as $\tau_{had-vis}$ candidates comprise a significant portion of the total background. Fakes arising from $\ell \rightarrow \tau$ misidentification are well modeled in MC simulations and are reweighted with scale factors provided by the ATLAS τ combined performance group. The mass of the $\tau_{had-vis}$ electron system can be seen in Figure 6.2 as verification of fake $\ell \rightarrow \tau$ modeling. However, fakes due to $j \rightarrow \tau$ misidentification are not well modeled in MC simulations due to a poor understanding of systematic uncertainties associated with the fake $\tau_{had-vis}$ object and limited statistics of simulated events. Instead, a data driven method is used to extract a scaling constant referred to as a fake factor.

Background process	Generator & parton shower	Cross section number(s) [pb]
$t\bar{t}$ with at least one lepton ℓ	Powheg & Pythia8	729.77*
Single top-quark t -channel		59.17*
Single top-quark s -channel	Powheg & Pythia8	3.29*
Single top-quark Wt -channel		83.83
$W(\ell\nu) + \text{jets}$	Sherpa 2.2.1	2.0×10^4 2.0×10^4 2.0×10^4
$Z/\gamma^*(\ell\ell, \nu\nu) + \text{jets}$	Sherpa 2.2.1	2.1×10^3 2.1×10^3 2.1×10^3
WW		54.81
WZ	Powheg & Pythia8	16.34
ZZ		8.94

Table 6.6: Cross sections for the main SM background samples at $\sqrt{s} = 13$ TeV. Here, ℓ refers to the three lepton families e , μ and τ . All background cross sections are normalized to NNLO predictions, except for diboson events, where the NLO prediction is used. A '*' indicates that the quoted cross section for the sample is neglecting leptonic/hadronic branching ratios.

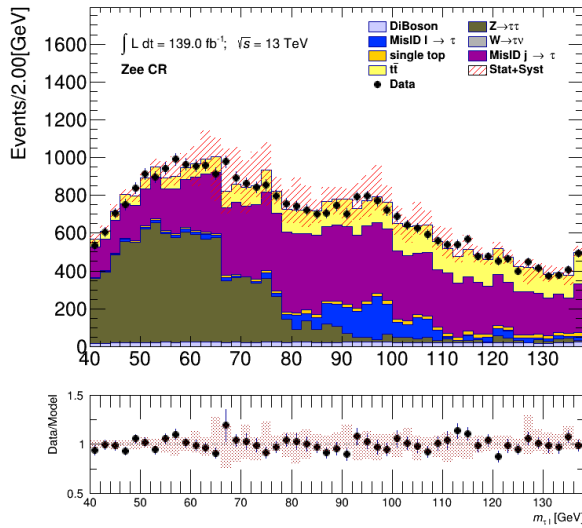


Figure 6.2: Mass of τ - e system in the Zee control region.

$t\bar{t}$ Control Region	b-veto Control Region
<p>$1 \tau_{had-vis}$</p> <p>$p_T^\tau > 40 \text{ GeV}$</p> <p>$\geq 3 \text{ jets}$</p> <p>$\geq 2 \text{ b-jets}$</p> <p>$E_T^{\text{miss}} > 150 \text{ GeV}$</p> <p>$m_T(\tau, E_T^{\text{miss}}) < 100 \text{ GeV}$</p>	<p>$1 \tau_{had-vis}$</p> <p>$p_T^\tau > 40 \text{ GeV}$</p> <p>$\geq 3 \text{ jets}$</p> <p>$p_T^{jet} > 25 \text{ GeV}$</p> <p>$E_T^{\text{miss}} > 150 \text{ GeV}$</p> <p>$m_T(\tau, E_T^{\text{miss}}) > 50 \text{ GeV}$</p> <p>b veto</p> <p>$\ell$ veto</p>
(a) $t\bar{t}$ modeling	(b) Close to signal region
W+Jets Control Region	b-veto $m_T \geq 100$ Control Region
<p>$1 \tau_{had-vis}$</p> <p>$p_T^\tau > 40 \text{ GeV}$</p> <p>$\geq 3 \text{ jets}$</p> <p>$p_T^{jet} > 25 \text{ GeV}$</p> <p>$E_T^{\text{miss}} > 150 \text{ GeV}$</p> <p>$m_T(\tau, E_T^{\text{miss}}) > 100 \text{ GeV}$</p> <p>b veto</p> <p>$\ell$ veto</p>	<p>$1 \tau_{had-vis}$</p> <p>$p_T^\tau > 40 \text{ GeV}$</p> <p>$\geq 3 \text{ jets}$</p> <p>$p_T^{jet} > 25 \text{ GeV}$</p> <p>$E_T^{\text{miss}} > 150 \text{ GeV}$</p> <p>$m_T(\tau, E_T^{\text{miss}}) > 100 \text{ GeV}$</p> <p>b veto</p> <p>$\ell$ veto</p>
(c) W+Jets modeling	(d) Fake $j \rightarrow \tau$ enriched region

Table 6.7: Control region definitions for the $\tau+\text{jets}$ subchannel.

Dilepton-btag CR	b-veto CR
τ veto $n \geq 1$ jets $p_T^{jet} > 25 GeV$ $\geq 1 b\text{-jets}$ $E_T^{\text{miss}} > 50 GeV$ $1 e$ 1μ	$1 \tau_{had-vis}$ $p_T^\tau > 30 GeV$ $1 e(\mu)$ Veto $\mu (e)$ Opposite sign $\tau e (\mu)$ ≥ 1 jets $p_T^{jet} > 25 GeV$ $E_T^{\text{miss}} > 50 GeV$ $1 \text{ tight } e (\mu)$
(a) $t\bar{t}$ and single top modeling	(b) Close to signal region
Zee CR	Same Sign CR
$1 \tau_{had-vis}$ $p_T^\tau > 30 GeV$ veto μ Opposite sign τe ≥ 1 jets $p_T^{jet} > 25 GeV$ b-jet veto $E_T^{\text{miss}} > 50 GeV$ $1 e$ $40 < \text{mass}(\tau, e) < 140 GeV$	$1 \tau_{had-vis}$ $p_T^\tau > 30 GeV$ Same sign $\tau e(\mu)$ Veto $\mu (e)$ ≥ 1 jets $p_T^{jet} > 25 GeV$ $E_T^{\text{miss}} > 50 GeV$ $1 \text{ tight } e (\mu)$
(c) Fake $\ell \rightarrow \tau$ enriched region	(d) Fake $j \rightarrow \tau$ enriched region

Table 6.8: Control region definitions for the $\tau + \ell$ subchannel.

In the $\tau + \ell$ final state a significant portion of $j \rightarrow \tau$ fakes come from misidentifying $\tau_{had-vis}$ candidates in W+Jets events that contain a true ℓ in the W decay and have a misidentified jet as a $\tau_{had-vis}$. Fakes of this manner also arise from QCD-like multi-jet interactions. The fake factor method used to estimate the amount of expected fake $\tau_{had-vis}$ objects that pass the $\tau_{had-vis}$ identification procedure described in Section 5.6. This method applies weights, or fake factors, to a subset of "anti- $\tau_{had-vis}$ " objects that have failed the selection and identification criteria in the signal region. A control region is defined to be rich in anti- $\tau_{had-vis}$ objects, where the $\tau_{had-vis}$ candidates fail the loose τ working point but have a τ identification RNN score of greater than 0.01. The fake factor and number of events with misidentified $\tau_{had-vis}$ objects (N_τ) are defined as:

$$FF = \frac{N^{\tau-id}}{N^{anti-\tau-id}} \quad (6.2)$$

$$N_{fakes}^\tau = N_{fakes}^{anti-\tau} \times FF$$

Both of these values are then corrected for $\tau_{had-vis}$ candidates matching a true hadronic τ at generator level:

$$N^{\tau-id} = N^{\tau-id}(Data) - N^{\tau-id}(MC) \quad (6.3)$$

$$N_{fakes}^{anti-\tau} = N^{anti-\tau}(Data) - N^{anti-\tau}_{true}(MC)$$

Two control regions are created, one to capture the multi-jet (MJ) fakes and the other to study the W+jets fakes. The MJ control region uses the $\tau+jets$ signal region definition with an additional b-veto and an $E_T^{\text{miss}} < 80$ GeV cut. The W+jets control region uses the $\tau + \ell$ signal region definition with a b-veto, no E_T^{miss} cut, and a cut on the transverse mass of the $\ell-E_T^{\text{miss}}$ system of $60 < m_T(\ell, E_T^{\text{miss}}) < 160$ GeV. The FF in the signal region is defined as

$$FF_{sig} = \alpha_{MJ} \times FF_{MJ} + (1 - \alpha_{MJ}) \times FF_{W+jets} \quad (6.4)$$

where α is taken from a template fit of the τ -ID score distributions of the anti- τ s using template shapes from the anti- τ distributions in the MJ and W+jets control regions. In the signal regions, the number of events containing fake- $\tau_{had-vis}$ candidates is defined as

$$N_{fake-\tau} = FF_{sig} \times N_{anti-\tau} \quad (6.5)$$

Figure 6.3 shows FF plotted in each control region for 1-prong and 3-prong $\tau_{had-vis}$ binned in $p_T\tau$; extracted α values and their fits can be seen in Appendix B.

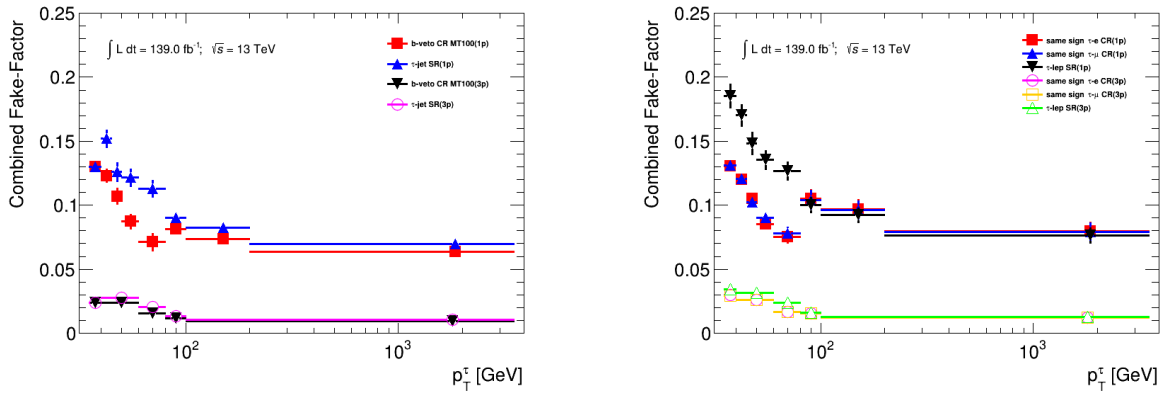


Figure 6.3: Combined fake factors for the τ +jets b-veto $m_T > 100$ control region, τ +jets signal region, τ +electron(muon) with same-sign control region and the $\tau + \ell$ signal region. Error bars represent systematic uncertainties of the method.

To verify background modeling, the E_T^{miss} distributions in each of the control regions are plotted with final scale factors including fake factors in Figure 6.4 (τ +jets) and Figure 6.5 ($\tau + \ell$). These plots include a ratio of reconstructed data events and simulated MC events bin by bin to ensure proper modeling across variable shapes. More background modeling plots can be seen in Appendix C.

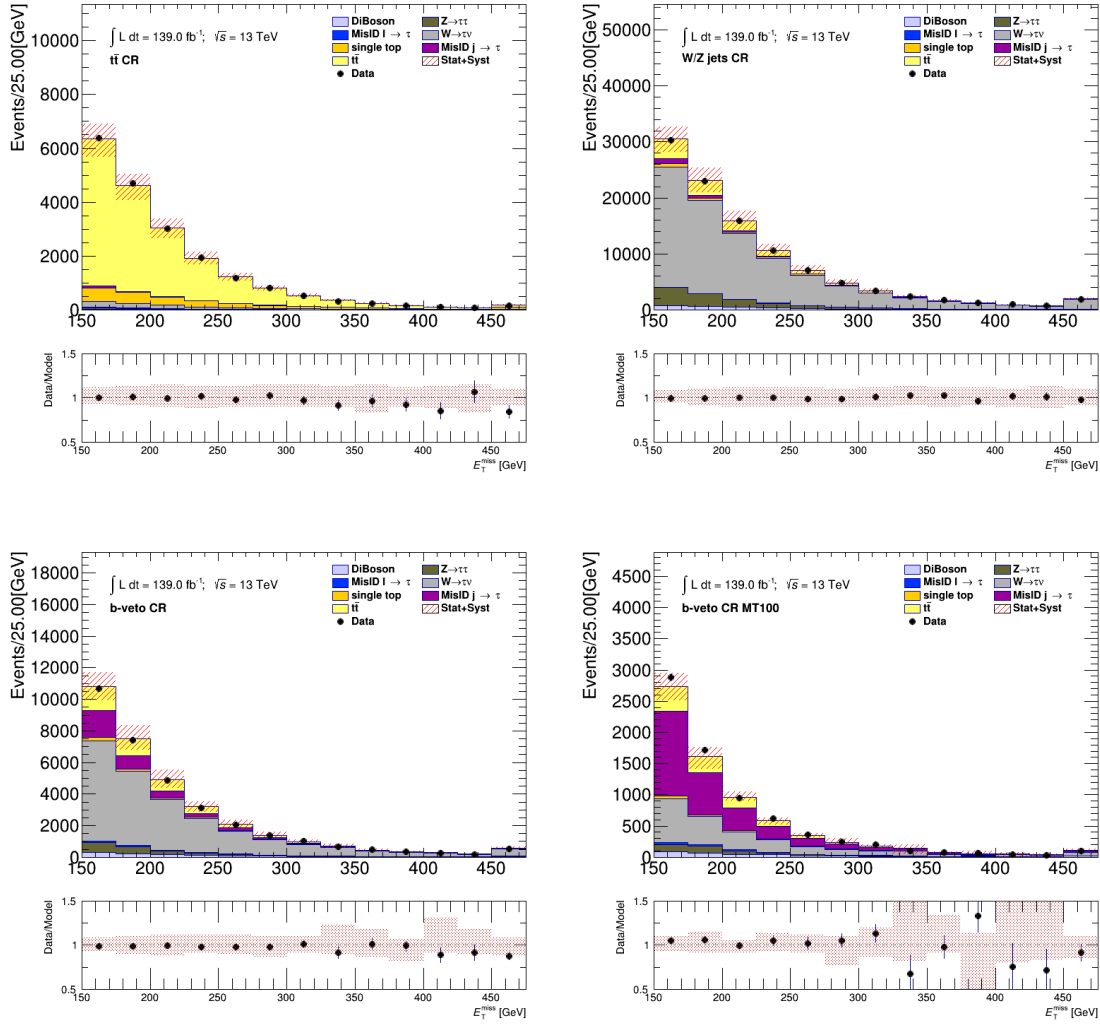


Figure 6.4: Comparison between the predicted and the measured E_T^{miss} distributions in various control regions defined for the $\tau + \text{jets}$ channel. The uncertainty band includes both statistical and systematic uncertainties on the background prediction.

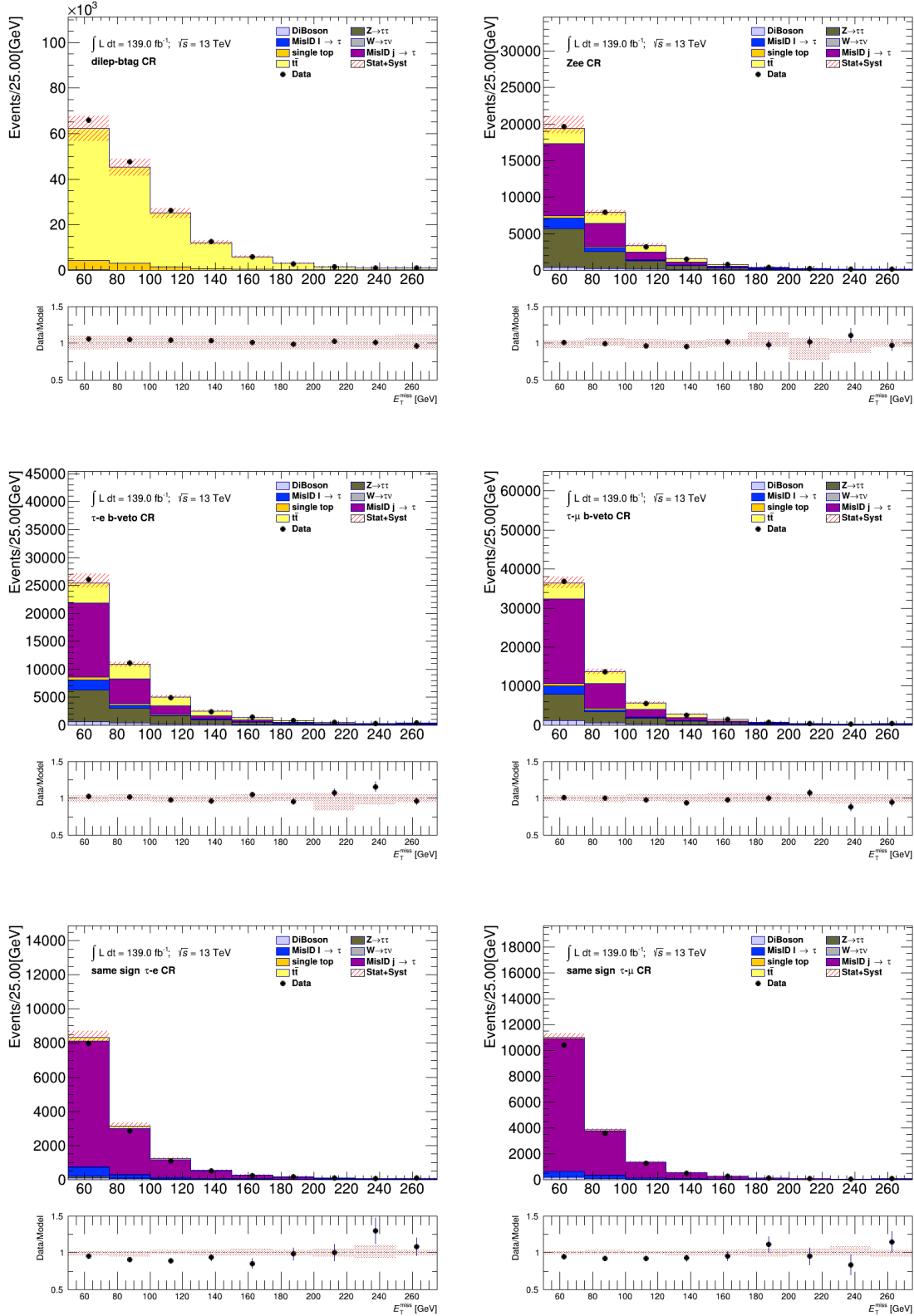


Figure 6.5: Comparison between the predicted and the measured E_T^{miss} distributions in various control regions defined for the $\tau + \ell$ channel. The uncertainty band includes both statistical and systematic uncertainties on the background prediction.

6.4 Multivariate Analysis Techniques

Once variables distributions are properly scaled and data/MC agreement is verified, multivariate analysis techniques are employed to separate signal-like events from background-like events in the signal regions. In the previous publication (described in Section 2.3.1), BDTs binned in m_{H^\pm} were used as the classifier, this publication use one PNN for the entire m_{H^\pm} spectrum. BDTs excel at separating linear correlations, whereas neural networks take advantage of nonlinear correlations. In the case of a PNN the parameterized variable, here m_{H^\pm} , is taken as an input to the network in addition with other input variables. PNNs offer the advantage of having one classifier model that can evaluate at any m_{H^\pm} value by learning how the signal event topology changes as m_{H^\pm} varies [38].

A neural network (NN) is a computing system loosely inspired by the human brain. A NN contains layers of nodes connected to each other with an associated weight and threshold. As long as a node has output greater than the given threshold value, data will flow through that node. Otherwise, that node is not activated and data are not sent to the next layer. The NN as a whole relies on a process called training where the node weights are varied, an accuracy is calculated based on a given loss function, the weights are then varied again and the process repeats. This is done until a preferred accuracy is reached; the final node weights are saved and new data can be evaluated. A diagram of a PNN can be seen in Figure 6.6, where the parameterized input is labeled as θ .

This analysis uses four such PNNs, events with 1-prong τ and 3-prong τ are divided into separate datasets within both subchannels.

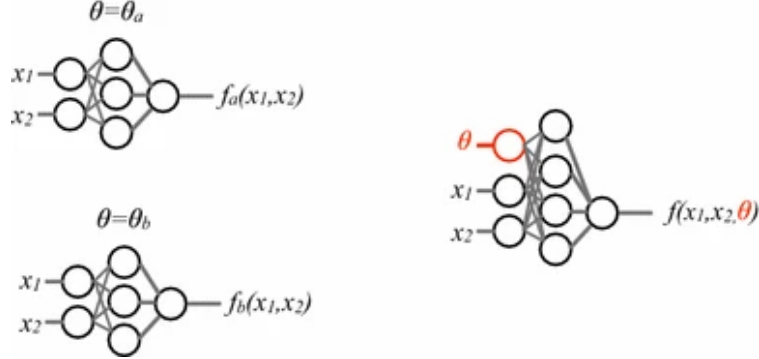


Figure 6.6: *Left*, individual networks with input variables (x_1, x_2) , each trained with examples with a single value of some parameter $\theta = \theta_a, \theta_b$. The individual networks are purely functions of the input variables. Performance for intermediate values of θ is not optimal nor does it necessarily vary smoothly between the networks. *Right*, a single network trained with input variables (x_1, x_2) as well as input parameter θ ; such a network is trained with examples at several values of the parameter θ [38].

6.4.1 Training

The training of the PNNs used in this dissertation are done with the Keras [39] library using the TensorFlow [40] library as backend. In order to increase the significance of training statistics and protect from overtraining, the k -fold method is used. Overtraining occurs when a NN has been fine tuned to have a high accuracy with a specific dataset and does not generalize to other datasets. The k -fold method divides input training samples into k equally populated subsets. The k -th subset is trained on the other $k - 1$ subsets and evaluated on the k -th subset. Figure 6.7 shows a pictorial representation of the k -fold method. $k = 5$ is chosen in this analysis.

A single PNN training is performed on all m_{H^\pm} values at once, with the m_{H^\pm} value being taken as an input variable. For signal events, the m_{H^\pm} value from the MC generator is given; background events are replicated 32 times (the number of simulated m_{H^\pm} points is 32) and each m_{H^\pm} value is given for each set. To avoid biasing the training due to varying statistics

	Fold 1	Fold 2	Fold 3	Fold 4	Fold 5	Background
Partition 1	Evaluation	Train	Train	Train	Train	Fold 1
Partition 2	Train	Evaluation	Train	Train	Train	Fold 2
Partition 3	Train	Train	Evaluation	Train	Train	Fold 3
Partition 4	Train	Train	Train	Evaluation	Train	Fold 4
Partition 5	Train	Train	Train	Train	Evaluation	Fold 5

Figure 6.7: The k-fold method for $k = 5$ [41].

at each m_{H^\pm} value, the background events are weighted by a factor of $w = N_S^i/N_B^i$ where i corresponds to a given m_{H^\pm} value, N_S^i , and N_B^i are the number of signal and background events respectively. When the PNN is evaluated, the m_{H^\pm} value is chosen and the output is used as the discriminant at that m_{H^\pm} .

6.4.2 Input Variables Selection

The choice of input variables to the PNNs is critical to the performance of the analysis. Several sets of variables were compared using expected limits as the figure of merit. All studies were performed in the $\tau + \ell$ signal region, as this region proves the most difficult challenge to separate signal-like events from background-like events. So called low level variables, consisting of the four vector components of the main physics objects in each event, were compared against high level variables; high level meaning they are calculated quantities from the low level variables. Tables of the low level and high level variables are shown in Table 6.9.

The variable $m_{H^\pm}^{Truth}$ corresponds to the m_{H^\pm} value the training and evaluation is performed at. In both cases, the variable Υ is used. Υ is a measure of the $\tau_{had-vis}$ polarization, computed

by taking the asymmetry of energies carried by the charged and neutron pions from the 1-prong τ decay measured in the laboratory frame. Υ is defined as

$$\Upsilon = \frac{E_T^{\pi^\pm} - E_T^{\pi^0}}{E_T^\tau} \approx 2 \frac{p_T^{\tau-\text{track}}}{p_T^\tau} - 1 \quad (6.6)$$

where $p_T^{\tau-\text{track}}$ is the transverse momentum of the track associated with the 1-prong $\tau_{had-vis}$ candidate. As such, Υ is only defined for 1-prong $\tau_{had-vis}$ candidates.

Low Level Input Variables

p_T^τ	η^τ	ϕ^τ	E^τ
p_T^ℓ	η^ℓ	ϕ^ℓ	E^ℓ
p_T^{b-jet}	η^{b-jet}	ϕ^{b-jet}	E^{b-jet}
p_T^{jet}	η^{jet}	ϕ^{jet}	E^{jet}
E_T^{miss}	$\phi^{E_T^{\text{miss}}}$	$p_T^{j_1}$	Υ
$m_{H^\pm}^{\text{Truth}}$			

(a) Low level variables

High Level Input Variables

E_T^{miss}
p_T^τ
p_T^{b-jet}
p_T^ℓ
p_T^{τ}
$\Delta\phi_{\tau, \text{miss}}$
$\Delta\phi_{b-jet, \text{miss}}$
$\Delta\phi_{\ell, \text{miss}}$
$\Delta R_{\tau, \ell}$
$\Delta R_{b-jet, \ell}$
$\Delta R_{b-jet, \tau}$
$\Delta\phi_{\tau, \text{miss}}/\Delta\phi_{\text{jet,miss}}$
Υ
$m_{H^\pm}^{\text{Truth}}$

(b) High level variables

Table 6.9: List of low level (a) and high level (b) kinematic variables used as input to the PNN in the $\tau + \ell$ subchannel. $\Delta\phi_{X, \text{miss}}$ denotes the difference in azimuthal angle between a reconstructed object X ($X = \tau, b-jet, \ell$) and the direction of the missing transverse momentum.

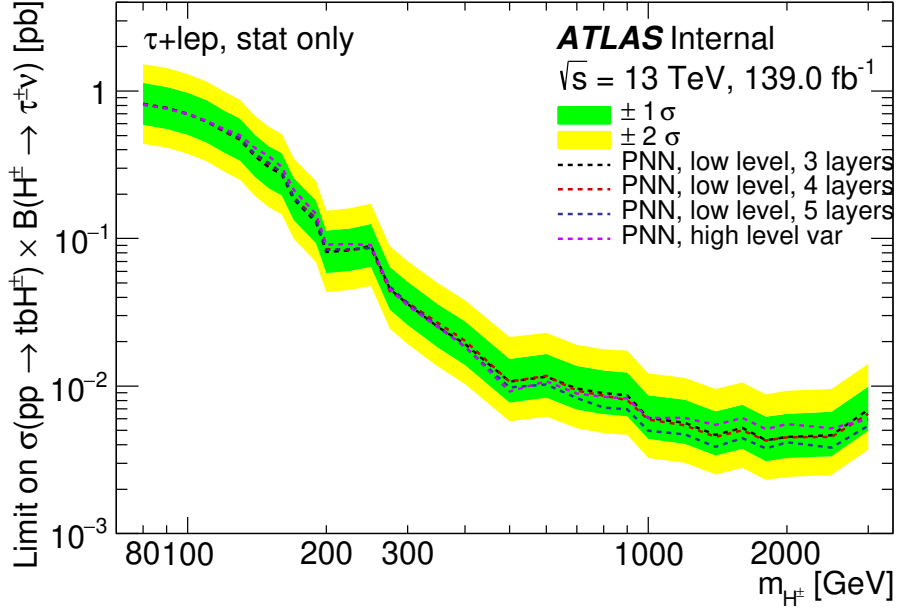


Figure 6.8: Expected limits comparing a set of high level variables and low level variables with various depths in the PNN architecture. X layers refers to the number of layers in the PNN.

An estimate of the impact of low level vs high level variables on the expected limits on the $H^\pm \rightarrow \tau^\pm \nu_\tau$ is shown in 6.8. The set of low level variables was chosen as performance was similar in low m_{H^\pm} and greater in high m_{H^\pm} . A optimization of the number of layers in the PNN and several other parameters of the PNN is discussed in detail in Section 6.4.3.

6.4.3 Hyperparameter Optimization

6.5 Systematic Uncertainties

6.6 Results

CHAPTER 7

CONCLUSION

Appendices

APPENDIX A

TILECAL DATA QUALITY

APPENDIX B

FAKE FACTORS

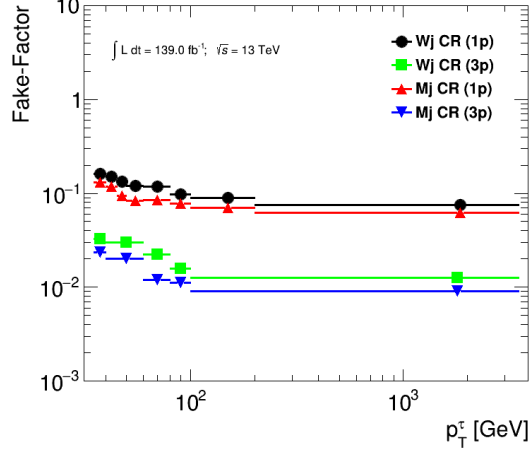


Figure B.1: Fake factors parameterized as a function of p_T^τ and the number of charged τ decay products (1-prong and 3-prong) obtained in the multi-jet and W+jets CRs. The errors shown represent the statistical uncertainty.

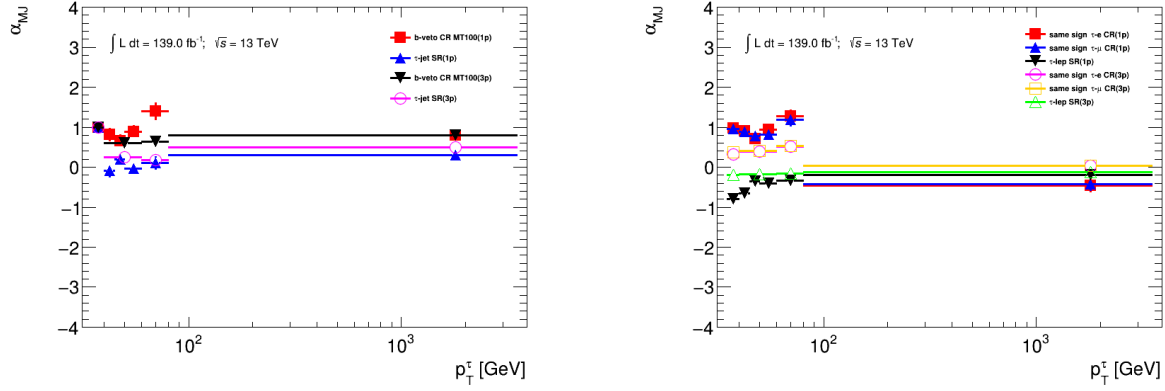


Figure B.2: Corrected α_{MJ} values for the $\tau_{had-vis} + \text{jets}$ b-veto $m_T > 100$ control region, $\tau_{had-vis} + \text{jets}$ signal region, $\tau_{had-vis} + \text{electron(muon)}$ with same-sign control region and the $\tau_{had-vis} + \text{lepton}$ signal region. Error bars represent uncertainties due to α_{MJ} fitting using template-fit method.

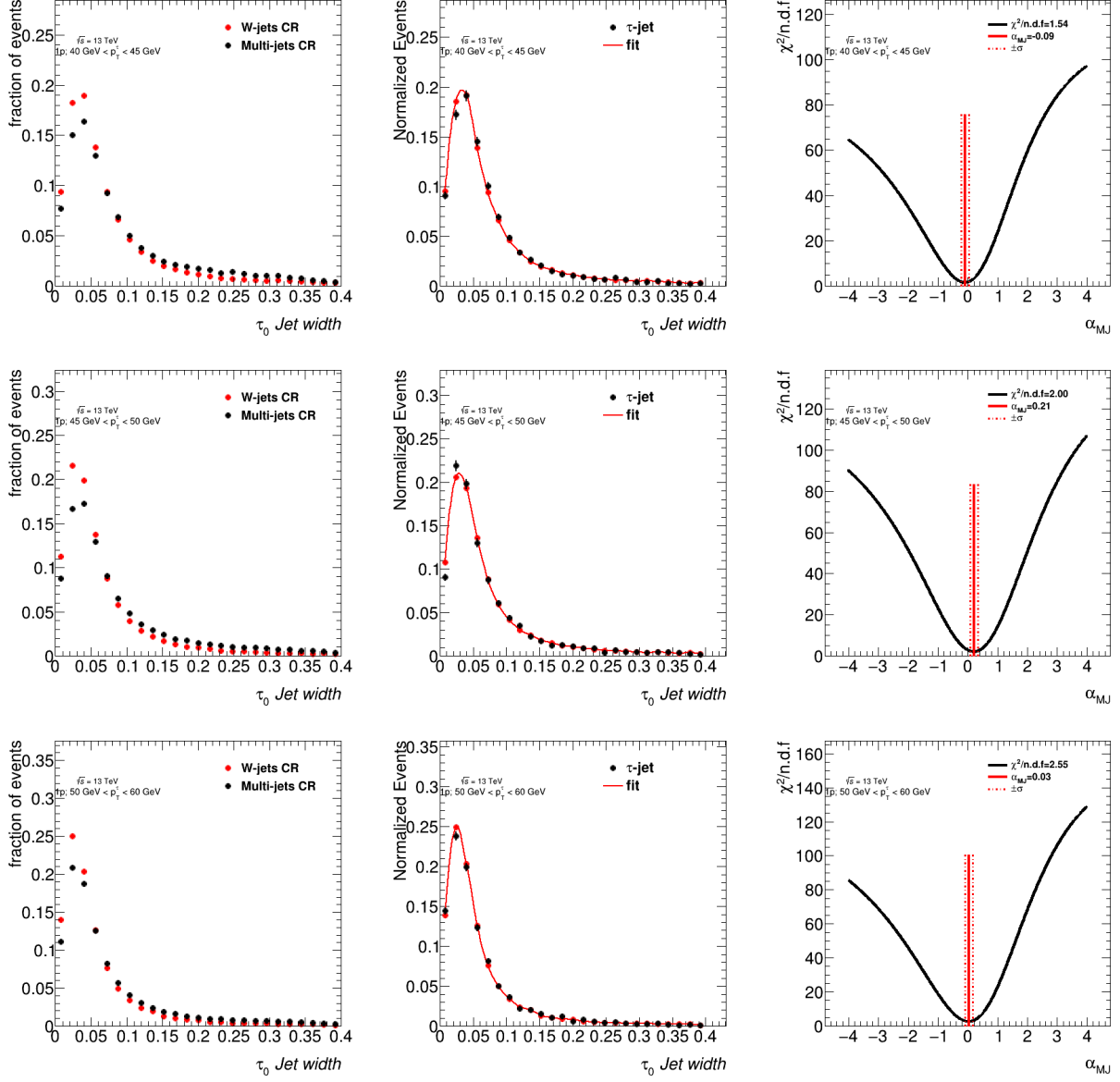


Figure B.3: Estimation of α_{MJ} in the $\tau_{\text{had-vis}} + \text{jets}$ signal region for $p_T \leq 60 \text{ GeV}$ 1-prong $\tau_{\text{had-vis}}$ candidates. Left: templates of discriminating variables for different $\tau_{\text{had-vis}}$ p_T and n-prong slices. Middle: shape of the discriminating variable obtained in the signal region and fitted shape using the templates measured in the control regions. Right: χ^2/ndf of the fit as a function of α_{MJ} , the error on α_{MJ} is defined by the band at $\chi^2_{\min}/\text{ndf} + \sqrt{\frac{2}{\text{ndf}}}$.

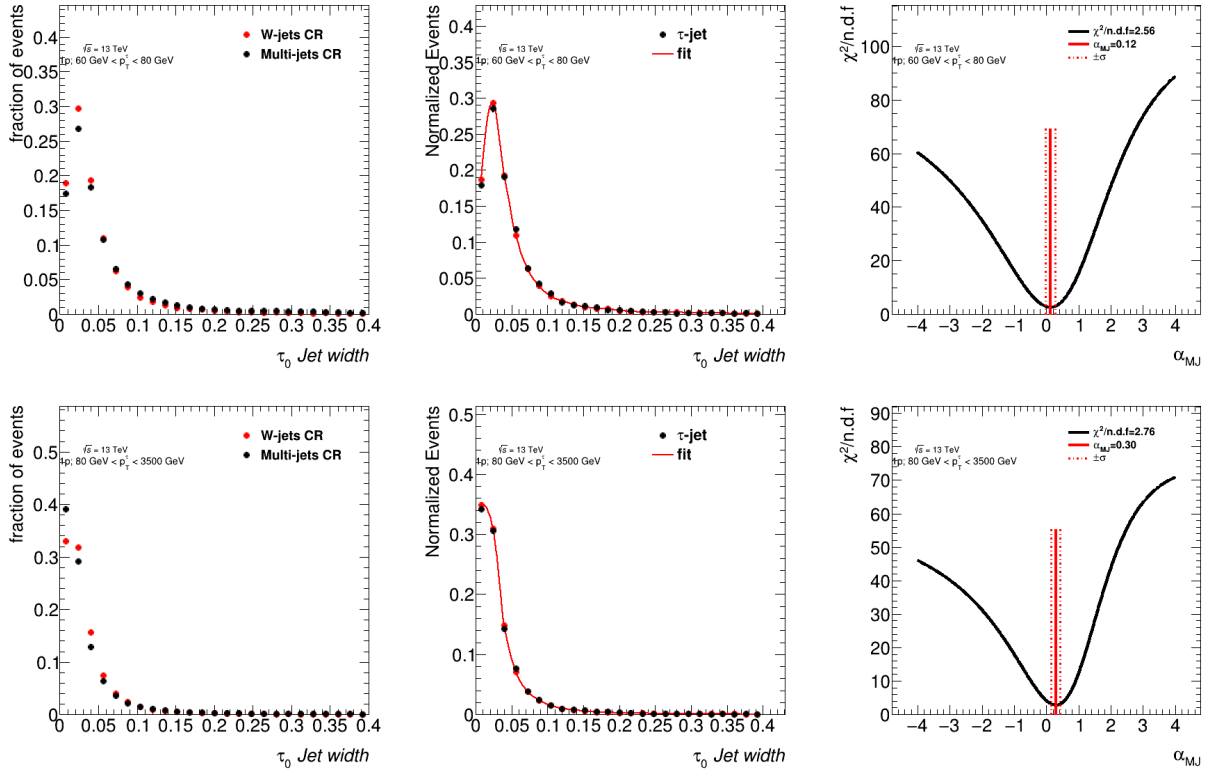


Figure B.4: Estimation of α_{MJ} in the $\tau_{had-vis} + \text{jets}$ signal region for $p_T \geq 60 \text{ GeV}$ 1-prong $\tau_{had-vis}$ candidates. Left: templates of discriminating variables for different $\tau_{had-vis}$ p_T and n-prong slices. Middle: shape of the discriminating variable obtained in the signal region and fitted shape using the templates measured in the control regions. Right: χ^2/ndf of the fit as a function of α_{MJ} , the error on α_{MJ} is defined by the band at $\chi^2_{\min}/\text{ndf} + \sqrt{\frac{2}{\text{ndf}}}$.

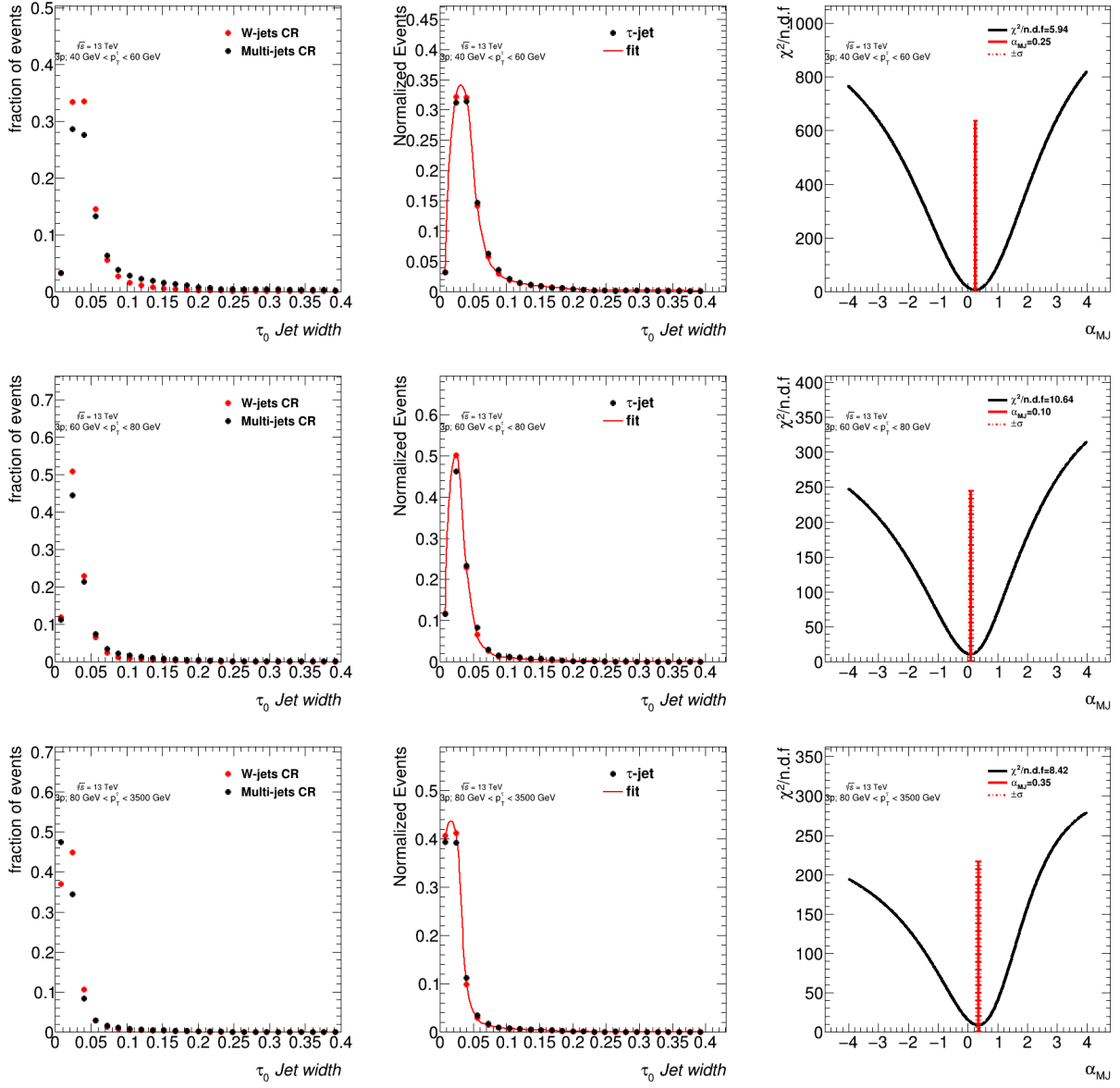


Figure B.5: Estimation of α_{MJ} in the $\tau_{\text{had-vis}} + \text{jets}$ signal region for 3-prong $\tau_{\text{had-vis}}$ candidates. Left: templates of discriminating variables for different $\tau_{\text{had-vis}}$ p_T and n-prong slices. Middle: shape of the discriminating variable obtained in the signal region and fitted shape using the templates measured in the control regions. Right: χ^2/ndf of the fit as a function of α_{MJ} , the error on α_{MJ} is defined by the band at $\chi^2_{\min}/\text{ndf} + \sqrt{\frac{2}{\text{ndf}}}$.

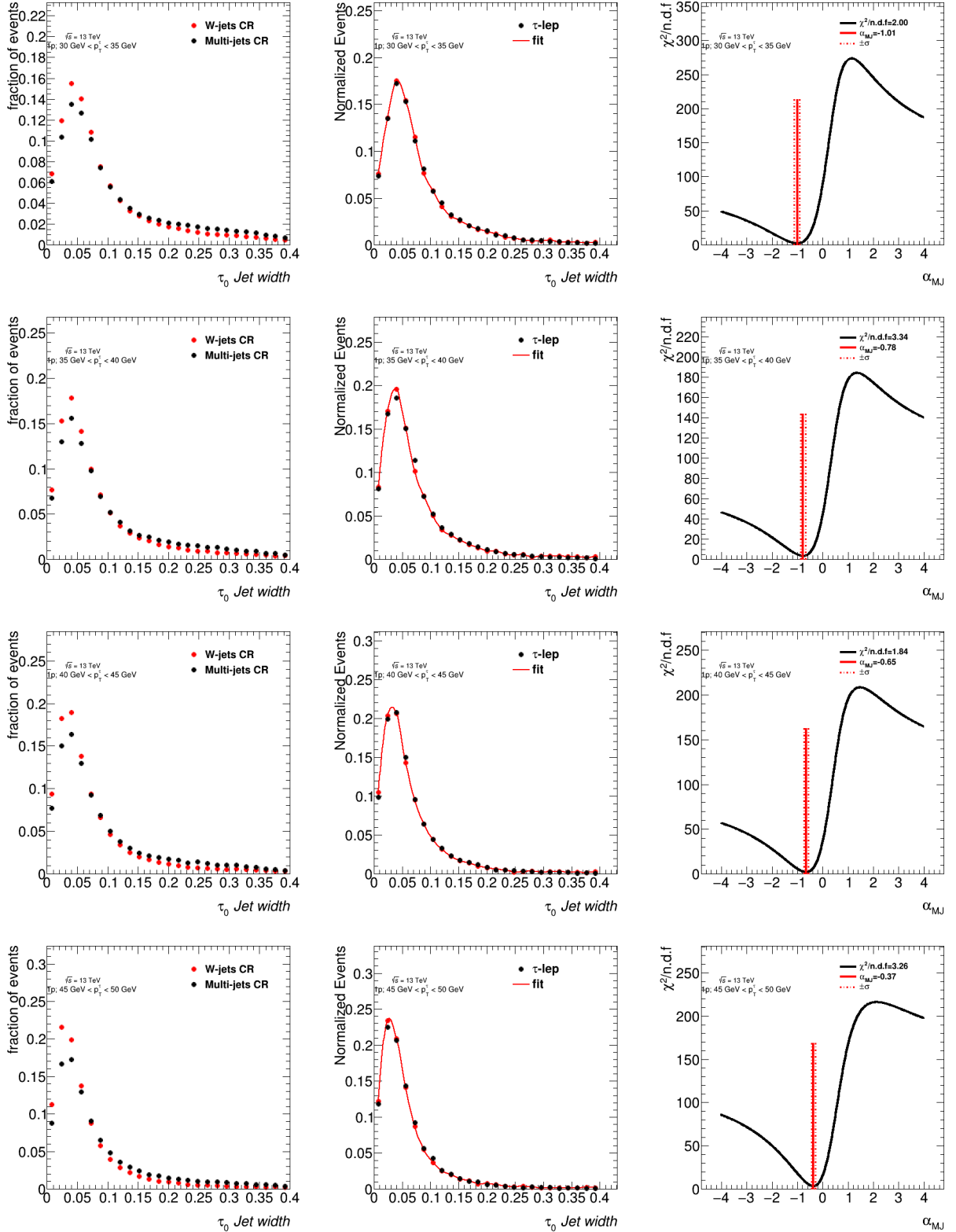


Figure B.6: Estimation of α_{MJ} in the $\tau_{\text{had-vis}} + \text{lepton}$ signal region for $p_T \leq 50 \text{ GeV}$ 1-prong $\tau_{\text{had-vis}}$ candidates. Left: templates of discriminating variables for different $\tau_{\text{had-vis}}$ p_T and n-prong slices. Middle: shape of the discriminating variable obtained in the signal region and fitted shape using the templates measured in the control regions. Right: χ^2/ndf of the fit as a function of α_{MJ} .

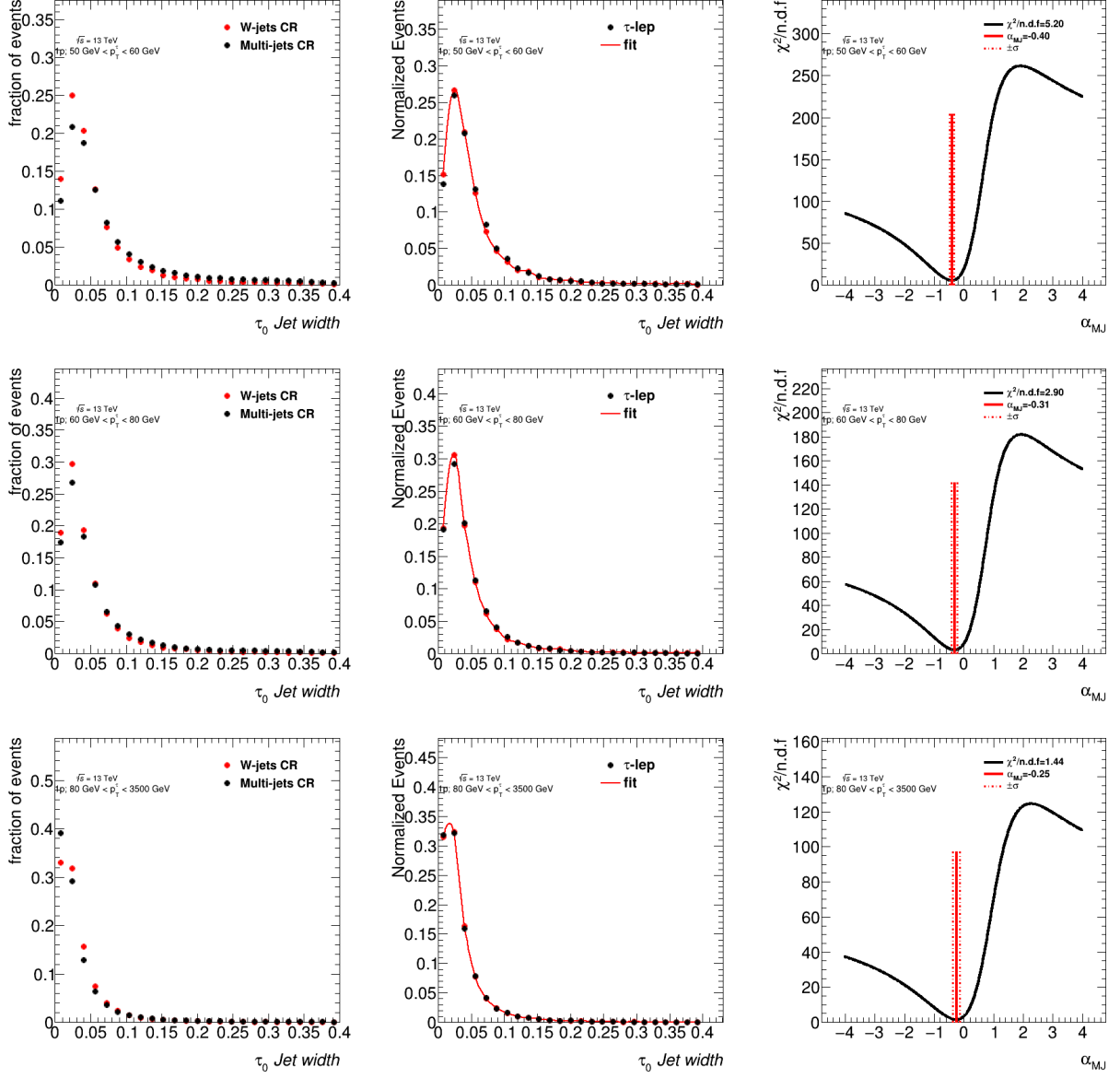


Figure B.7: Estimation of α_{MJ} in the $\tau_{\text{had-vis}} + \text{lepton}$ signal region for $p_T \geq 50 \text{ GeV}$ 1-prong $\tau_{\text{had-vis}}$ candidates. Left: templates of discriminating variables for different $\tau_{\text{had-vis}}$ p_T and n-prong slices. Middle: shape of the discriminating variable obtained in the signal region and fitted shape using the templates measured in the control regions. Right: χ^2/ndf of the fit as a function of α_{MJ} , the error on α_{MJ} is defined by the band at $\chi^2_{\min}/\text{ndf} + \sqrt{\frac{2}{\text{ndf}}}$.

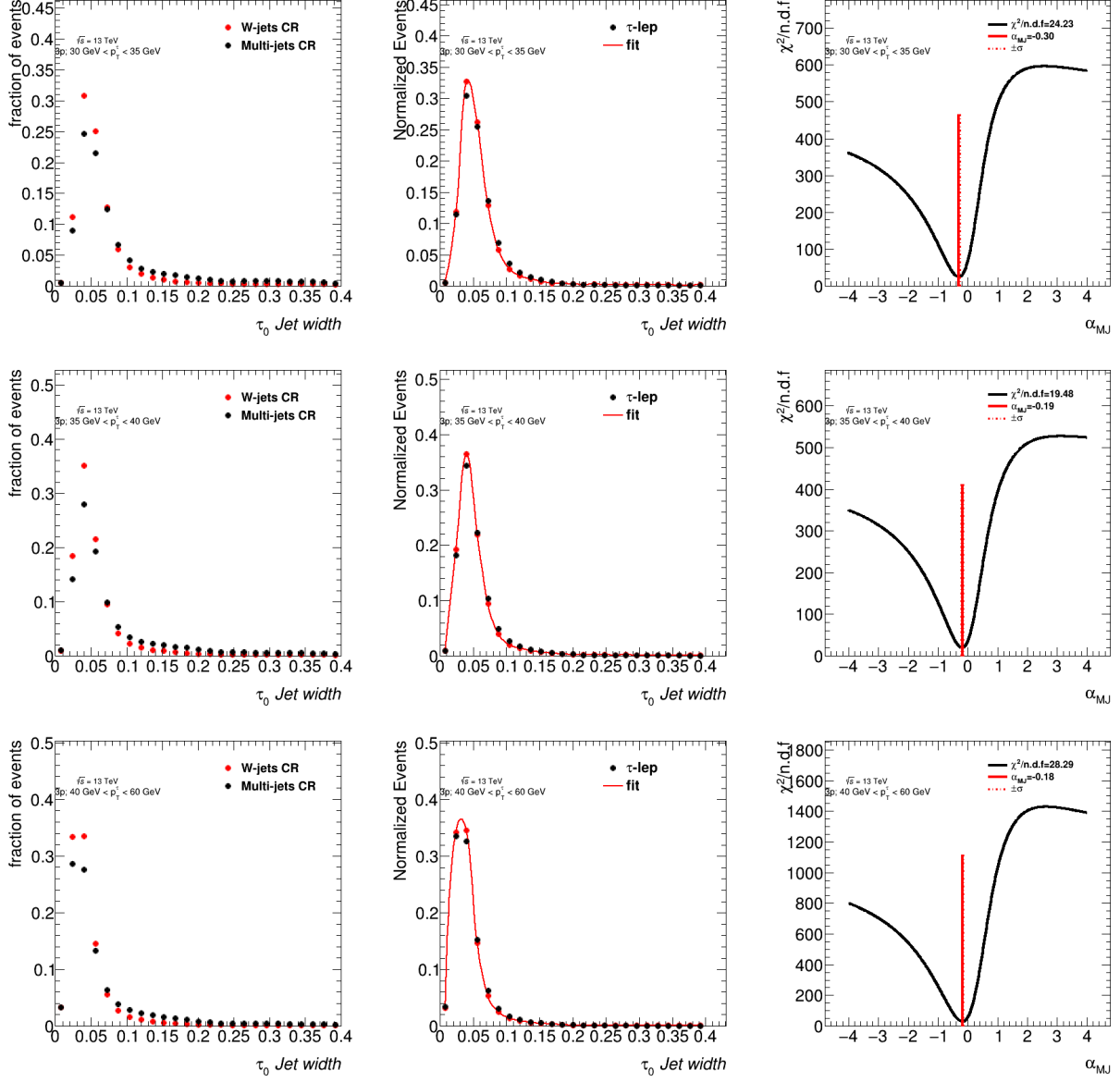


Figure B.8: Estimation of α_{MJ} in the $\tau_{had-vis} + \text{lepton}$ signal region for $p_T \leq 60 \text{ GeV}$ 3-prong $\tau_{had-vis}$ candidates. Left: templates of discriminating variables for different $\tau_{had-vis}$ p_T and n-prong slices. Middle: shape of the discriminating variable obtained in the signal region and fitted shape using the templates measured in the control regions. Right: χ^2/ndf of the fit as a function of α_{MJ} , the error on α_{MJ} is defined by the band at $\chi^2_{\min}/\text{ndf} + \sqrt{\frac{2}{\text{ndf}}}$.

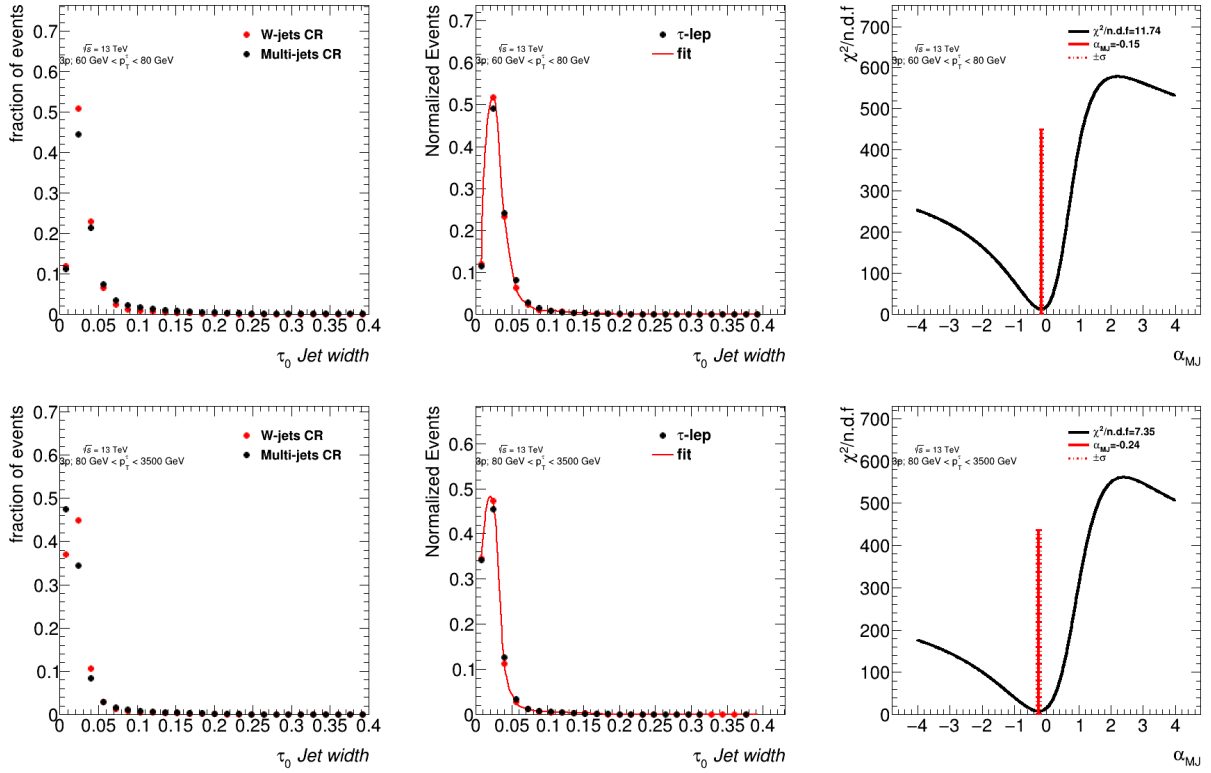


Figure B.9: Estimation of α_{MJ} in the $\tau_{\text{had-vis}} + \text{lepton}$ signal region for $p_T \geq 60 \text{ GeV}$ 3-prong $\tau_{\text{had-vis}}$ candidates. Left: templates of discriminating variables for different $\tau_{\text{had-vis}}$ p_T and n-prong slices. Middle: shape of the discriminating variable obtained in the signal region and fitted shape using the templates measured in the control regions. Right: χ^2/ndf of the fit as a function of α_{MJ} , the error on α_{MJ} is defined by the band at $\chi^2_{\min}/\text{ndf} + \sqrt{\frac{2}{\text{ndf}}}$.

APPENDIX C

ADDITIONAL VALIDATION PLOTS

C.1 $\tau + \text{jets}$ Validation Plots

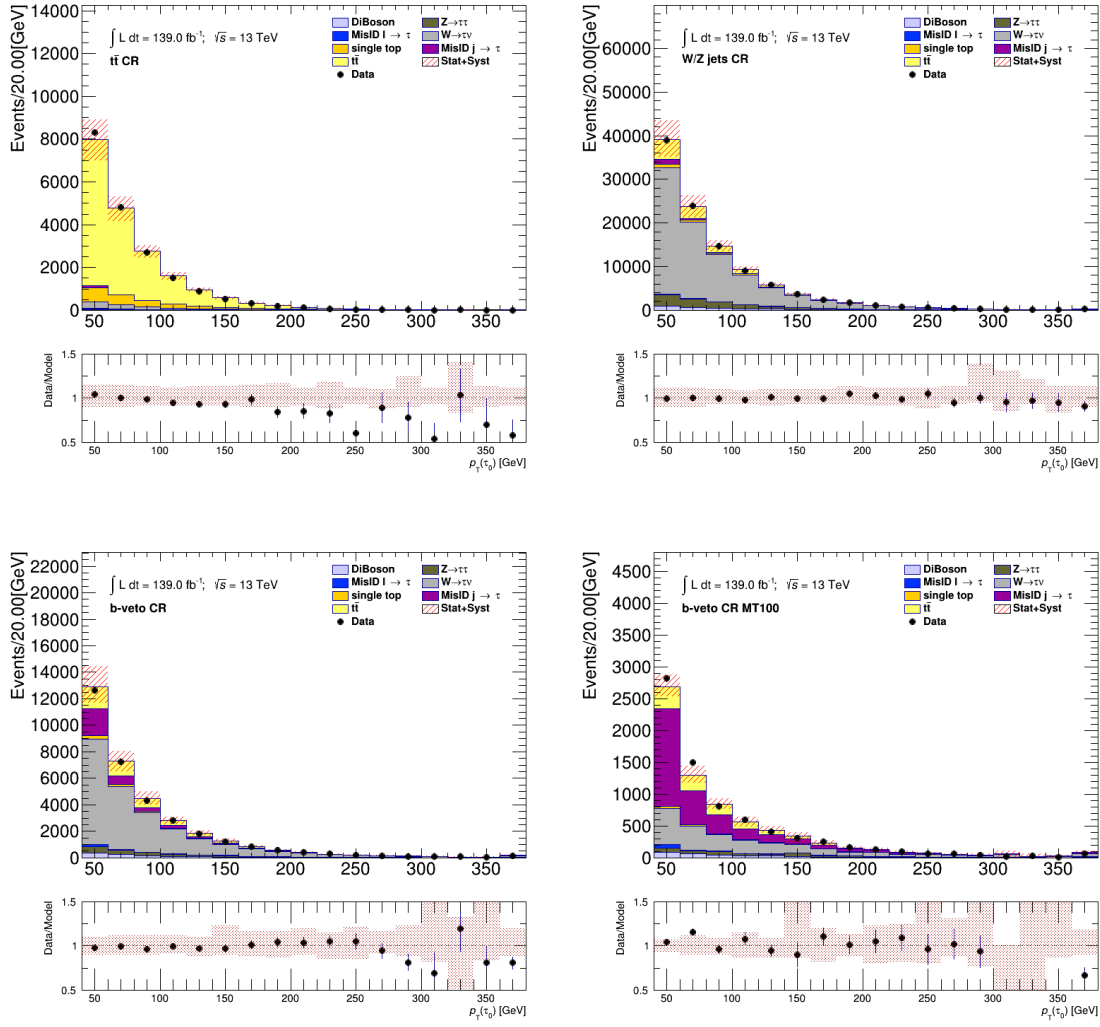


Figure C.1: Comparison between the predicted and the measured p_T^τ distributions in various control regions defined for the $\tau + \text{jets}$ channel. The uncertainty band includes both statistical and systematic uncertainties on the background prediction.

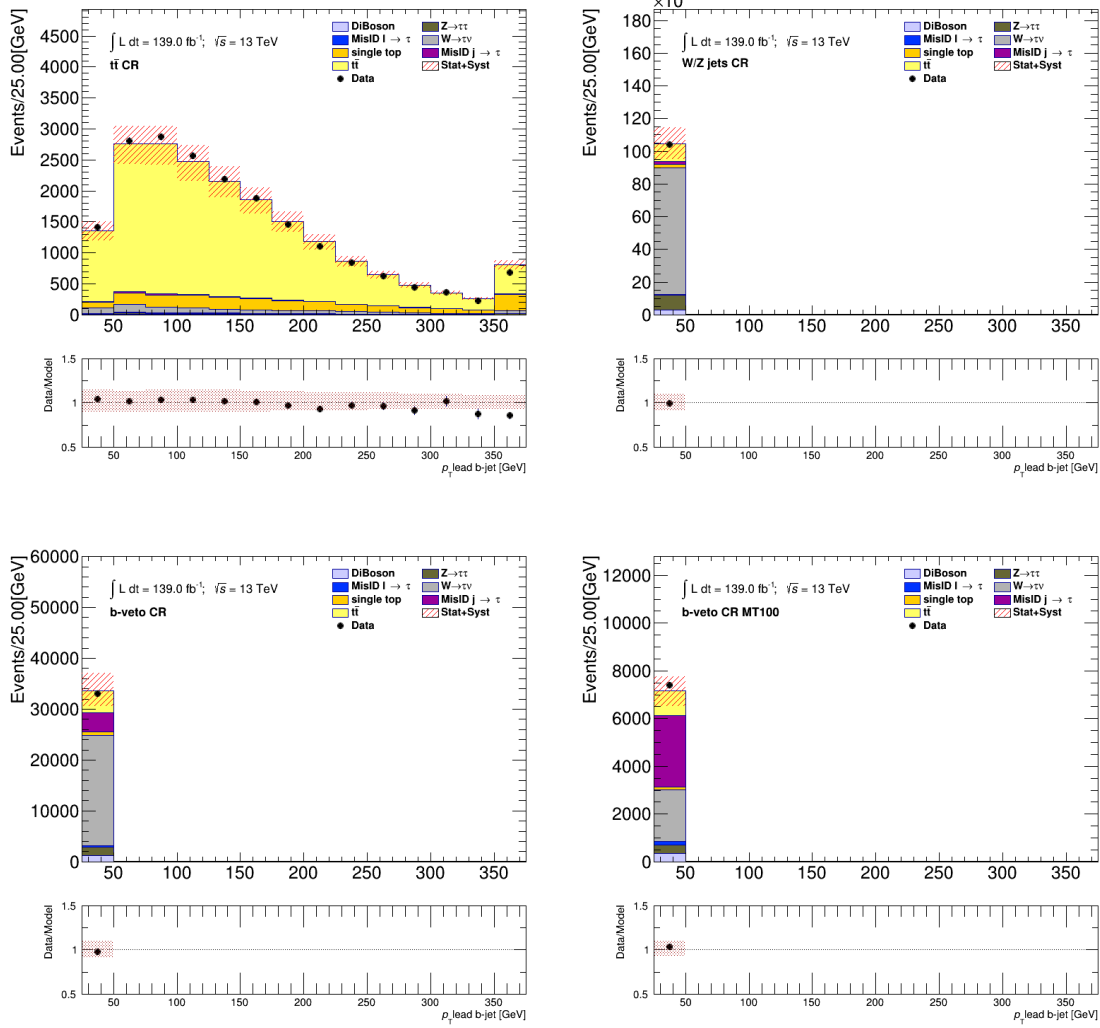


Figure C.2: Comparison between the predicted and the measured p_T^{b-jet} distributions in various control regions defined for the $\tau + \text{jets}$ channel. The uncertainty band includes both statistical and systematic uncertainties on the background prediction.

C.2 $\tau + \ell$ Validation Plots

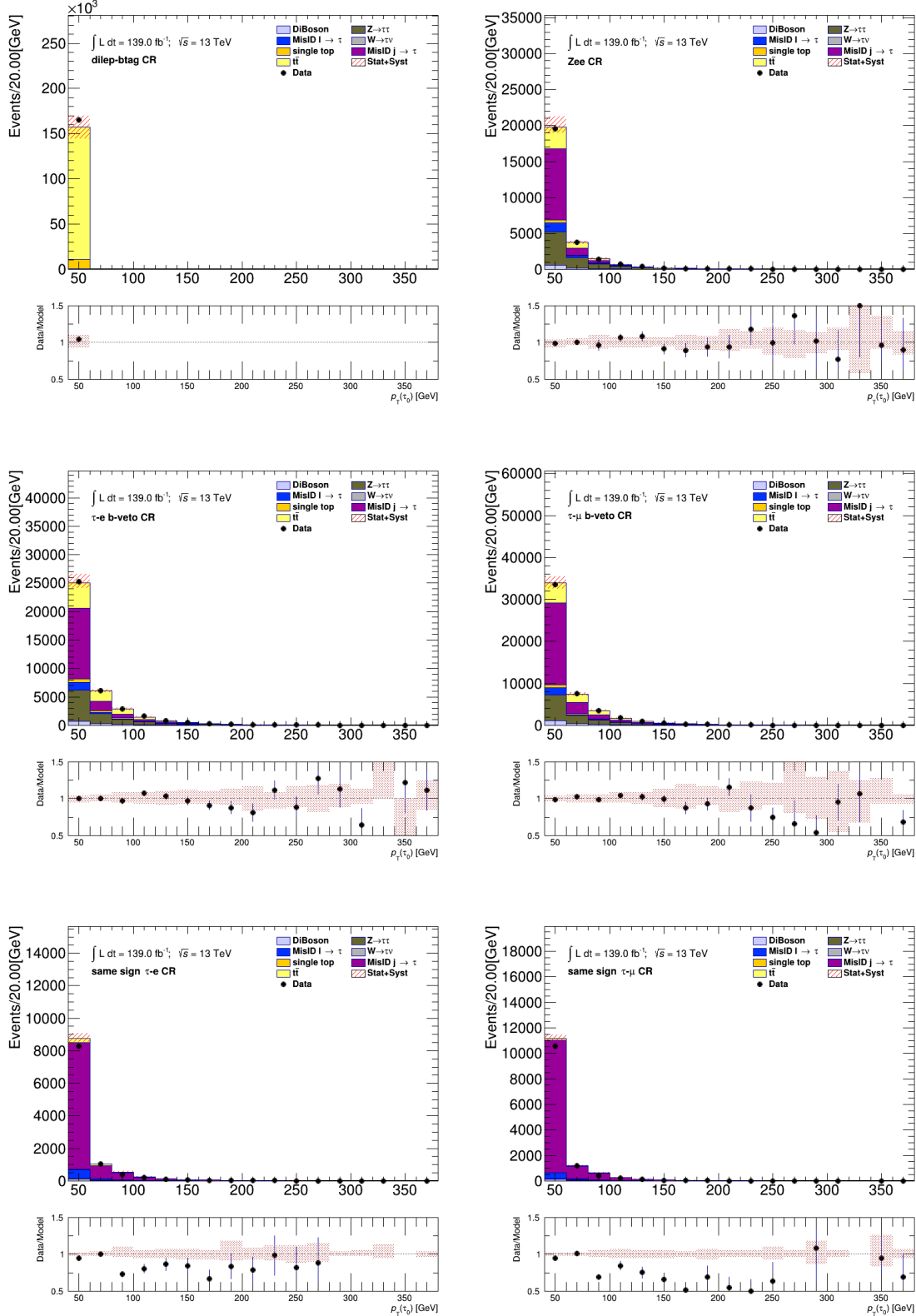


Figure C.3: Comparison between the predicted and the measured p_T^τ distributions in various control regions defined for the $\tau + \ell$ channel. The uncertainty band includes both statistical and systematic uncertainties on the background prediction.

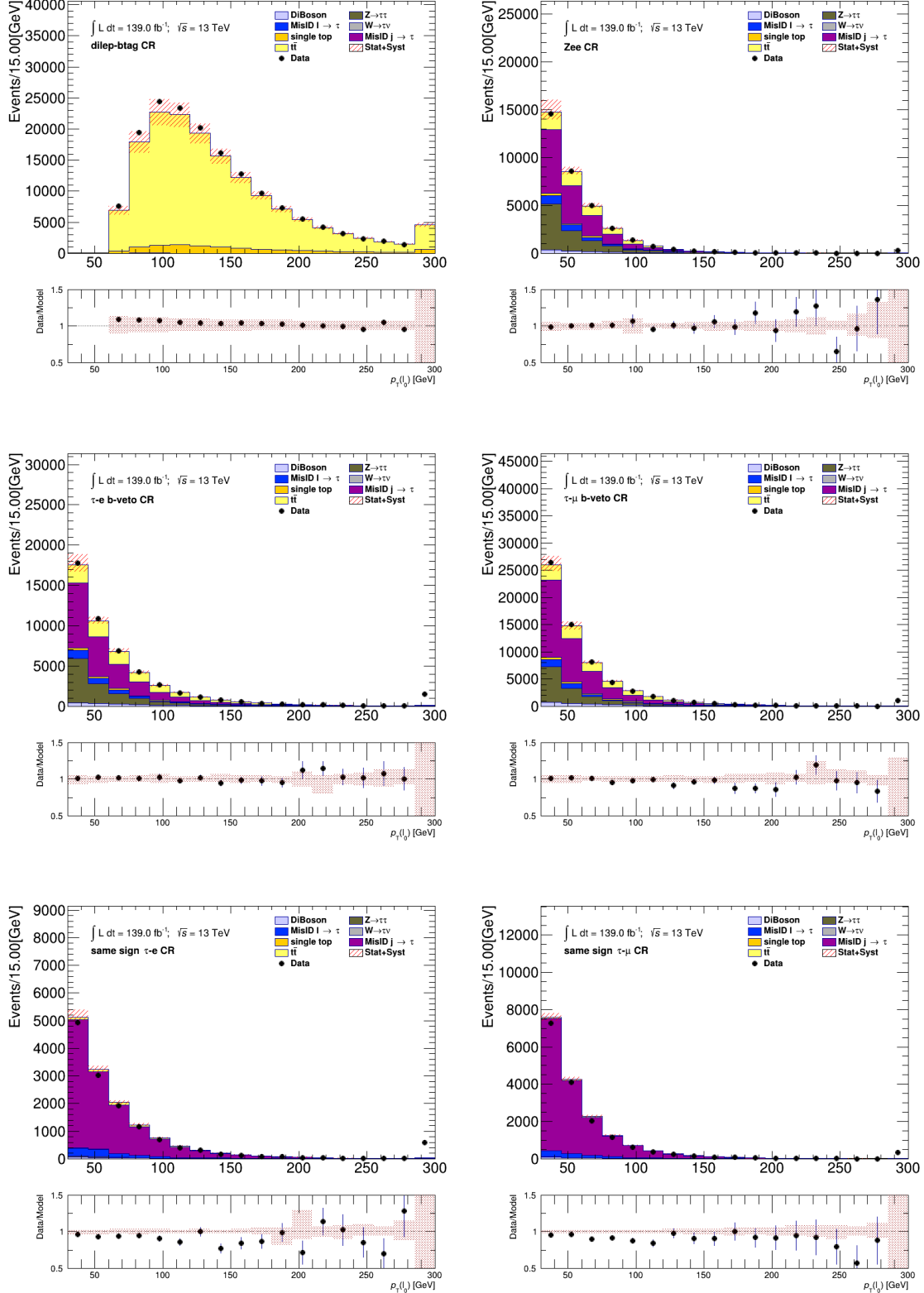


Figure C.4: Comparison between the predicted and the measured p_T^ℓ distributions in various control regions defined for the $\tau + \ell$ channel. The uncertainty band includes both statistical and systematic uncertainties on the background prediction.

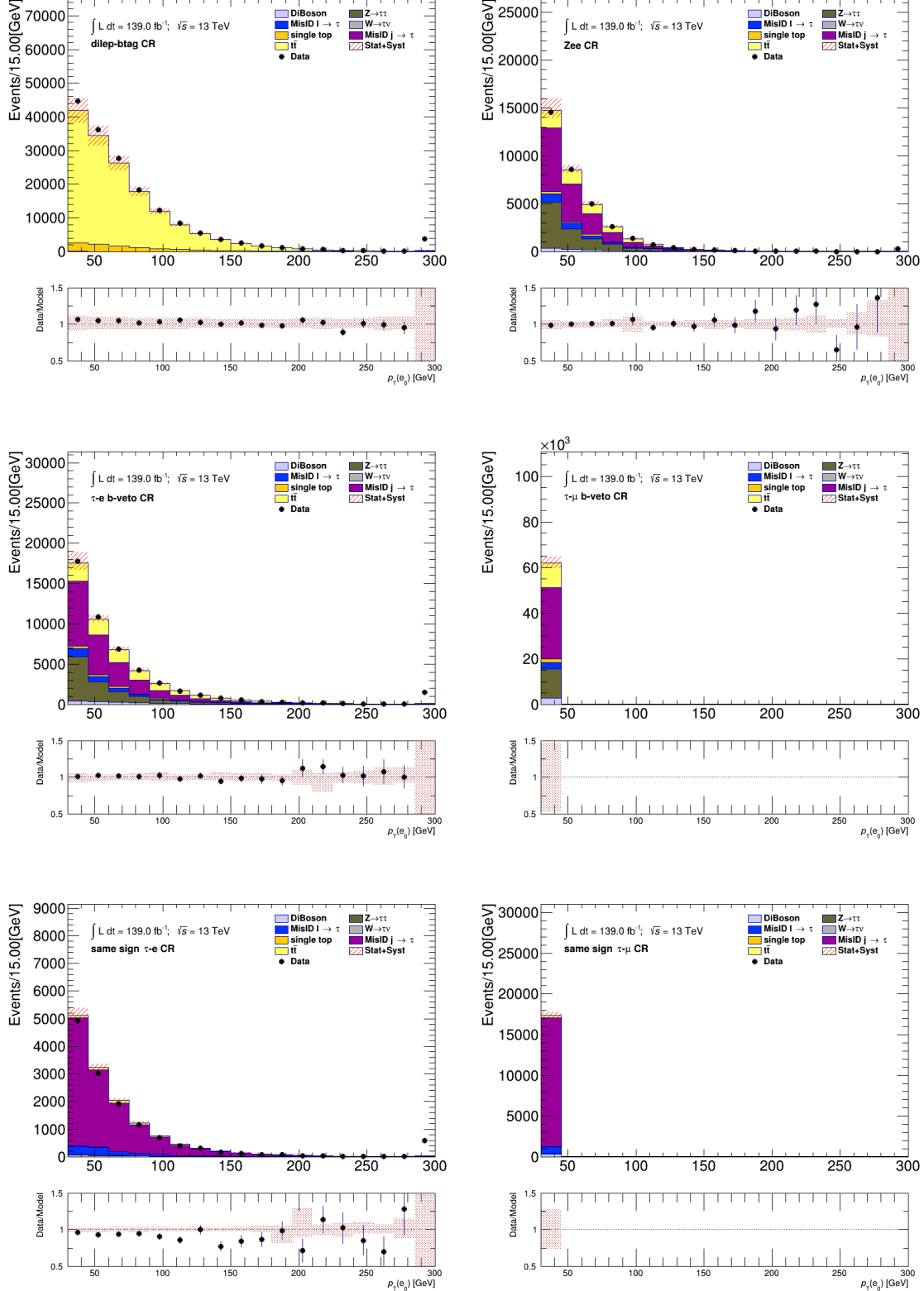


Figure C.5: Comparison between the predicted and the measured p_T^e distributions in various control regions defined for the $\tau + \ell$ channel. The uncertainty band includes both statistical and systematic uncertainties on the background prediction.

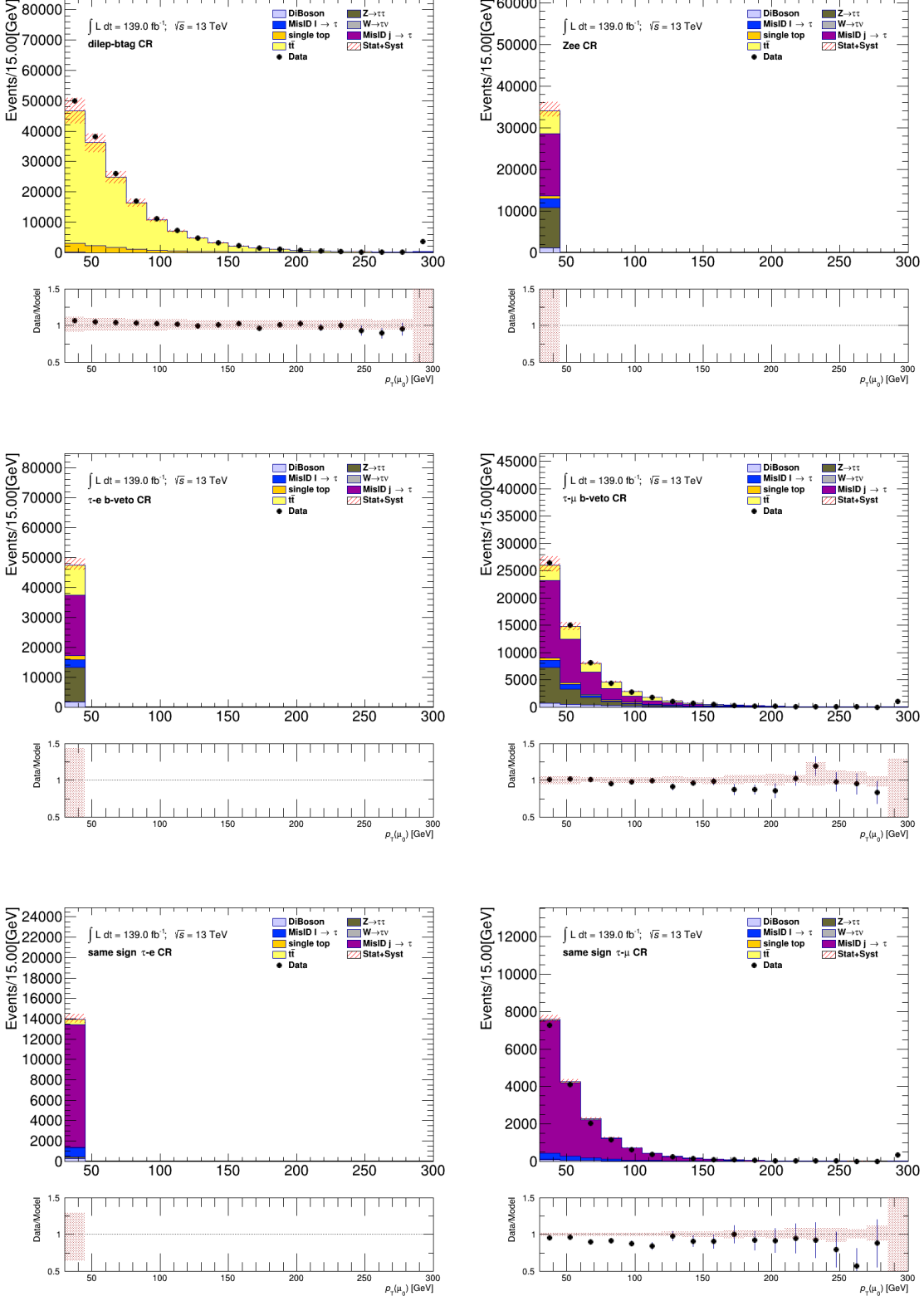


Figure C.6: Comparison between the predicted and the measured p_T^μ distributions in various control regions defined for the $\tau + \ell$ channel. The uncertainty band includes both statistical and systematic uncertainties on the background prediction.

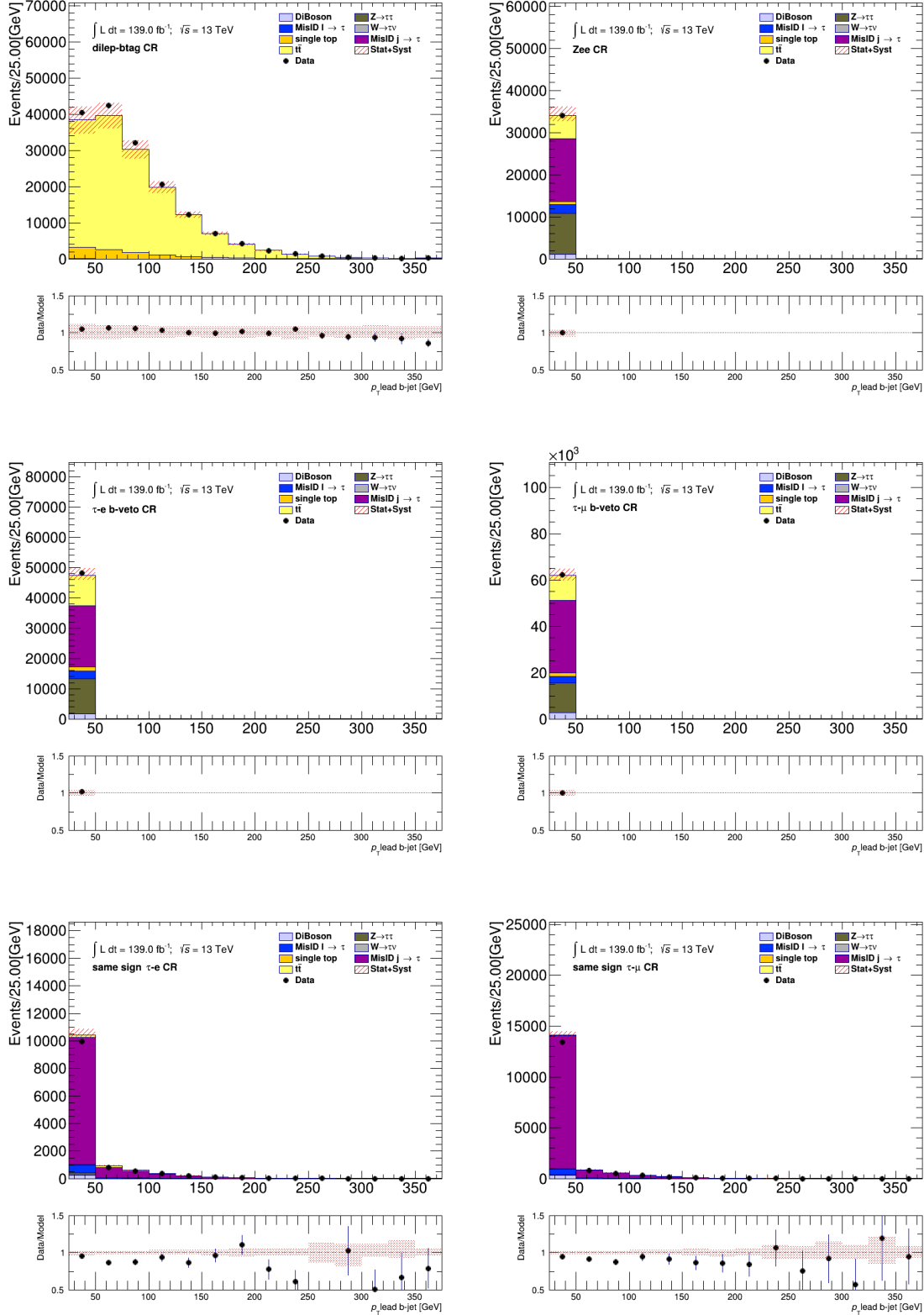


Figure C.7: Comparison between the predicted and the measured p_T^{b-jet} distributions in various control regions defined for the $\tau + \ell$ channel. The uncertainty band includes both statistical and systematic uncertainties on the background prediction.

BIBLIOGRAPHY

- [1] R. L. Workman et al. “Review of Particle Physics”. *PTEP* 2022 (2022), p. 083C01. DOI: 10.1093/ptep/ptac097.
- [2] P. W. Higgs. “Broken Symmetries and the Masses of Gauge Bosons”. *Phys. Rev. Lett.* 13 (16 Oct. 1964), pp. 508–509. DOI: 10.1103/PhysRevLett.13.508. URL: <https://link.aps.org/doi/10.1103/PhysRevLett.13.508>.
- [3] F. Englert and R. Brout. “Broken Symmetry and the Mass of Gauge Vector Mesons”. *Phys. Rev. Lett.* 13 (9 Aug. 1964), pp. 321–323. DOI: 10.1103/PhysRevLett.13.321. URL: <https://link.aps.org/doi/10.1103/PhysRevLett.13.321>.
- [4] J. Ellis. “Higgs Physics” (Dec. 2013). 52 pages, 45 figures, Lectures presented at the ESHEP 2013 School of High-Energy Physics, to appear as part of the proceedings in a CERN Yellow Report, 117–168. 52 p. DOI: 10.5170/CERN-2015-004.117. arXiv: 1312.5672. URL: <https://cds.cern.ch/record/1638469>.
- [5] T. A. Collaboration. “Observation of a new particle in the search for the Standard Model Higgs boson with the ATLAS detector at the LHC”. *Physics Letters B* 716.1 (2012), pp. 1–29.
- [6] G. Branco et al. “Theory and phenomenology of two-Higgs-doublet models”. *Physics Reports* 516.1–2 (July 2012), pp. 1–102. ISSN: 0370-1573. DOI: 10.1016/j.physrep.2012.02.002. URL: <http://dx.doi.org/10.1016/j.physrep.2012.02.002>.
- [7] J. R. Andersen et al. “Handbook of LHC Higgs Cross Sections: 3. Higgs Properties” (2013). Ed. by S. Heinemeyer et al. DOI: 10.5170/CERN-2013-004. arXiv: 1307.1347 [hep-ph].
- [8] T. A. Collaboration. “Search for charged Higgs bosons decaying via $H^\pm \rightarrow \tau^\pm \nu_\tau$ in the $\tau + \text{jets}$ and $\tau + \text{lepton}$ final states with 36 fb^{-1} of pp collision data recorded at $\sqrt{s} = 13$

- TeV with the ATLAS experiment”. *JHEP* 09 (2018), p. 139.
 DOI: 10.1007/JHEP09(2018)139. arXiv: 1807.07915 [hep-ex].
- [9] CERN. *Facts and figures about the LHC*.
 URL: <https://home.cern/resources/faqs/facts-and-figures-about-lhc>.
- [10] L. R. Evans and P. Bryant. “LHC Machine”. *JINST* 3 (2008). This report is an abridged version of the LHC Design Report (CERN-2004-003), S08001. 164 p.
 DOI: 10.1088/1748-0221/3/08/S08001.
 URL: <https://cds.cern.ch/record/1129806>.
- [11] X. C. Vidal and R. C. Manzano. *Lorentz Force Taking a closer look at LHC*. URL:
https://www.lhc-closer.es/taking_a_closer_look_at_lhc/0.lorentz_force.
- [12] E. Lopienska. “The CERN accelerator complex, layout in 2022. Complexe des accélérateurs du CERN en janvier 2022” (Feb. 2022). General Photo.
 URL: <https://cds.cern.ch/record/2800984>.
- [13] *Pseudorapidity*. Wikipedia, Feb. 2009.
 URL: <https://en.wikipedia.org/wiki/File:Pseudorapidity2.png>.
- [14] *ATLAS central solenoid: Technical Design Report*. Technical design report. ATLAS. Electronic version not available. Geneva: CERN, 1997.
 DOI: 10.17181/CERN.ZZVJ.2JYE. URL: <https://cds.cern.ch/record/331067>.
- [15] *ATLAS tile calorimeter: Technical Design Report*. Technical design report. ATLAS. Geneva: CERN, 1996. DOI: 10.17181/CERN.JRBJ.7028.
 URL: <https://cds.cern.ch/record/331062>.
- [16] J. P. Badiou et al. *ATLAS barrel toroid: Technical Design Report*. Technical design report. ATLAS. Electronic version not available.

- Geneva: CERN, 1997. DOI: 10.17181/CERN.RF2A.CP5T.
 URL: <https://cds.cern.ch/record/331065>.
- [17] N. Wermes and G. Hallewel. *ATLAS pixel detector: Technical Design Report*. Technical design report. ATLAS. Geneva: CERN, 1998.
 URL: <https://cds.cern.ch/record/381263>.
- [18] M. Capeans et al. *ATLAS Insertable B-Layer Technical Design Report*. Tech. rep. Sept. 2010. URL: <https://cds.cern.ch/record/1291633>.
- [19] *ATLAS inner detector: Technical Design Report, 1*. Technical design report. ATLAS. Geneva: CERN, 1997. URL: <https://cds.cern.ch/record/331063>.
- [20] The ATLAS Collaboration.
 “The ATLAS Experiment at the CERN Large Hadron Collider”.
Journal of Instrumentation 3.08 (Aug. 2008), S08003–S08003.
 DOI: 10.1088/1748-0221/3/08/s08003.
 URL: <https://doi.org/10.1088/1748-0221/3/08/s08003>.
- [21] *ATLAS muon spectrometer: Technical Design Report*. Technical design report. ATLAS. Geneva: CERN, 1997. URL: <https://cds.cern.ch/record/331068>.
- [22] T. A. collaboration. “Operation of the ATLAS trigger system in Run 2”.
Journal of Instrumentation 15.10 (Oct. 2020), P10004–P10004.
 DOI: 10.1088/1748-0221/15/10/p10004.
 URL: <https://doi.org/10.1088/1748-0221/15/10/p10004>.
- [23] C. Wanotayaroj. “Search for a Scalar Partner of the Top Quark in the Jets+MET Final State with the ATLAS detector”. Presented 25 Oct 2016. Nov. 2016.
 URL: <http://cds.cern.ch/record/2242196>.

- [24] S. Agostinelli et al. “Geant4 a simulation toolkit”. *Nuclear Instruments and Methods in Physics Research Section A: Accelerators, Spectrometers, Detectors and Associated Equipment* 506.3 (2003), pp. 250–303. ISSN: 0168-9002. DOI: [https://doi.org/10.1016/S0168-9002\(03\)01368-8](https://doi.org/10.1016/S0168-9002(03)01368-8). URL: <https://www.sciencedirect.com/science/article/pii/S0168900203013688>.
- [25] Garelli, Nicoletta on behalf of the ATLAS Collaboration. “Performance of the ATLAS Detector in Run-2”. *EPJ Web Conf.* 164 (2017), p. 01021. DOI: [10.1051/epjconf/201716401021](https://doi.org/10.1051/epjconf/201716401021). URL: <https://doi.org/10.1051/epjconf/201716401021>.
- [26] T. A. Collaboration. “Topological cell clustering in the ATLAS calorimeters and its performance in LHC Run 1”. *The European Physical Journal C* 77.7 (2017), p. 490. DOI: [10.1140/epjc/s10052-017-5004-5](https://doi.org/10.1140/epjc/s10052-017-5004-5). URL: <https://doi.org/10.1140/epjc/s10052-017-5004-5>.
- [27] T. A. Collaboration. “Muon reconstruction and identification efficiency in ATLAS using the full Run 2 pp collision data set at $\sqrt{s} = 13$ TeV”. *Eur. Phys. J. C* 81.7 (2021), p. 578. DOI: [10.1140/epjc/s10052-021-09233-2](https://doi.org/10.1140/epjc/s10052-021-09233-2). arXiv: 2012.00578 [hep-ex].
- [28] T. A. Collaboration. “Electron and photon performance measurements with the ATLAS detector using the 2015–2017 LHC proton-proton collision data”. *Journal of Instrumentation* 14.12 (Dec. 2019), P12006–P12006. DOI: [10.1088/1748-0221/14/12/p12006](https://doi.org/10.1088/1748-0221/14/12/p12006). URL: <https://doi.org/10.1088/1748-0221/14/12/p12006>.
- [29] T. A. Collaboration. “Jet reconstruction and performance using particle flow with the ATLAS Detector”. *The European Physical Journal C* 77.7 (2017), p. 466.

- DOI: [10.1140/epjc/s10052-017-5031-2](https://doi.org/10.1140/epjc/s10052-017-5031-2).
- URL: <https://doi.org/10.1140/epjc/s10052-017-5031-2>.
- [30] M. Cacciari, G. P. Salam, and G. Soyez. “The anti- k_T jet clustering algorithm”. *Journal of High Energy Physics* 2008.04 (Apr. 2008), pp. 063–063.
- DOI: [10.1088/1126-6708/2008/04/063](https://doi.org/10.1088/1126-6708/2008/04/063).
- URL: <https://doi.org/10.48550/arXiv.0802.1189>.
- [31] M. Cacciari, G. P. Salam, and G. Soyez. “The catchment area of jets”. *Journal of High Energy Physics* 2008.04 (Apr. 2008), pp. 005–005.
- DOI: [10.1088/1126-6708/2008/04/005](https://doi.org/10.1088/1126-6708/2008/04/005).
- URL: <https://doi.org/10.1088/1126-6708/2008/04/005>.
- [32] P. O. Hansson Adrian. *The ATLAS b-jet Trigger*. Tech. rep.
Comments: 4 pages, 6 figures, conference proceedings for PIC2011.
Geneva: CERN, Nov. 2011. arXiv: [1111.4190](https://arxiv.org/abs/1111.4190).
URL: <https://cds.cern.ch/record/1397942>.
- [33] *Optimisation and performance studies of the ATLAS b-tagging algorithms for the 2017-18 LHC run*. Tech. rep. All figures including auxiliary figures are available at <https://atlas.web.cern.ch/Atlas/GROUPS/PHYSICS/PUBNOTES/ATL-PHYS-PUB-2017-013>. Geneva: CERN, July 2017.
URL: [http://cds.cern.ch/record/2273281](https://cds.cern.ch/record/2273281).
- [34] *Expected performance of the ATLAS b-tagging algorithms in Run-2*. Tech. rep.
All figures including auxiliary figures are available at <https://atlas.web.cern.ch/Atlas/GROUPS/PHYSICS/PUBNOTES/ATL-PHYS-PUB-2015-022>. Geneva: CERN, July 2015.
URL: <https://cds.cern.ch/record/2037697>.

- [35] *E_T^{miss} performance in the ATLAS detector using 2015-2016 LHC p-p collisions.* Tech. rep. All figures including auxiliary figures are available at <https://atlas.web.cern.ch/Atlas/GROUPS/PHYSICS/CONFNOTES/ATLAS-CONF-2018-023>. Geneva: CERN, June 2018.
URL: <https://cds.cern.ch/record/2625233>.
- [36] *Luminosity determination in pp collisions at $\sqrt{s} = 13$ TeV using the ATLAS detector at the LHC.* Tech. rep. All figures including auxiliary figures are available at <https://atlas.web.cern.ch/Atlas/GROUPS/PHYSICS/CONFNOTES/ATLAS-CONF-2019-021>. Geneva: CERN, June 2019.
URL: <http://cds.cern.ch/record/2677054>.
- [37] *A study of optimal parameter setting for MADGRAPH5_AMC@NLO + PYTHIA 8 matched setup.* Tech. rep. All figures including auxiliary figures are available at <https://atlas.web.cern.ch/Atlas/GROUPS/PHYSICS/PUBNOTES/ATL-PHYS-PUB-2015-048>. Geneva: CERN, Nov. 2015.
URL: <https://cds.cern.ch/record/2103221>.
- [38] P. Baldi et al. “Parameterized neural networks for high-energy physics”. *The European Physical Journal C* 76.5 (2016), p. 235.
DOI: [10.1140/epjc/s10052-016-4099-4](https://doi.org/10.1140/epjc/s10052-016-4099-4).
URL: <https://doi.org/10.1140/epjc/s10052-016-4099-4>.
- [39] URL: <https://keras.io/>.
- [40] Martín Abadi et al.
TensorFlow: Large-Scale Machine Learning on Heterogeneous Systems.
Software available from tensorflow.org. 2015. URL: <https://www.tensorflow.org/>.

- [41] B. Burghgrave. “Search for charged Higgs Bosons in the $\tau +$ lepton final state with 36.1 fb^{-1} of pp collision data recorded at $\sqrt{s} = 13 \text{ TeV}$ with the ATLAS experiment”. PhD thesis. Northern Illinois U., 2018.